UNIVERSITÀ
DEGLI STUDI
DI PADOVA

Administrative Headquater: University of Padova, Italy

Department of Industrial Engineering

Ph.D. SCHOOL OF RESEARCH IN: Industrial Engineering

Address : Energy Engineering

CYCLE : XXVI°

Electric Vehicle Propulsion System

Director of the School **: Ch.mo Prof. Paolo Colombo**

Coordinator **: Ch.mo Prof. Luisa Rossetto**

Supervisor **: Ch.mo Prof. Giuseppe Buja**

PhD Student **: Ritesh Kumar Keshri**

UNIVERSITÀ
DEGLI STUDI
DI PADOVA

Sede Amministrativa: Università degli Studi di Padova

Dipartimento di Dipartimento di Ingegneria Industriale

SCUOLA DI DOTTORATO DI RICERCA IN : Ingegneria Industriale
INDIRIZZO: Ingegneria dell' Energia
CICLO: XXVI°

Electric Vehicle Propulsion System

Direttore della Scuola	: Ch.mo Prof. Paolo Colombo	Paolo Colombo
Coordinatore d'indirizzo	: Ch.mo Prof. Luisa Rossetto	Luisa Rossetto
Supervisore	: Ch.mo Prof. Giuseppe Buja	G. Buja
Dottorando	: Ritesh Kumar Keshri	Ritesh Keshri

Abstract

Electric vehicles are being considered as one of the pillar of eco-friendly solutions to overcome the problem of global pollution and radiations due to greenhouse gases. Present thesis work reports the improvement in overall performance of the propulsion system of an electric vehicle by improving autonomy and torque-speed characteristic. Electric vehicle propulsion system consists of supply and traction system, and are coordinated by the monitoring & control system. Case of light electric vehicle propulsion system with permanent-magnet (PM) brushless dc (BLDC) drive being used in electric scooters and electric-mini cars is considered for analytical study and the implementation of the proposed solutions. PM BLDC motor and voltage source inverter are considered as a part of traction system and electric energy source such as battery, fuel cell or photovoltaic panel are considered as a part of supply system.

Available electric energy sources are capable of delivering higher current at lower terminal voltage, so are connected either in series or -more often- to the higher voltage dc-link through a circuital arrangement (boost topology) to achieve higher voltage. For the evaluation of boost topologies, traditional dc-to-dc boost converter with cascade VSI (DBI) and Z-source inverter (ZSI) are considered for fuel cell and battery as on-board energy sources. Evaluation of the convenience of the two supply topologies is carried out in terms of the factors defining transistor power utilization, and voltage and current transistor solicitation. In addition to mentioned defined factors, sizing of the passive components in terms of the power contribution factor of fuel cell is considered. In respect to the defined factors, DBI supply is found to be beneficial for PM BLDC drive whereas, with respect to the power contribution factor, ZSI supply is good to adopt for the cases were major contribution of power is from battery.

For the improvement in torque-speed characteristics of the considered drive, issue of torque ripple due to non-ideal phase commutation in case of conventional square-wave phase current (SqPC) supply is studied analytically by establishing a correlation between the behavior of the commutating phase currents and motor torque. Behavior of the motor torque during commutation for low and high speed zone as a function motor speed and defined motor specific quantity are explained in detailed. The analytical results are used to explain the dropping torque-speed characteristic of the drive and are verified experimentally for a propulsion drive available in the laboratory. Dropping torque-speed characteristic limits the use of the drive up till the nominal speed. To overcome this issue sinusoidal phase current (SPC) supply is proposed. SPC offers constant motor torque. A detailed convenience analysis of SPC over SqPC is carried out. Strategy for the implementation of SPC supply is also discussed and the analytical results were verified by the experimentally.

The study of the PM BLDC drive by means of the space phasor/vector approach has been executed. While such an approach is quite common for drives with motors with sinusoidal back-emf and phase currents, it is not explored in the literature for the present case, where back-emfs are trapezoidal and phase currents are square-wave in nature. Behavior of the PM BLDC drive has been revisited in stationary plane and the current commutation between the motor phases has been explained with the help of phase variable vectors. All the results obtained in a-b-c plane are cross verified in stationary plane showing the simplicity and potentialities of the vector approach for PM BLDC drive.

To address the issue of the autonomy of electric vehicles, use of solar energy to assist the on-board batteries of an electric mini-car is considered. Photovoltaic Geographical Information Systems database provided by Joint Research Centre Europe, is used to estimate the solar irradiance available in Padova, Italy. Output of a 0.487 sq-meter, 20-cell multi-crystalline PV panel is estimated and accordingly a conventional dc-to-dc boost converter is designed to interface PV panel with dc-link of a mini-car available in the laboratory. Appropriate control is implemented through DSP to track maximum power point. Whole system was tested outside the laboratory and measurements were carried out. Analytical loss model of the dc-to-dc boost converter is developed to explain the variations in gain, efficiency and loss components of the converter under varying solar irradiance.

The thesis work has been carried out at the Laboratory of "Electric systems for automation and automotive" headed by Prof. Giuseppe Buja. The laboratory belongs to the Department of Industrial Engineering of the University of Padova.

Sommario

I veicoli elettrici sono considerati uno dei pilastri tra le soluzioni ecosostenibili per superare il problema dell'inquinamento globale dovuto ai gas serra. Questo lavoro di tesi tratta del miglioramento delle prestazioni complessive di un sistema di propulsione di un veicolo elettrico mediante l'aumento dell'autonomia e della caratteristica coppia-velocità. Il sistema di propulsione di un veicolo elettrico consiste in un sistema di alimentazione e di un sistema di trazione, coordinati da un sistema di monitoraggio e controllo. Lo studio analitico e l'implementazione della soluzione proposta per il sistema di propulsione sono stati svolti con riferimento ad un motore brushless a magneti permanenti con fem trapezoidale (PM BLDC), utilizzato comunemente in veicoli elettrici leggeri come gli scooter e le mini-car. Il sistema di propulsione è costituito dal motore PM BLDC e dall'invertitore di tensione, mentre il sistema di alimentazione è formato da sorgenti energia elettrica come le batterie, le celle a combustibile o i pannelli fotovoltaici.

Le sorgenti di energia elettrica disponibili sul mercato consentono di raggiungere elevati valori di corrente ma con bassi valori di tensione. Al fine di ottenere i valori di tensioni richiesti dal bus in continua, esse sono collegate in serie tra loro o sono connesse mediante convertitori innalzatori di tensione. Ciò può avvenire o attraverso un tradizionale convertitore dc/dc innalzatore con in cascata un invertitore di tensione (DBI) o attraverso un invertitore di tipo Z-source (ZSI). La valutazione di convenienza delle due modalità di alimentazione è basata sul fattore di utilizzazione e sulle sollecitazioni in termini di corrente e tensione dei transistor di potenza. Oltre ai fattori menzionati in precedenza, sono stati dimensionati gli elementi passivi in funzione della quota parte di potenza fornita dalla cella a combustibile. In relazione ai parametri definiti, la migliore soluzione risulta essere l'alimentazione con DBI, mentre quella con ZSI appare conveniente quando la maggior parte della potenza assorbita dal carico sia fornita dalle batterie.

Al fine di migliorare le prestazioni di coppia, il ripple di coppia dovuto alla non ideale commutazione del convertitore ad onda quadra (SqPC) è stato studiato analiticamente, stabilendo la correlazione tra le correnti durante la fase di commutazione e la coppia del motore. Il comportamento di coppia a basse ed ad alte velocità è stato esaminato in dettaglio utilizzando specifiche grandezze del motore. I risultati analitici sono stati utilizzati per spiegare la caduta della coppia sviluppata dal motore ad alte velocità; essi sono stati verificati sperimentalmente su un azionamento di propulsione disponibile in laboratorio. La non costanza della caratteristica coppia-velocità limita l'uso del motore nei pressi della velocità nominale. Per superare questo limite è stata altresì utilizzata un'alimentazione con corrente sinusoidale (SPC). Essa permette di fornire al motore una coppia costante. E' stata quindi eseguita un'analisi dettagliata al fine di vedere quale sia il metodo di alimentazione più conveniente tra SqPC e SPC. È stata altresì descritta la strategia d'implementazione dell'alimentazione SPC, e i risultati analitici sono stati verificati sperimentalmente.

E' stato eseguito lo studio degli azionamenti con motori PM BLDC con l'approccio dei fasori spaziali. Mentre questo approccio è abbastanza comune nel caso di azionamenti con motori con forza contro-elettromotrice e correnti di sinusoidali, esso non è trattato in letteratura per gli azionamenti con motori PM BLDC, in quanto la forza contro-elettromotrice è trapezoidale e il profilo delle correnti di fase è un onda quadra. Il comportamento del motore PM BLDC è stato rivisitato sul piano stazionario e la

commutazione della corrente tra le fasi è stata descritta con l'ausilio dei vettori delle grandezze di fase. Tutti i risultati ottenuti nel piano a-b-c sono stati verificati nel piano stazionario, mostrando la semplicità e le potenzialità dell'approccio vettoriale.

Al fine di estendere l'autonomia del veicolo sono stati utilizzati dei pannelli fotovoltaici. Il Sistema Geografico di Informazioni Fotovoltaico sviluppato dal Joint Research Center Europe è stato utilizzato per stimare il valore d'irraggiamento solare disponibile a Padova. È stata stimata la potenza generata da un pannello fotovoltaico di superficie 0.487 m^2, formato da 20 celle multi-cristalline, e in relazione ad essa, è stato progettato il convertitore dc-dc elevatore per interfacciare il pannello fotovoltaico al bus in continua di una mini-car disponibile in laboratorio. Un appropriato controllo è stato implementato in un processore DSP al fine di inseguire il punto di massima potenza. L'intero sistema è stato provato all'esterno del laboratorio, facendo le misure necessarie per le verifiche. Un modello analitico delle perdite del convertitore dc-dc elevatore è stato sviluppato per descrivere la variazione di guadagno, rendimento e perdite del convertitore al variare dell'irraggiamento solare.

Il lavoro di tesi è stato sviluppato presso il Laboratorio di "Sistemi elettrici per l'automazione e la veicolistica" diretto dal Prof. Giuseppe Buja. Il laboratorio afferisce al Dipartimento di Ingegneria Industriale dell'Università di Padova.

Dedicated to

my parents
father: Late Murari Prasad Keshri, mother: Satyabhama Devi

and

Beloved wife: Manju, and daughter: Sneha

Acknowledgement

I would like to express my deepest gratitude to each and every one who helped me with their continuous support during my doctoral work. Even though it is not possible to wrap the support of my supervisor with words, I take this opportunity to thank Prof. Giuseppe Buja, who has been constant source of inspiration and guidance, without whom successful completion of the work for the thesis would not have been feasible. I am also grateful to Dr. Manuele Bertoluzzo (Assistant Professor, Department of Industrial Engineering), whose dedication towards the laboratory remains unparalleled. His support to me and fellow students has always been an ever increasing source of motivation.

I am grateful to coordinators of the WillPower Program at Ecole Centrale di Nantes, France and University of Padova, Italy for considering me as a grantee for 34 months with Erasmus Mundus Fellowship from European Commission. My sincere appreciations to Prof. Colombo, Prof. Luisa Rosetto, Prof. Martinelli, and administrative staffs of the department and the University for their support. I have always found them responsive and supportive not only to me but to all the students, contributing towards an excellent world class research environment. I am also thankful to all the non-teaching technical staffs of the department for their assistance bestowed.

I would like to extend my salute and thanks to all my colleague students Michele, Marco, Nicola Ganeo, Davide, Nima Zabihi, Osley, Kishore, Syamnaresh and Kundan for their professionalism, company and respect during group work and social activities. In addition, I would like to thanks my Italian friends Elena, Luca Sinigaglia and Sara for considering me and my family like members of their own. I am especially indebted to my family members for their patience and moral support during my doctoral work.

Last but not the least, I am beholdento all those who helped me directly and indirectly in my work.

Table of Content

Chapter 5

Chapter 6

Chapter 7

Chapter 1

Introduction

Research work reported in this Ph.D. thesis is in the area of Electric Vehicle Propulsion System (EVPS). This research carries out the study, performance improvement and evaluation of the components of an EVPS. Different components of an EVPS are categorized under three subsystem termed as supply system, traction system, and control & monitoring system. Supply and traction systems are connected to each other through a high-voltage dc-link. Control system & monitoring system continuously monitors the activities of two subsystems and other on-board accessories. Traction system of an electric vehicle consists of traction motor(s) together with appropriate converters, for controlled conversion of energy submitted by the supply system to the dc-link. Converter used for the controlled energy conversion are dc-to-ac converter as per the type of traction motor used for propulsion. Supply system consists of energy sources alone or together with bi-directional converters to meet bi-directional power flow requirements for the recovery of energy during regeneration.

Present research considers electric scooters and electric mini-cars as an example of study and implementation of developed strategies for the improvement of the performance of supply and traction system. Improvement of performance refers to the speed torque characteristics of the traction motor and the extension in the autonomy of the considered electric vehicles. Both of the considered electric vehicles belongs to the category of light-electric vehicles whose mobility is limited to a city or town. The two vehicles use Permanent-magnet (PM) brushless dc (BLDC) motors for traction. PM BLDC motors are characterised by their capability of offering higher power density and motor-torque compared to the motors of other types and of same size. Chapter 2 of the thesis discusses above mentioned subsystems of the used PM BLDC drive explaining the principle of operation, and electrical & mechanical characteristics of the drive.

PM BLDC motors used for the traction purpose are generally designed for higher terminal voltages to reduce the copper loss, whereas the existing on-board dc sources are capable of delivering higher current with low terminal voltage. To meet the higher dc-link voltage, energy sources are either connected in series or are connected to the dc-link through circuital arrangements to achieve proper gain in the voltage. Use of any of the boost topology is important for the cases where space and electrical response are big concern, such as the cases of fuel cells and photovoltaic (PV) panel as an energy source. Dc-to-dc boost converter is one of the popular topology for such case. Chapter 3 of the thesis carries out a discussion on the comparative evaluation of another popular boost topology termed as Z-source inverter (ZSI) with a topology having a combination of dc-to-dc boost converter and VSI termed as DBI for PM BLDC drive having fuel cell as an energy source. Case of DBI is a two stage energy conversion process (dc-to-dc and then dc-to-ac); contrary to this, ZSI uses z-connected passive network together with VSI and offers single

stage energy conversion process (dc-to-ac). For the comparative evaluation, total voltage and current solicitation of the transistors, transistor utilisation and the sizing power of the passive components are defined as evaluation factors. In addition to this, sizing of the passive component as a function of power contribution is considered as another measure. Based on the outcome, overall evaluation is carried out for the two topologies. It has been found that, the current and voltage ratings of the transistors and sizing power of the passive components are quite higher for the ZSI supply compared to the DBI supply. This raises cost of the devices and voltage stress on the stator windings of the PM BLDC motor. Thus, although the ZSI supply provides single stage power conversion with reduced switching losses and short-circuit protection of the transistors, the DBI supply could be preferable. The influence of the fuel cell power fraction with respect to the nominal power of the traction motor on the supply design states that, for fraction less than 20%, the transistor peak current in the ZSI supply is less than that in the DBI supply but this fraction requires high values for the inductors. However, as the current solicitation is an important factor affecting the cost of the supply, ZSI can be preferred in the cases where the major power source is a battery.

PM BLDC motors are characterized by their trapezoidal phase-back. To ensure flat and maximum torque per ampere, motor requires injection of square-wave phase current (SqPC) synchronized with the flat portion of the corresponding back-emf. For this VSI uses its 120° mode of operation, in which two phases conduct at time. Therefore commutation of phase currents takes place with the periodicity of 60° to ensure square-wave nature of the current. In practice dynamics of the phase currents during phase commutation is affected by the phase inductance and limited voltage supply causing deviation in the ideal behavior of the phase currents. This deviation causes issues of: a) torque ripple, causing discomfort in driving, and b) dropping speed torque characteristic, limiting the use of PM BLDC drive up till the nominal speed. Phenomenon of phase current commutation is addressed in chapter 4. At first correlation of phase currents with the motor torque is established and then behavior of the phase currents during commutation as a function of speed and defined motor specific quantity is discussed analytically. Outcome of the analytical results was used to explain the issues of torque ripple and dropping speed-torque characteristic of the motor. Based on the results, nominal speed and torque of the motor were defined. As a case study an in-wheel surface mounted PM BLDC motor drive used in a light electric vehicle is considered for the experimental verification of the obtained analytical results.

Chapter 5 proposes sinusoidal phase-current (SPC) supply over SqPC supply as a solution to utilize the drive up till the nominal speed. In case of square-wave phase current, commutation process does not remain complementary, i.e. rate of rise or fall of commutating currents defers and affects the non-commutating current by inducting ripple. In case of sinusoidal phase current supply, as always all the three-phases continue to conduct, phase commutation remains balanced and motor offers a speed independent constant torque. For the same copper loss per phase, SPC offers 5% higher torque then

SqPC. Convenience analysis of SPC supply is carried out and the improvement in the speed torque characteristics is discussed with analytical results. A comparison of the torque ripple for the two cases show that: a) the torque ripple in case of SPC remains constant to approximately 15% up till the nominal speed after which motor fails to develop required torque, whereas torque ripple for SqPC varies from +50% to -50% from low speed to nominal speed with 0 at the mid-speed point; b) apart from a span of 22% of nominal speed around mid-speed point, torque ripple for SPC remains much lower compared to the case of SqPC. Thus the utilization of SPC supply in place of SqPC supply can provide significant improvements in overall torque performance. Experimental arrangement has been made for the implementation of both kinds of the supply strategy. Implementation is discussed starting from the generation of reference currents from the estimated rotor position to the injection of phase-currents through proper control action. At last speed-torque characteristic is evaluated experimentally.

Use of space-phasor/vector approach for the phase variables is quite common with the ac motors having sinusoidal back-emf and phase current. Vector approach for the case of PM BLDC motor is never explored, reasoning behind it could be that this is operated by a non-sinusoidal phase currents. Chapter 6 has revisited the PM BLDC drive behavior in stationary plane by presenting a quite simple and powerful approach to understand the drive. Under ideal case of commutation for a supply interval, back-emf vector continues to move along the side of a regular hexagon; during this time current vector remains stationary representing the vertex of a regular hexagon. At the end of the supply interval, back-emf changes its slope to the next corresponding side of the hexagon and current makes instantaneous transition to the current vector representing next state. Thus trajectory of both current and back-emf vectors in stationary plane follow a regular hexagon. Re-visitation is extended to explain the electrical dynamics of the motor in case of non-ideal phase commutation during the low and high speed zone. All the results obtained in the a-b-c plane were validated in a simple way in stationary plane showing the strength of the vector approach for PM BLDC motor drive.

Another important issue of an electric vehicle is the limited autonomy due to the lower energy density and longer charging time of on-board batteries compared to the internal combustion engine (ICE) vehicles. Possibilities of fast and ultra-fast charging of the batteries are becoming popular and are in their immature stage of research and marketization. Another option is the utilization of solar energy to support the batteries. Utilization of solar energy for light electric vehicles have constraints of limited available on-board space and lower efficiency of PV-panel. Even under such constraints, for the cases where mobility of the vehicle is limited within the city, solar energy can be utilised to assist energy sources like battery. In Chapter 7 integration of a PV panel with an electric mini-car available in the laboratory is considered. At first basics of solar irradiation, photovoltaic and datasheet specifications together with the characteristics of a photovoltaic module are discussed. Then a discussion on the estimation of solar irradiance available in Padova (Italy), is carried out for the calculation of input and output power of a considered

0.487 sq-meter, 20-cell multi crystalline PV panel. Based on these data a conventional dc-to-dc boost converter is designed and built up as an interface between panel and dc-link. Appropriate control is implemented through DSP to track the maximum power point (MPP). Analytical loss model is developed for the explanation of the variations in gain, losses and efficiency as observed during the experimentation under varying solar irradiance. Efficiency of the converter is evaluated analytically and experimentally and found to be in agreement, showing the accuracy of the developed loss model. 5% increase in the autonomy of the electric mini-car is estimated, which is a good assistance by the mounted PV panel of such a small area.

Chapter 2

Electric Mini-car

Summary: An electric mini-car called Birò and produced by Estrima, is considered as a case of study and platform for the experimental verification of the proposed strategies for the improvement of the performance of the propulsion system of a light electric vehicle. Strategies for the improvement in performance and their experimental verifications are discussed and presented in separate chapters. Present chapter discusses the electric propulsion system for the mini-car. Traction and supply system of an electric vehicle is discussed in reference to the mini-car. Discussion on the construction, operation and torque speed characteristics of permanent magnet brushless dc motor used is placed under traction system. Discussion on the lead-acid battery together with the specification, I-V characteristics of the battery used for the vehicle is also presented under supply system.

2.1 Electric propulsion system of the electric mini-car

In general propulsion system of any electric vehicle can be grouped into two parts, termed as traction system and the supply system. The two systems are connected to each other through a high voltage dc-link. Traction motor together with voltage source inverter (VSI) is the part of the traction system. Supply system consists of series connected batteries as energy source. In some of the cases, battery is also assisted by the fuel cell or photovoltaic panel in combination with ultra-capacitor are also preferred. In addition with the above mentioned two parts, vehicle also requires a control system to manage the various constraints as required and under the limits with the help of voltage and current sensors. Due their higher torque and power density as well as cost and compactness compared to the motor of other types of the same size, permanent magnet brushless dc (PM BLDC) motors are preferred as traction motor. *Figure 2.1.1* shows the schematic of an electric vehicle propulsion system (EVPS).

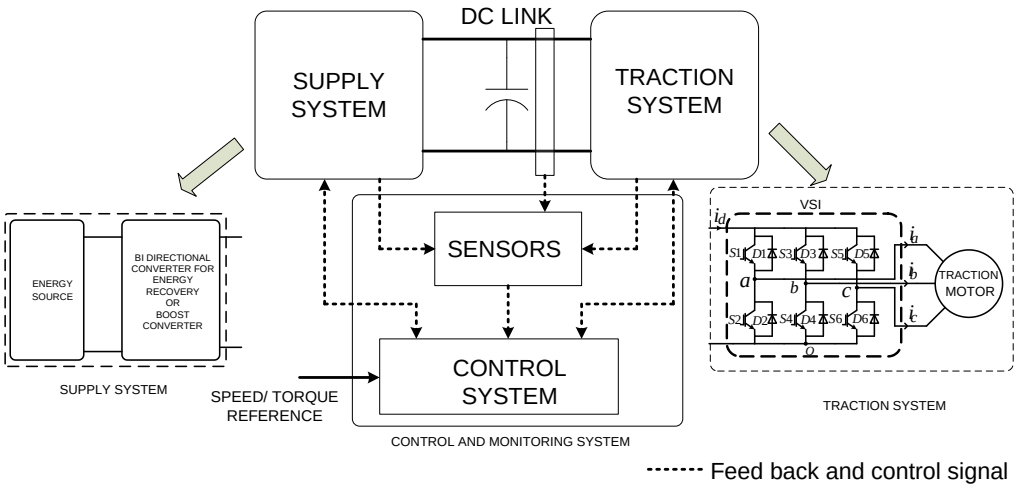

Fig. 2.1.1 Schematic of an electric vehicle propulsion system (EVPS)

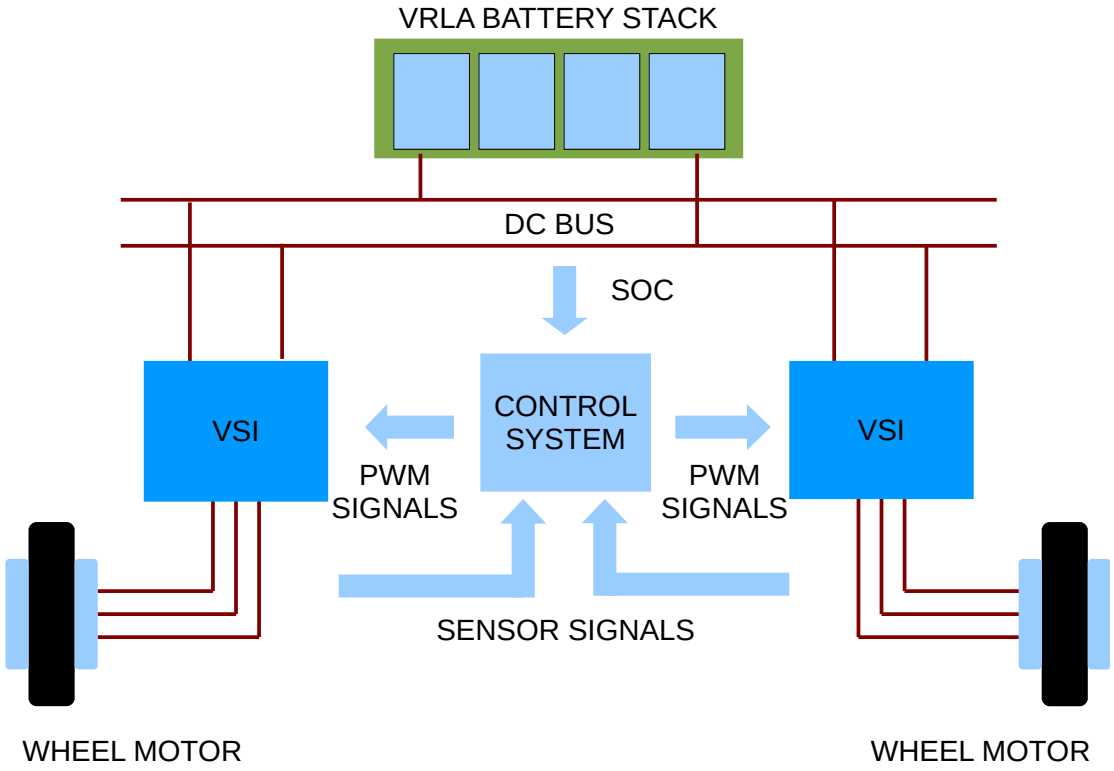

Fig. 2.1.2 Schematic of electric propulsion system of BIRO

Schematic of the electric propulsion system of BIRO is shown in *Figure 2.1.2*. It consists of two 48V (*nominal line-to-line voltage)* and 2 kW in-wheel PM BLDC motors with the peak power of 4kW. Each motor is connected to a 48V dc-link through two separate VSI. Four series connected 12V, 100Ah VRLA batteries are used to feed 48V dc-link. Control system of BIRO monitors the state of charge (SOC) of the battery, generates the PWM signals for VSI to be operated under specific condition as per drivers requirement under constraints set by the manufacture. On board batteries can be charged from 220V, 5A ac power point at home or in parking places.

2.2 Traction System

Traction motors for an electric vehicle application require certain characteristics as discussed in [1] and are listed as:

- High torque and power density
- High starting torque for low speeds and high power for high speed cruising.
- Wide speed range, with a constant power operating range 3 to 4 times the base speed.
- Higher efficiency over wide speed and torque range including low torque operation.
- Intermittent overload capability typically twice the rate torque for short duration.
- High reliability and robustness appropriate to vehicle environment.
- Acceptable cost.

Induction motor, switch reluctance motor and the permanent magnet brushless (PMBL) motor are possible candidates for the purpose. PMBL motors are efficient, offer higher

torque and power density together with reliability and robustness compared to the motors of the same size and other types. Therefore PMBL motors are preferred for the electric vehicle application. These motors cannot be operated by the direct connection to ac or dc supply just like in case of induction or dc motors respectively. Rather these need a VSI, whose switches are operated as per the angular position of the rotor. Angular position of the rotor is sensed by the Hall sensors mounted on to the stator of the motor. This is one of the reasons why VSI is considered as a part of traction system in place of part of supply system. *Figure 2.2.1* shows the layout of traction system.

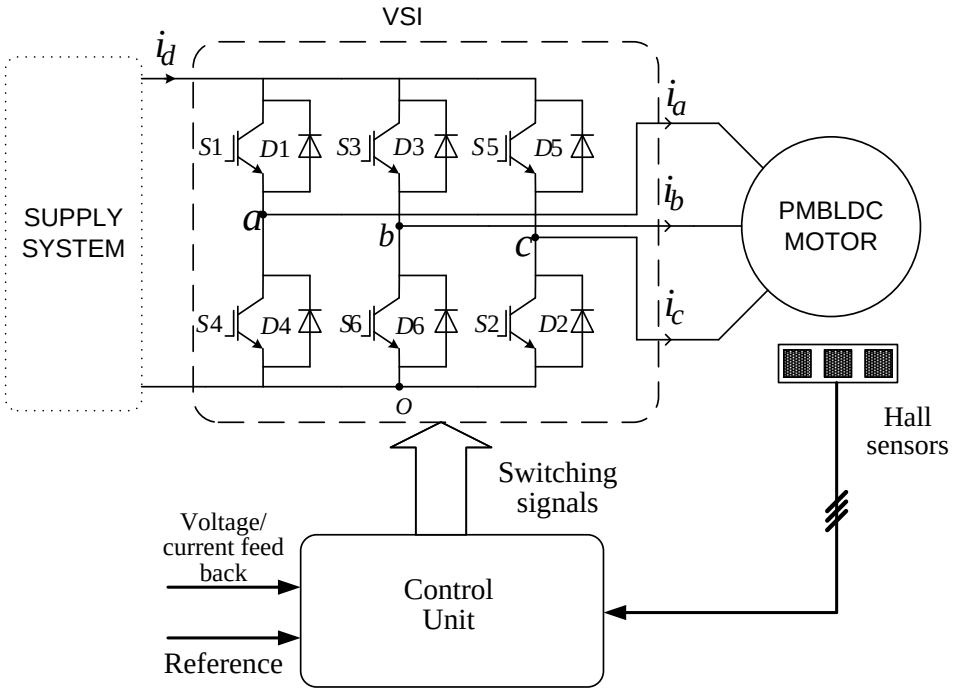

Fig. 2.2.1 Traction system of a PM BLDC motor (*general layout*)

As per the nature of stator back-emf PMBL motor are classified as PM BLDC motor if back-emf is trapezoidal in shape and PM BLAC motor, if the shape is sinusoidal one. For light and medium power application PM BLDC motor are considered due to higher torque and power density. Since our case study lies in this power range, therefore discussion on PM BLDC motor is considered.

2.2.1 Permanent Magnet Brush-less DC (PM BLDC) motor

The mini electric car utilizes an in-wheel surface mounted PM BLDC motor and falls in the category of radial flux machine. In such type of motor permanent magnets are mounted on the surface of the rotor and are termed as surface mounted permanent magnet (SPM) motors. The two possible configurations of the placement of the magnet on the surface of the rotor are shown in *Figures 2.2.2a* and *2.2.2b*. In first type of structure, rotor core is non-salient type and the magnets are mounted on the surface of the rotor as shown in *Figure 2.2.2a*. Whereas in another type permanent magnets are placed between the teeth of the salient rotor structure as shown in *Figure 2.2.2b*. Stator winding is distributed one similar to that of an induction motor.

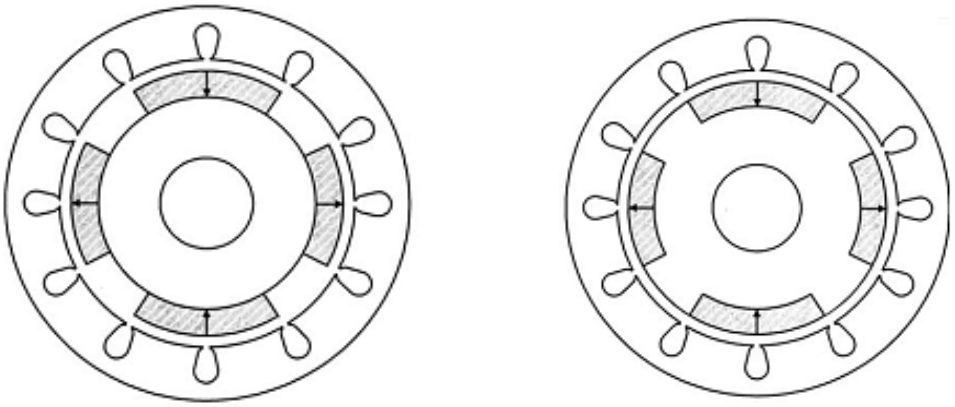

(a) (b)

Fig.2.2.2. Permanent-magnet brushless motor topologies with PM on rotor [1]: a) surface-mounted; b) surface inset.

PMBL DC motor utilizes 180° and 120° arc magnets, as shown in *Figures 2.2.3a* and *2.2.3b* respectively, to produce rectangular distribution of flux density in the air gap [2].

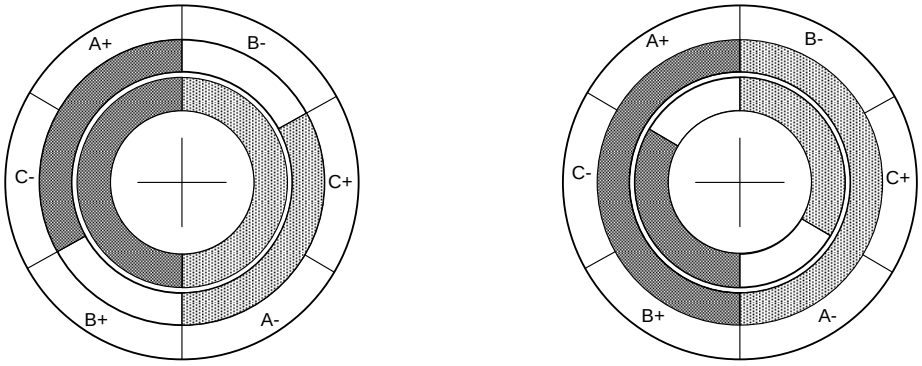

(a) (b)

Fig.2.2.3. PMBL DC motor with: a) 180° arc magnet; b) 120° arc magnet [2]

180° arc magnet motor requires injection of 120° duration of square wave current to produce the flat and ripple free torque, whereas 120° arc magnet requires injection of 180° duration of square-wavewave current. Current injection requirement makes it compulsory for the stator winding to be star connected in the first case and delta connected in the second case. Although in case of motor with 120° arc magnet phase current is of 180° duration, line to line current remains of 120°; duration thus same switching strategy and control can be applied in this case.

Structure of the motor used in mini-car is similar to *Figures 2.2.2a* and *2.2.3a* with the difference of the use of 8 pole pairs of magnet in place of 4 pole pairs as shown in figures.

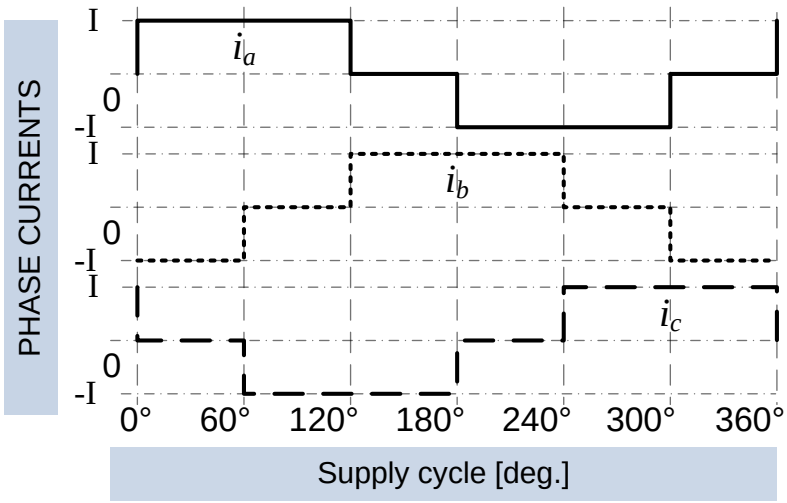

Fig.2.2.4. Stator winding currents in case of 180° arc magnet motor.

Figure 2.2.4 shows the stator currents for 180° arc magnets. In the case of motor with delta connected stator winding circulating current result in unnecessary winding losses and increased torque ripple whereas in case star connected winding only two phases conduct at a time so losses are lesser, therefore 180° arc magnet motor is preferred in place of 120° arc magnet motor.

2.2.2 Principle of operation of PM BLDC motor

Consider 180° arc magnet PM BLDC motor with three phase star-connected stator winding as shown in *Figure 2.2.5* and the stator winding is energised by a quasi-square wave type phase current with 120° of conduction duration, as shown in *Figure 2.2.4*. In further following considerations have been made:

- arc magnet is considered as equivalent to a bar permanent magnet with the axis perpendicular to the arc magnet.
- even though the stator windings have multiple number of coils per phase per slot connected in series, it is considered that this arrangement is equivalent to a single coil per phase.
- the coils for the three phases are displaced from each other by 120° electrical angle in space.
- positive and negative phase currents are represented by cross and dot respectively.
- whenever the coil is excited by a current, it produces a flux and can be considered as equivalent to North-South pole pair of an electro-magnet depending upon the direction of entrance of the current into the coil.
- axis of the electro-magnet pair coincides with the axis of the coil perpendicular to the area of the coil and passing through the centre of the coil.
- as the stator coils are stationary and fixed on the stator core, position of the electromagnets remain same. Their polarity changes as per the excitation of the coil decided by the switching of the VSI, to obtain current pattern as shown in *Figure 2.2.4*.

Figures 2.2.5a and *2.2.5b* shows the PM BLDC motor layout and its equivalent layout for

the discussion of principle of operation.

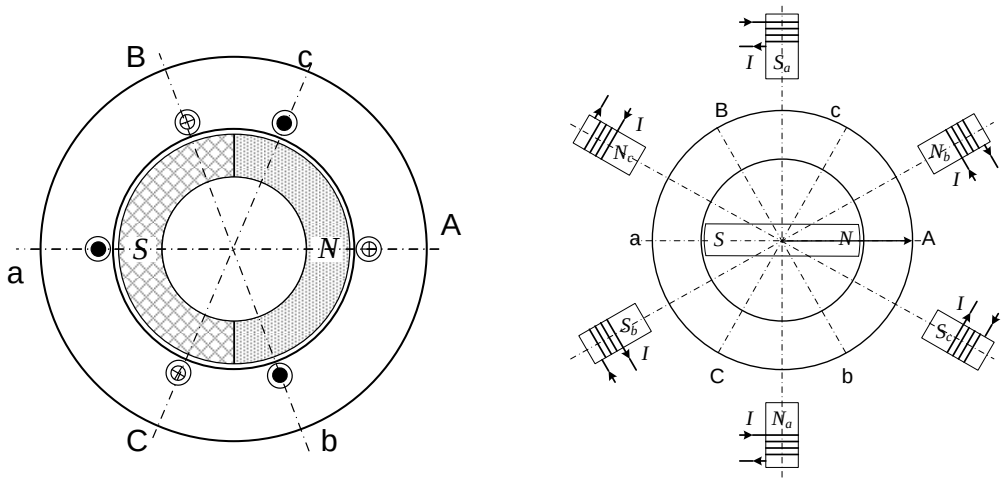

(a) (b)

Fig.2.2.5. a) PMBL DC motor with: 180° arc magnet and star connected stator coils and; b) Equivalent arrangement of PM BLDC motor with electro-magnet pairs in place of stator coils.

Considering that rotor angular position θ is measured in anti-clock direction from the initial rotor position shown in *Figures 2.2.5b* and *2.2.6a*. Square-wave phase current of 120° duration is fed to the motor by proper switching of the switches of the VSI as per the rotor position [*Figure 2.2.1*]. *Figures 2.2.6a* to *2.2.6c* shows the rotor position and equivalent electro-magnet pole pairs for the stator coils due to the excitation by the phase currents as shown in *Figure 2.2.4*. For the angular position from $0° \leq \theta < 60°$ as phase-A current is positive and phase phase-B current is negative. This result in development of electro-magnet pole pairs (N_a, S_a) and (N_b, S_b) due to the coils, A-a and B-b respectively. *N* and *S* poles of the rotor are attracted by electro-magnets (S_a, S_b) and (N_a, N_b) respectively. This results in rotation of the rotor (bar-magnet) towards the equilibrium position shown by the dashed dotted bold line in *Figure 2.2.6a*. Equilibrium position of the pairs (N_a, N_b) and (S_a, S_b) is at 60° angular position from the initial rotor position. To this position rotor becomes stagnant and requires injection of another phase current combination to rotate further. This is achieved by turning *OFF* phase-B current and sending negative current in phase-C. This results in the development of pole-pairs (N_c, S_c) for phase-C as shown in *Figure 2.2.6b*. During the angular position $60° \leq \theta < 120°$, rotor pole *N* is attracted by poles S_a and S_c and S pole is attracted by N_a and N_c in anti-clock wise direction and result in the further rotation of the rotor towards the equilibrium position of the rotor pole shown by the bold dotted line at an angle $\theta = 120°$ where rotor again becomes stagnant. To avoid the stagnancy current through phase-A coil is turned *OFF* and positive current is fed to the phase-C coil by maintaining negative current through phase-B coil. This results in the development of pole-pairs (N_b, S_b) as shown in *Figure 2.2.6c*. During the angular position $120° \leq \theta < 180°$, *N* is attracted by the poles (S_c, S_b) and *S* is attracted by (N_c, N_b) in anti-clock wise direction. Thus rotor keeps rotating towards the next equilibrium position at $\theta = 180°$, as shown in *Figure 2.2.6c*. After *180°* of angular position reversal of the phase-A current takes place to repeat the same cycle during negative half. This keeps the rotor to rotate in anti-clock wise direction.

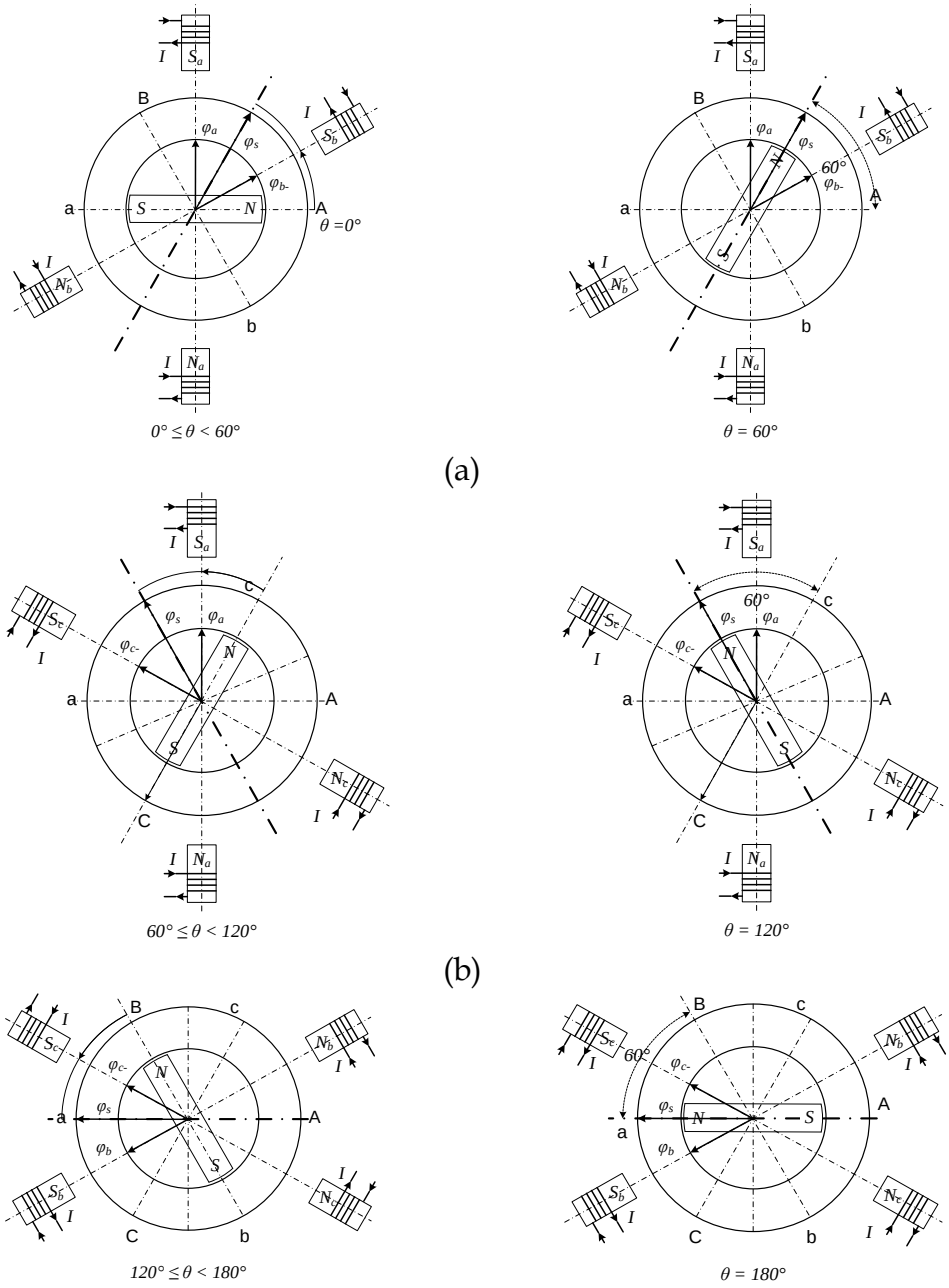

Fig.2.2.6. Poles of the equivalent electro-magnet and position of the rotor as per the excitation of the stator coils during rotor positions: a) $.0° \le \theta \le 60°$; b) $60° \le \theta \le 120°$; c) $120° \le \theta \le 180°$;

As explained that, at the end of each 60° of the angular position, rotor achieves equilibrium position and becomes stagnant, therefore to keep rotor in rotation, injection of phase current in proper sequence is required as per the rotor angular position. Information of rotor position is obtained with the help of three Hall sensors mounted on the stator. Hall sensors work on the principle of Hall Effect and give either high of low signal of 180° duration. When a hall sensor comes in the vicinity of north-pole of the arc-magnet it gives high signal and when it comes in the vicinity of south-pole it get reset. φ_s is the resultant

of the stator fluxes in the air gap to the excitation of two required phases responsible for the rotation of rotor. Under ideal conditions φ_s remains constant in magnitude and occupies six angular positions corresponding to the six equilibrium positions of rotor or six active states of VSI with a shift of 60° electrical angle.

Phase back-emfs, Hall sensors and corresponding Hall states are shown in *Figure 2.2.7a* and the conducting transistors corresponding to a different Hall states,and phase currents are shown *2.2.7b*.

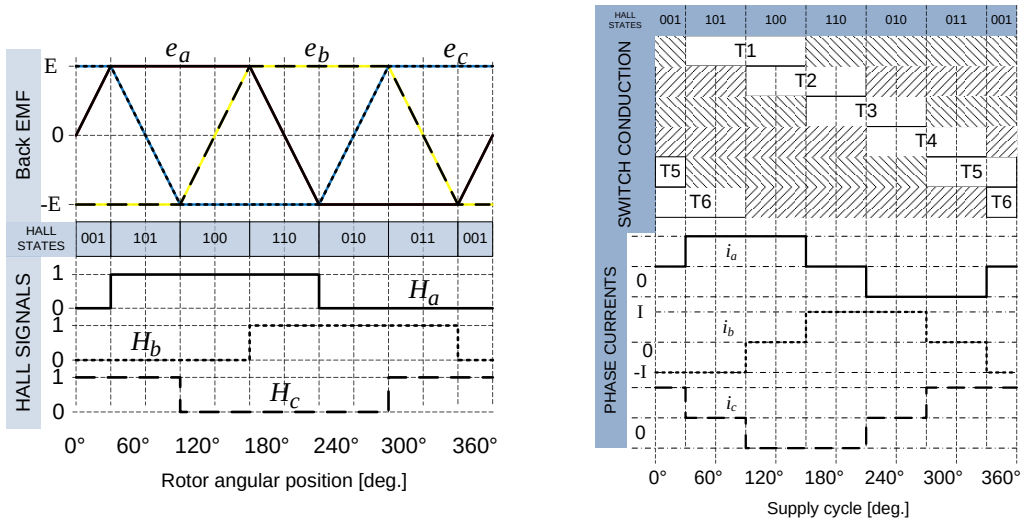

(a) (b)

Fig.2.2.7. a) Phase back-emf and Hall sensor signals as per rotor position; b) phase currents through the VSI as per Hall-states.

2.2.3 Torque-speed characteristics of PM BLDC motor

Interaction of the flux due to stator currents and flux-linkages due to the flux from the PM through the stator coil result in the development of the required motor torque to drive a load. Flux linkage to the stator coil appears as back-emf.

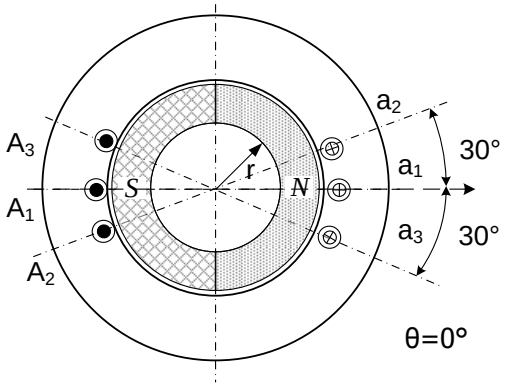

Fig.2.2.8. Layout of two pole 180° arc magnet PM BLDC motor with three series connected coils per phase (only phase *A* coils are shown)

Trapezoidal behaviour of the back emf of the motor can be explained with the help of a two pole 180° arc magnet three phase PM BLDC motor with 18 slots (*three slots per pole per phase*). Let N_C is the number of turns of a full pitch coil of say, phase *A* as shown in

Figure 2.2.8. Each phase winding is single layer and consists of three coils with their axes displaced by the 30° from the central coil in positive and negative directions. For the present case for phase *A* the three full pitch coils are a_1-A_1, a_2-A_2.and a_3-A_3. Consider the rotor angular position at $\theta = 0°$. Flux linkages λ through the coils varies linearly from zero to maximum value with the rotation of rotor.

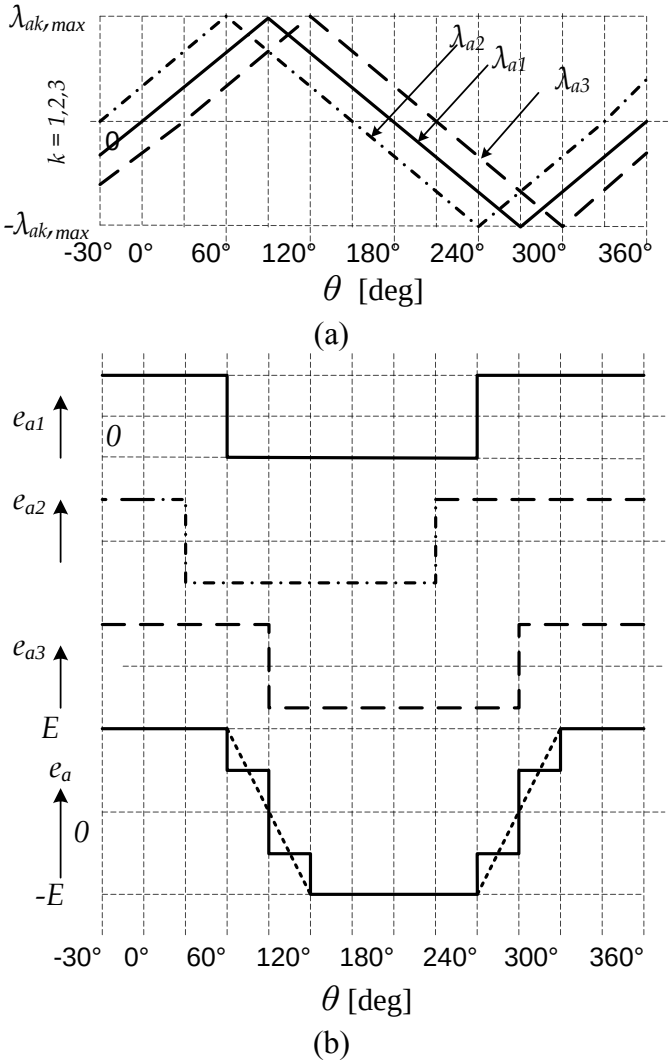

Fig. 2.2.9. Flux linkages and back-emf of phase A coils.

Flux linkage in coil a_1-A_1 as shown in *Figure 2.2.9a*, during the angular position $0° < \theta \leq 90°$

$$\lambda_{a1}(\theta) = \frac{2}{\pi}\theta\lambda_{\max} \qquad (2.2.1)$$

where λ_{max} is the maximum value of the flux linkage through the coil a_1-A_1 and is equal to $N_C B_g \pi r l$. Where B_g is the air gap flux density. Considering that the cross and the dot represents current entering and leaving, to and from the coil respectively. Then the emf induced in the coil a_1-A_1 is expressed by (2.2.2)

$$e_{a1} = \omega_m \frac{d\lambda_{a1}}{d\theta} \qquad (2.2.2)$$

where $\omega_m = d\theta/dt$. (2.2.1) and (2.2.2) gives the expression for the emf induced in a_1-A_1 is equal to

$$e_{a1} = 2N_C B_g r l \omega_m \text{ Volt} \qquad (2.2.3)$$

Flux linkages and the back-emf for the coils a_3-A_3 and a_2-A_2 leads and lags by 30° with that of first a_1-A_1. Net flux linkage and the back emf for a phase is the sum of these quantities for the three coils of a phase. Flux linkage and back emf developed in the three coils for phase A are shown in *Figure 2.2.9b*.

Net emf e_a induced in phase *A* coil is given by the sum ($e_{a1}+e_{a2}+e_{a3}$). Magnitude of the flat top portion of e_a i.e *E* is given by

$$E = 2NB_g r l \omega_m \text{ Volt} \qquad (2.2.4)$$

where $N = 3N_C$.

Variation in the back-emf of phase *A* is shown in *Figure 2.2.9b* by continuous bold line. The dotted bold line, shows the trapezoidal behaviour of the back emf. More closeness of the back-emf with trapezoidal one is achieved by the use of higher number of slots/coils per-pole/phase and is cost concern of the motor.

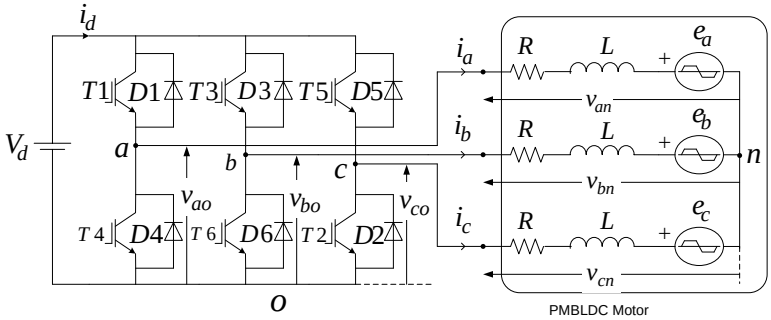

Fig.2.2.10. PM BLDC motor drive: circuital representation.

In reference with the circuital representation of PM BLDC motor, as shown in *Figure 2.2.10*, motor phase to neutral voltage is given by

$$v_{jn} = Ri_j + L\frac{di_j}{dt} + e_j \qquad (2.2.5)$$

where $j = a, b$ and c; v_{Pn} is phase to neutral voltage; i_P is phase current and e_P is phase back-emf.

Magnitudes of the flat portions of the back-emf are equal to $\pm E$, where *E* is equal to $k\omega_m$, ω_m is the motor speed and *k* is the motor back-emf constant and is equal to $2NB_g rl$. Portions of the back-emf representing the transition from $+E$ to –E and vice-versa are in general expressed as

$$e_j = s\left(1 - \frac{6}{\pi}\theta_t\right)E \qquad (2.2.6)$$

where θ_t is the angular position of the rotor with respect to the starting positions of the transition. s can be +1 or -1 depending upon whether the transition is from +*E* to –*E* or –E to +E respectively. Supply angular frequency, ω_e is n_p times the motor angular speed ω_m, where p is the number of pole pairs of the motor.

Instantaneous motor torque developed is equal to

$$\tau_m = \frac{1}{\omega_m} \sum_{j=a,b,c} i_j e_j \qquad (2.2.7)$$

If the square-wave phase currents are maintained in synchronism with the flat portion of the corresponding back-emf, (2.2.7) results in a constant value of the motor torque given by (2.2.8).

$$\tau_m = \frac{2EI}{\omega_m} = 4NB_g lrI = 2kI \text{ N-m} \qquad (2.2.8)$$

Thus the electrical torque developed by the motor is similar to that of a dc shunt motor with constant filed flux.

In steady state (2.2.5) and (2.2.7) reduces to

$$\left.\begin{aligned} V_d &= 2IR + 2E \\ T &= 2kI \end{aligned}\right\} \qquad (2.2.9)$$

(2.2.9) results in the speed torque characteristic of a PM BLDC motor in steady state and ideal condition and is

$$T = -\frac{2k^2}{R}\omega_m + \frac{kV_d}{R} \qquad (2.2.10)$$

In practice torque vs speed characteristic is dominantly affected by the problem of non-ideal phase commutation and the back-emf causing drop in motor torque with the increase in speed. Figure *2.2.11* shows the torque vs speed characteristics with non-ideal phase commutation.

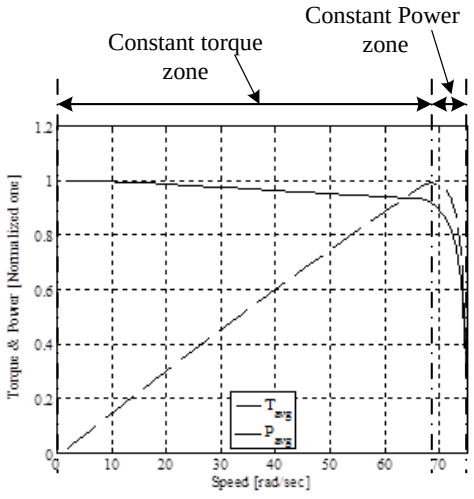

Fig.2.2.11. Speed torque characteristic of a PM BLDC motor

Constant torque and constant power zone of the motor are also labled in the figure.

2.3 Supply system

Supply system of an electric vehicle consists of battery, fuel cell, ultra-capacitor or photovoltaic (PV) module as a source of energy. In general traction motor are designed for higher terminal voltage so to reduce the problem of cu losses and the available energy sources are capable of delivering higher current at lower voltage. Therefore energy sources are either connected in series to achieve higher dc-bus/link voltage to power the motor or are connected to dc-bus through a dc-to-dc boost converter. Dc-to-dc boost converter is preferred for the cases where on board space is matter of great concern, like in the case of photovoltaic and fuel cell. Fuel cells have higher energy density and much lower power density whereas Ultra-capacitors have very high power density and much lower energy density. Thus the combination of fuel and ultra-capacitor is a perfect match. Availability of hydrogen for fuel cell is an issue due to the infrastructural requirements for the storage and distribution of hydrogen. This makes the use of battery ultra-capacitor system for the vehicles as secondary choice, since batteries have sufficient energy density to meet the vehicle requirements. Although Li-ion batteries have much higher energy density and less charging time compared to lead acid batteries, cost of the Li-ion batteries is a decision factor for its application in low-cost light electric vehicles. Electric mini car under consideration uses four lead-acid batteries to provide traction and auxiliary load.

2.1.1 Valve Regulate Lead-acid battery

Electric mini car under consideration uses four, LPC12-100 (12V, 100Ah) Valve Regulated Lead Acid (VRLA) batteries as an energy source. *Figures 2.3.1a* and *2.3.1b* show VRLA battery and its internal arrangement, respectively.

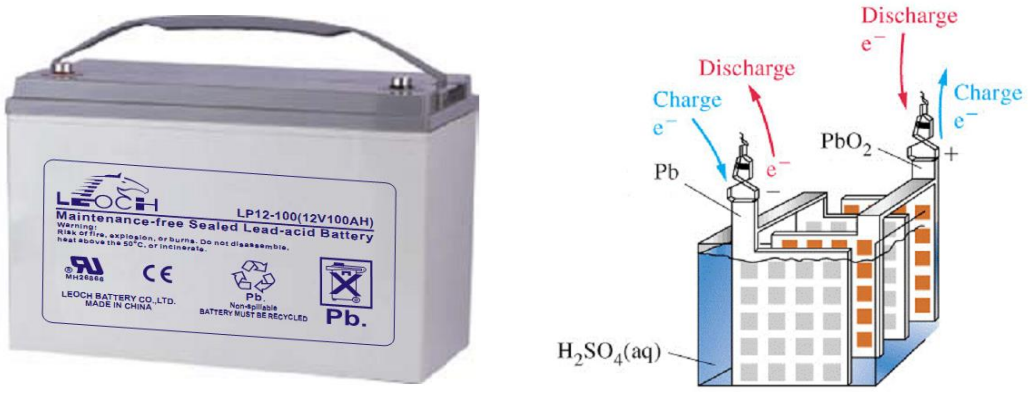

(a) (b)

Fig.2.3.1. VRLA battery: a) LPC12-100 (LEOCH) b) internal arrangement.

VRLA batteries are widely used energy source in industry. Anode (positive plate) and cathode (negative plate) of this battery are placed in the electrolyte. To avoid short circuit between anode and cathode, non-woven fabric of fine glass fibres are used as separator. Electrodes are made of lead-tin-calcium alloy in the form of grid frame as shown in *Figure 2.3.1b*. Porous portion of the anode frame holds PbO_2 as an active material, whereas cathode holds spongy lead as an active material. Dilute sulphuric acid is used as an electrolyte to provide medium for the conducting ions during the electrochemical reaction in the battery. Electrochemical reactions taking place at anode-cathode are written as

Positive plate

Discharge

$PbO_2 + 4H^+ + SO_4^{--} + 2e^- \rightleftarrows PbSO_4 + 2H_2O$

Charge

Negative plate

Discharge

$Pb + SO_4^{--} \rightleftarrows PbSO_4 + 2e^-$

Charge

Discharge

$PbO_2 + 2H_2SO_4 + Pb \rightleftarrows PbSO_4 + 2H_2O + PbSO_4$

Charge

During the discharge of the battery, spongy Pb at cathode combines with sulphuric acid to form $PbSO_4$with the release of electrons and H^+ ions. These electrons are received at anode, with the conversion of PbO_2 into $PbSO_4$ and formation of water. During the charge process of the battery, $PbSO_4$ at anode get converted into PbO_2 at anode and Pb at cathode.

Characteristics of the battery used in electric mini-car, as per the data sheet provided by the manufacture are shown in *Figures 2.3.2a* and *2.3.2b*.

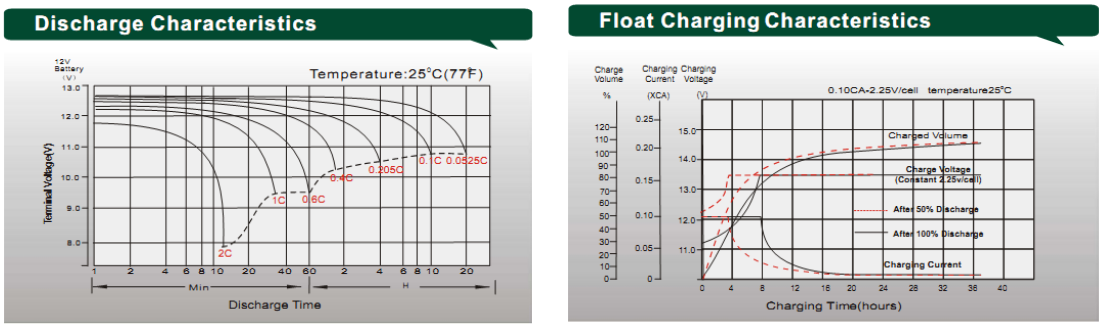

(a) (b)

Fig.2.3.2. LPC12-100 characteristics: a).discharge; b) charging (*Source: LEOCH, LPC12-100 data sheet*)

VRLA battery exhibits almost flat terminal voltage characteristics as it is shown in *Figure 2.3.2a*. Flatness of the terminal voltage for VRLA battery depends upon the capacity *C* being utilised. For smaller value of capacity it remains flat, whereas for larger values of capacity terminal voltage variation is wide as are shown in *Figure 2.3.2a*. *Figure 2.3.2b* shows the variations in the charging characteristics (charging current, charged voltage and charging volume) for the two cases of discharge, first when the charging started with 100% discharge (bold lines) and second when charging is started with 50% of discharge (dashed line). Half discharge requires much lesser volume of charge and time as compared to the case of full discharge. In case of full discharge charging time is almost double of that in case of half discharge.

2.1.2 Mixed storage system in mini-electric car

LPC12-100 contains 6 cells connected in series with the nominal voltage of 2V. Each cell and hence the battery has defined lower and upper threshold values for the terminal voltages. As for the present case during the discharge if terminal voltage of the battery falls below 36V, supply should be disconnected from the load. Similarly in the case of charging or regenerative braking if terminal voltage rises above 56V battery should be disconnected from the charger or load. Further during acceleration batteries are required to deliver current peaks which results in the drop of the battery voltage so the autonomy of the vehicle

is affected. Likewise during deceleration or regenerative breaking, a large amount of current are required to be absorbed by the batteries. To improve the performance of the vehicle autonomy and battery performance a battery ultra-capacitor mixed storage system for mini-electric car is developed in the line of ECE 15, in the laboratory by another group of researchers [3]. Circuital arrangement of the PM BLDC motor drive with mixed storage system is shown in *Figure 2.3.3*.

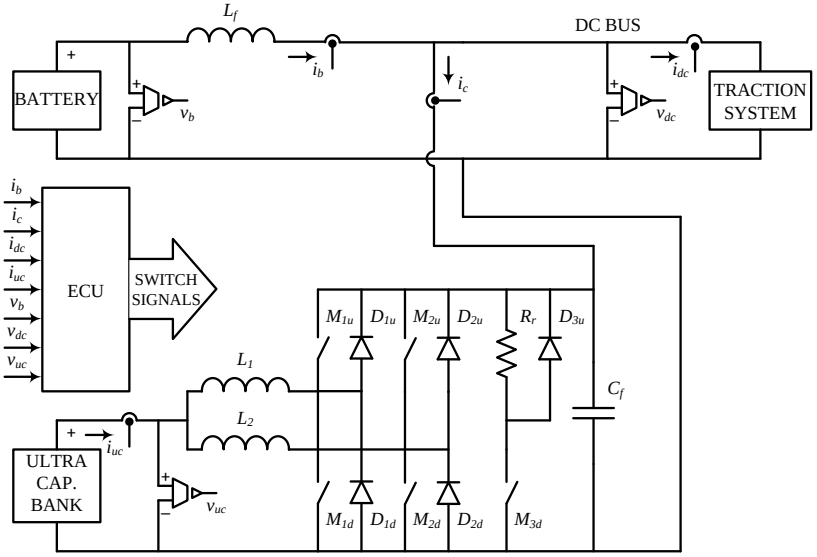

Fig.2.3.3. Battery ultra-capacitor mixed storage system for mini-electric car.

This storage system uses an interleaved bi-directional dc-to-dc converter in between dc-bus and a properly sized ultra-capacitor bank. Current pulses during the acceleration are supplied by the ultra-capacitor bank and pulses are absorbed during the regenerative braking. Overall control strategy maintains a proper balance between the energy transferred from the battery for the regular traction operation and the operation during transients.

2.4 References

[1] Chan, C. C, "State of the Art of Electric, Hybrid, and Fuel Cell vehicles", *Proceedings of the IEEE*, vol. 95, no. 4, pp. 704-718, April 2007.

[2] Miller, T. J., "Brushless Permanent-Magnet and Reluctance Motor Drives", clarendon Press, Oxford 1989.

[3] Bertoluzzo, M., Buja., G., Pede, G. and Puccetti, A., "Hybrid-battery super-capacitor storage system for electric city cars", Proceedings of EEVC, Brussels, Belgium, October 26-28, 2011.

Chapter 3

Converter Topologies for Electric Propulsion

Summary: PM Brushless dc motors used in traction applications like electric vehicle are generally designed for higher terminal voltage to minimize the cu-losses. Whereas the available on board energy sources like, batteries, hydrogen fuel cell, photovoltaic modules are capable of delivering higher current at comparatively lower voltage. Thus they require some circuital arrangements that can meet the higher dc link voltage requirement to feed the traction motor. Output of these sources is dc in nature. Possible arrangements which are being widely considered for the purpose are: a) use of series combinations of such sources and b) use of dc-to-dc boost converter. Use of only series combination of energy source is quite common, in case of batteries. Consider an example, to have 48V dc bus either four 12V, 100A.h (f.i. *LEOCH* battery) series connected battery or two 12V, 200A.h series connected battery with a boost converter with two times boost can be used. In the second case A-h of the battery is doubled to have same performance. But this case does not give any improvement in terms of weight and volume. Rather in second case for battery weight and volume are 5 kg and 1.12 times respectively more. However use of boost converter in case of fuel cell and photovoltaic panel gives a significant improvement in terms of weight and volume reduction of energy source. Traction system uses voltage source inverter (*VSI*) to convert dc-bus voltage to alternating terminal voltage for motor so converter strategy for electric propulsion can be termed as: VSI supply, when series connected energy source is used and dc boost inverter (*DBI*) supply when VSI with dc-to-dc boost converter is used. Z-source Inverter (*ZSI*) supply is another solution to have voltage boost. It can provide single stage power conversion from source to motor with the advantages of reduced switching losses and has an inherent protection from undesirable turn *ON* of the transistors of the same leg of a voltage VSI due to EMI noises. Present chapter considers DBI and ZSI supply topologies for the comparison in terms of sizing of passive components, defined voltage stress and current stress. Fuel cell stack is considered as a source of energy because of its prospect for electric vehicle propulsion. In the case of fuel cells energy recovery during regenerative braking is not possible and it has wide variation in *V-I* characteristics, so it requires quit tight norms for the regulation of voltage and current. Therefore fuel cell as an energy source can be considered as worst case situation. PM BLDC motor is considered as traction motor.

3.1 Dc-to-dc boost inverter (DBI) supply for PM BLDC motor drive

Consider a PM BLDC motor drive fed by a fuel cell with nominal voltage V_{FC} which is less than the nominal voltage V_N of the motor. Necessary voltage boost is obtained by the use of a dc-to-dc boost converter voltage with gain *G*. Gain G is defined by the ratio of nominal terminal voltage of the motor to nominal voltage of the fuel cell, i.e. $G = V_N/V_{FC}$ and is greater than one. Traction system utilizes a conventional VSI to fed alternating square-wave voltage to the motor. Such an arrangement is termed as dc boost inverter *DBI*. Schematic of the drive with *DBI* is shown in *Figure 3.1.1*. *Figure 2.2.7* shows the variation of the back-emf of the motor and the switching of the VSI transistors to achieve square-wave phase current of 120° with the electrical angular position of the rotor. Magnitude of the average voltage across the motor terminals varies from 0 to V_N as per the motor speed whereas the magnitude of the phase current varies from 0 to the nominal value I_N as per

the torque demand. Variation in the voltage and current is achieved by chopping anyone of the conducting transistors.

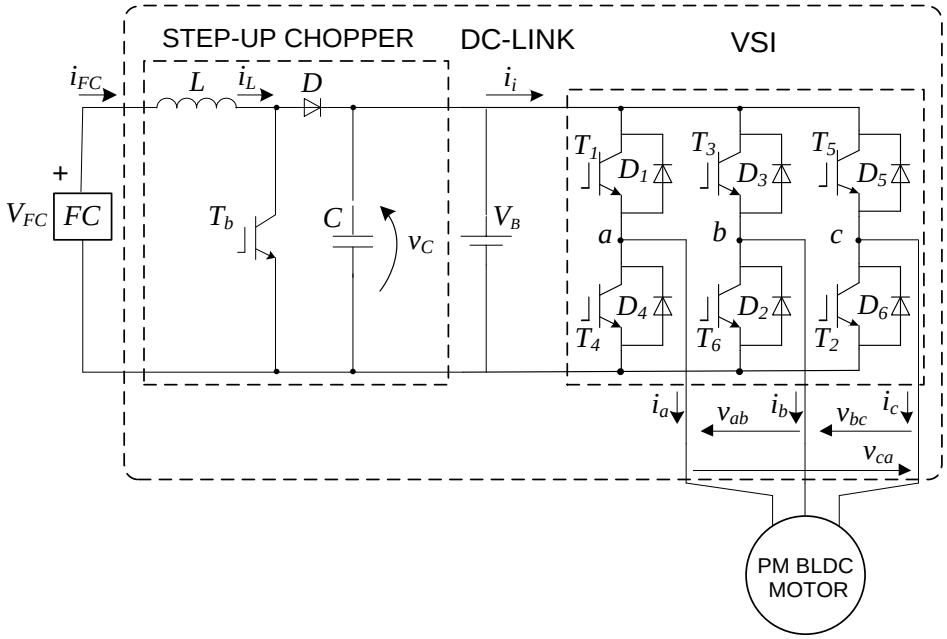

Fig.3.1.1. Schematic of *DBI* for *PM BLDC* motor drive

As the energy recovery is not possible during regenerative braking, it is considered that the fuel cell *FC* is assisted by a battery. As the battery imposes a constant voltage to the dc bus and it has to power motor over the full voltage range, therefore its voltage must be equal to V_N i.e $V_B = V_N$.

DC-to-dc boost chopper boosts the lower fuel cell voltage V_{FC} to V_N by operating the transistor T_b. Let T_s be the switching period of T_b. During the *ON* time of the transistor, diode *D* gets reversed biased and current i_L through the inductor *L* increases to store the energy. During this time VSI is fed by the output capacitor *C* and the battery. When the transistor T_b is turned *OFF* energy stored in the inductor together with the energy from the fuel cell is transferred to the output capacitor and battery to maintain the higher voltage at dc bus. Under the hypothesis that the internal impedance of the capacitor is much lesser than that of the battery, it can be considered that the energy transferred is entirely absorbed by the capacitor and the presence of the battery can be neglected for the sizing of the capacitor. During the steady state operation balance of the energy stored in inductor and energy transferred to the capacitor results in

$$V_N = \frac{1}{1-\delta_N} V_{FC} \qquad (3.1.1)$$

Where δ_N is the duty cycle of T_b to produce nominal voltage V_N. Gain of the boost converter is given by

$$G = \frac{1}{1-\delta_N} \qquad (3.1.2)$$

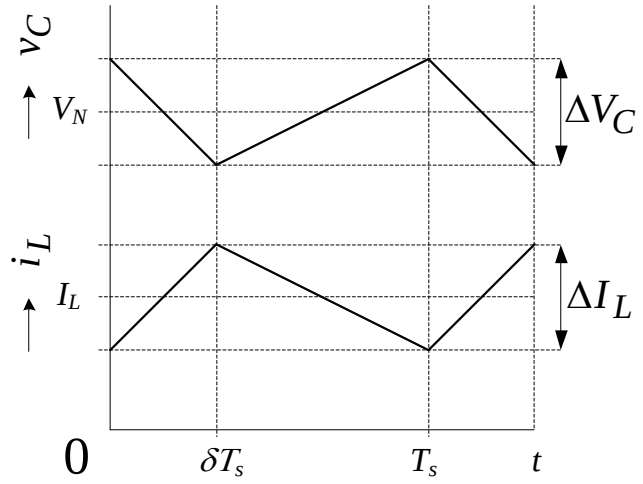

Fig.3.1.2. Capacitor voltage and inductor current of the boost converter

Figure 3.1.2 shows the variation in the capacitor voltage and the inductor current of the boost converter for *DBI*. Average value of the voltage across the capacitor remains equal to the nominal voltage V_N.

3.2 Z-source Inverter (*ZSI*) supply for PM BLDC motor drive

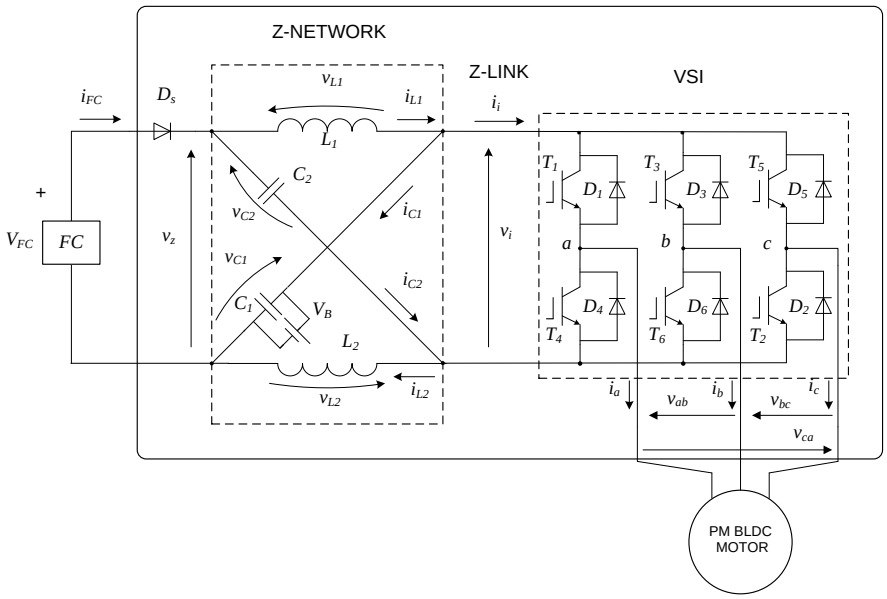

Fig.3.2.1. Schematic of *ZSI* for a *PM BLDC* motor drive

Figure 3.2.1 shows the schematic of a *PM BLDC* drive with *ZSI* supply. Conventional ZSI uses a diode D_s, and a symmetric z-network to interface a low voltage energy source with a VSI. Z-network is formed by two inductors L_1, L_2 and two capacitors C_1, C_2. Diode D_s is used to prevent the reverse current through the low voltage energy source (fuel cell). Battery is connected in parallel with C_1 to assist the fuel cell during the regenerative braking. z-network is designed to be symmetric, therefore L_1=L_2=L and C_1= C_2 = C. These ensure that, the voltages across and current through the two inductors and capacitors to be equal. For inductors these are, v_L, and i_L respectively and for capacitors, v_C, and i_C

respectively.

ZSI has three modes of operation: i) active (*A*) mode when the VSI delivers any one of its six active voltage vectors, ii) open (*O*) mode when the VSI deliver any one of its two zero voltage vector, and iii) shoot-through (*T*) mode when both the transistors of a leg (or of all the three legs) of the VSI are intentionally turned *ON* to create a short-circuit at Z-link to have boost function. During the steady state average voltages across the two inductors remain zero therefore battery has to impose the average value of the voltage v_i across the Z-link and it must be equal to V_N to supply the motor over the full voltage range.

$$V_i = V_B = V_N \tag{3.2.1}$$

This makes *ZSI* to boost fuel cell voltage V_{FC} to motor nominal voltage V_N by introducing mode-*T* during modulation period of *VSI*.

Let T_c is the modulation period of *ZSI*. d_a, d_o and d_t are the duty-ratio of the modes *A*, *O* and *T*, respectively with $d_a+d_o+d_t=1$. During mode-*A*, fuel cell supplies energy to *VSI* as well as to the capacitors through the inductors and continues until sum of the voltages across the capacitors becomes greater than or equal V_{FC}. During this interval current through the inductors continue to decrease with the increase in capacitor voltages. At the end of mode-*A*, shoot through state is imposed to make the parallel combination of pairs (L_1, C_2) and (L_2, C_1). This allows the transfer of energy from capacitors to inductors, which increases the boost capability of *ZSI*. Mode-*T* continues until capacitor voltages fall below V_{FC}.

Under the hypothesis that T_c is short enough, the Z-link delivers a current i_i that is nearly constant within each mode; it can be expressed as

$$i_i = \begin{cases} I_d & \text{mode } A \\ O & \text{mode } O \\ I_t & \text{mode } T \end{cases} \tag{3.2.2}$$

where I_d is the current absorbed by the PM BLDC motor and I_t is the shoot-through current. As the current i_L into the inductors of the Z-network is nearly constant during T_c, therefore it is denoted with I_L. Waveforms of the voltages v_i, v_L and the currents i_i, i_C are shown in *Figures 3.2.2a and 3.2.2b*, respectively. It is worth to note that the Z-link voltage v_i is not constant rather it is pulsating.

The average value of v_i as a function of V_{FC} is given by

$$V_i = B_a V_{FC} \tag{3.2.3}$$

where B_a is termed as average boost factor and is expressed as

$$B_a = \frac{1-d_t}{1-2d_t} \tag{3.2.4}$$

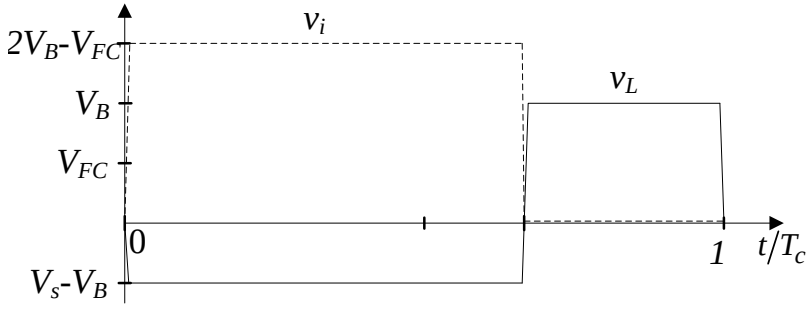

(a)

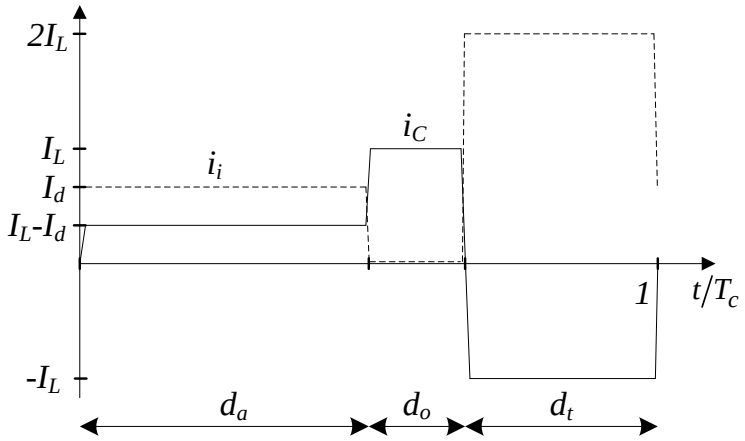

(b)

Fig.3.2.2. Plots of a) voltages and b) currents for Z-link during modulation period T_c.

From (3.2.4), it can be concluded that d_t has an upper limit of 0.5. The peak value of v_i as a function of V_{FC} is given by

$$\hat{v}_i = B_p V_{FC} \tag{3.2.5}$$

where B_p is termed as peak boost factor and is expressed as

$$B_p = \frac{1}{1-2d_t} \tag{3.2.6}$$

(3.2.4) and (3.2.5) point out that introduction of mode-T (d_t>0) results in boost factor greater than 1, with a step-up of both the average and peak values of the voltage v_i with respect to V_{FC}. By (3.2.3) to (3.2.6), the ratio between the peak and average values of v_i is given by (3.2.7) and tends to 2 as d_t tends to 0.5.

$$\frac{\hat{v}_i}{V_i} = \frac{1}{1-d_t} \tag{3.2.7}$$

The peak value of v_i, in turn, determines the average value of the line-to-line VSI output voltage according to

$$V_{LL} = (1-d_t-d_o)\hat{v}_i \tag{3.2.8}$$

The current I_L through the inductors as a function of I_d is given by

$$I_L = \frac{(1-d_t-d_o)}{1-2d_t} I_d \qquad (3.2.9)$$

The shoot-through current I_t as a function of I_d is given by

$$I_t = \frac{2(1-d_t-d_o)}{1-2d_t} I_d \qquad (3.2.10)$$

As just like mode-*O*, mode-*T* introduces a zero vector at the output of the *VSI*, application of mode-*O* is not convenient when the nominal voltage is required at the terminals of the VSI. Therefore only modes-*A* and *T* can be considered. Similar to *DBI* supply, under the hypothesis that the internal impedance of the capacitor is much less than that of battery, the energy stored into the inductors during modes *A* and *T* is entirely swapped with the capacitors and the presence of the battery can be neglected for the sizing of capacitors.

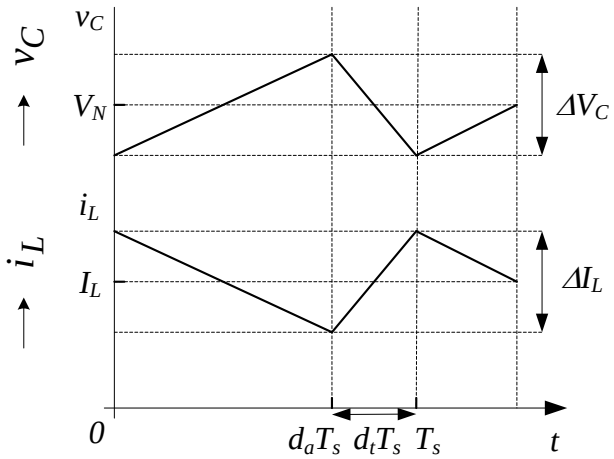

Fig.3.2.3. Capacitor voltage and inductor current for the z-network of *ZSI* supply.

Figure 3.2.3 shows the variation in i_L and v_C as a function of the time. In this case also average value of v_C is equal to V_N. V_N as a function of V_{FC} and nominal value of d_t , $d_{t,N}$ and vice versa $d_{t,N}$ as a function of V_N and V_{FC} be written as

$$V_N = \frac{1-d_{t,N}}{1-2d_{t,N}} V_{FC} \Leftrightarrow d_{t,N} = \frac{1}{2}\left(\frac{1-\frac{3V_{FC}}{V_N}}{1-\frac{2V_{FC}}{V_N}}\right) \qquad (3.2.11)$$

Therefore gain *G* for *ZSI* is given by

$$G = \frac{1-d_{t,N}}{1-2d_{t,N}} \qquad (3.2.12)$$

The current i_i of the Z-link is given by

$$i_i = \begin{cases} I & \text{mode } A \\ i_t = 2i_L & \text{mode } T \end{cases} \qquad (3.2.13)$$

where i_t is the shoot-through current.

3.3 Evaluation of ZSI and DBI for battery assisted fuel cell supply

DBI supply for the purpose of boost of low voltage energy source like fuel cell and photovoltaic module for traction purpose is widely accepted. ZSI needs evaluation for the case of PM BLDC motor drive due to following reasons:

- It provides single stage power conversion (dc-to-ac) with dc source voltage boost.
- Inherent protection from shorting of transistors of the same leg, due to EMI noises.
- Reduced switching losses compared to DBI.
- In case of PM BLDC motor drive two transistors of VSI conduct during a regular interval of operation, whereas applications with ZSI and the comparisons available, consider only the cases where three transistors conduct during regular interval of operation.
- Like dc-link voltage in case of DBI, Z-link voltage is not continuous; rather it varies from 0 to $2V_i$-V_{FC}. [*Figure 3.2.2a*] For example to have average z-link voltage equal to 48V with 24V input dc voltage, peak value of the z-link voltage is 72V.

Current and voltage ripple in a supply topology are quite important points of consideration for the life cycle of battery/fuel cell and dc link voltage regulation. Current and voltage ripples are limited by the proper sizing of the passive components. Voltage and current stress on the switching devices are other factors for the selection of a supply topology as these are related with cost and reliability of a topology.

Present section considers the discussion on above mentioned issues with the help of defined evaluation factors related as a function of current and voltage stress on the transistors. Fuel cell stack is considered as a source of energy because of its prospect for electric vehicle; also it is a worst case situation where energy recovery during regenerative braking is not possible and requires quit tight norms for the voltage and current regulation due to its widely varying V-I characteristics. PM BLDC motor is considered as traction motor. As the DBI is the widely accepted topology so it is considered as a reference to make a formal comparison.

3.3.1 Evaluation factors

3.3.1.1 Defined evaluation factors

Total voltage solicitation VS: defined as the sum of the maximum voltage V_M across the transistors as a fraction of $6V_N$, where 6 are the transistors of the VSI supply.

$$VS = \frac{\sum_{i=1}^{n} V_{M,i}}{6V_N} \qquad (3.3.1)$$

where n is the number of transistors of the topology.

Total current solicitation: There can be three possible current solicitation factors and are defined by considering the peak, rms and average current through the transistors.

Total peak current solicitation CS_p: is defined as the sum of the maximum peak current $I_{p,M}$ through the transistors as a fraction of $6I_N$.

$$CS_p = \frac{\sum_{i=1}^{n} I_{p,M,i}}{6I_N} \tag{3.3.2}$$

Total average current solicitation CS_{av}: is defined as the sum of the maximum average current $I_{av,M}$ through the transistors as a fraction of $6I_N$.

$$CS_{av} = \frac{\sum_{i=1}^{n} I_{av,M,i}}{6I_N} \tag{3.3.3}$$

Total rms current solicitation CS_{rms}: is defined as the sum of the maximum rms current $I_{rms,M}$ through the transistors as a fraction of $6I_N$.

$$CS_{rms} = \frac{\sum_{i=1}^{n} I_{rms,M,i}}{6I_N} \tag{3.3.4}$$

Transistor utilization TU: is defined as the ratio of P_T and P_N, where P_T is the *sum* of the products of the maximum voltage $V_{p,M}$ across the transistors and the maximum peak current $I_{p,M}$ through them.

$$TU = \frac{P_N}{P_T} = \frac{P_N}{\sum_{i=1}^{n} V_{p,M,i} I_{p,M,i}} \tag{3.3.5}$$

In a similar manner an evaluation factor for the passive components can be defined as is

Passive component sizing power PS: is defined as the ratio between A_T and P_N, where A_T is the sum of the product of the maximum voltage V_M across the passive components (inductors and capacitors) and the maximum peak current $I_{p,M}$ through them.

$$PS = \frac{A_T}{P_N} = \frac{\sum_{i=1}^{m} V_{M,i} I_{p,M.i}}{P_N} \tag{3.3.6}$$

where m is the number of passive components of the topology.

3.3.1.2 Evaluation factors for ZSI

When the motor operates at nominal voltage, V_{LL} must be equal to V_N. By (3.3.4), this is conveniently obtained by setting d_o=0. Inspection of (3.3.3) and (3.2.8) together with (3.3.4) discloses that both V_{LL} and V_B are equal to V_N. Then the average boost factor is equal to the required voltage gain, i.e.

$$B_a = G \tag{3.3.7}$$

By (3.3.7) and (3.2.10), d_t is expressed as

$$d_t = \frac{G-1}{2G-1} \tag{3.3.8}$$

and the peak boost factor as

$$B_p = 2G - 1 \qquad (3.3.9)$$

From (3.3.1) voltage solicitation VS for ZSI is calculated as

$$VS = \frac{2G-1}{G} \qquad (3.3.10)$$

As $V_{p,M}=B_pV_{FC}$ and V_N=GV_{FC}, (3.3.10) indicates that VS tends toward 2 as G increases. The product of VS by V_N gives the maximum voltage applied not only to the transistors of the VSI but also to the motor phases, which therefore must be properly isolated to sustain this solicitation.

Mode-T has an inverter state that does not exist in a VSI topology. It can be achieved in several ways; the most convenient one is to switch ON all the transistors of the three legs of the VSI for them to share the shoot-through current. By recognizing from (3.2.9) and (3.2.10) that $I_t/3>I_d/2$ and by assuming that i) the shoot-through current divides equally among the three legs, and ii) the motor current flows half through the upper transistor of the VSI leg feeding the motor and half through the bottom one, it comes out that the magnitude of the current i_{T1} flowing through transistor T_1 along the six motor supply angular intervals is as given in *Table 3.3.1*.

Table 3.3.1. Conducting transistors and current flowing through the transistor T1

Angular intervals & conducting transistors	mode	i_{T1}
0-π/3 & T5,T6	A, O	0
π-4π/3 & T3,T2	T	$I_t/3$
π/3-2π/3 & T1,T6	A, O	I_d
2π/3-π & T1,T2	T	$I_t/3+I_d/2$
4π/3-5π/3 & T3,T4	A, O	0
5π/3-2π & T5,T4	T	$I_t/3-I_d/2$

The currents flowing into transistors T_3, T_5, T_4, T_6 and T_2 are shifted of 2π/3, -2π/3, π, π+2π/3 and π-2π/3, respectively, from that of T_1. The maximum current solicitation of the transistors occurs when d_o=0 and the motor currents is I_N. Then, by (3.2.10) and (3.3.8), the maximum value of I_t is

$$I_{t,M} = 2GI_N \qquad (3.3.11)$$

and $I_{p,M}$ in (3.3.3) is expressed as

$$I_{p,M} = \frac{2GI_N}{3} + \frac{I_N}{2} \qquad (3.3.12)$$

For the passive components of the ZSI supply, by (3.2.9) the maximum peak current through the inductors is achieved again for d_o=0 and $I_d=I_N$ and is equal to GI_N whilst the maximum voltage across the inductors is V_B. The maximum peak current through the capacitors coincides with that through the inductors, i.e. it is GI_N. Therefore, by processing

the current values in *Table 3.3.1*, the evaluation factors of the ZSI topology are

$$\left.\begin{aligned} &VS = \frac{2G-1}{G}; \quad CS_p = \frac{3+4G}{6}; \quad CS_{av} = \frac{G}{3} \\ &CS_{rms} = \frac{1}{\sqrt{3}}\sqrt{1+\frac{(4G-3)(G-1)}{6(2G-1)}}; \quad TU = \frac{G}{(2G-1)(4G+3)} \\ &PS = 4G \end{aligned}\right\} \qquad (3.3.13)$$

3.3.1.3 Evaluation factors for DBI

Under the assumption of ideally smooth current through inductor L, during the ON-time of transistor T_c, a constant current flow through it. Magnitude of this current is equal to G times the maximum current absorbed by the *VSI*, i.e. GI_N. Thus the maximum current through inductor L is equal to GI_N and the maximum voltage across the inductor is

$$V_{L,M} = \begin{cases} V_s = \dfrac{V_N}{G} & for\ 1 \le G \le 2 \\ \dfrac{G-1}{G}V_N & for\ G \ge 2 \end{cases} \qquad (3.3.14)$$

Maximum voltage across the capacitor C is equal to V_N whereas maximum current through it is

$$I_{L,M} = \begin{cases} I_N & for\ 1 \le G \le 2 \\ (G-1)I_N & for\ G \ge 2 \end{cases} \qquad (3.3.15)$$

Therefore, the evaluation factors of the *DBI* supply become

$$\left.\begin{aligned} &VS = \frac{7}{6}; \quad CS_p = \frac{6+G}{6}; \quad CS_{av} = \frac{1+G}{6} \\ &CS_{rms} = \frac{2\sqrt{3}+\sqrt{G(G-1)}}{6}; \quad TU = \frac{1}{6+G} \\ &PS = \begin{cases} 2 & for\ 1 \le G \le 2 \\ 2(G-1) & for\ G \ge 2 \end{cases} \end{aligned}\right\} \qquad (3.3.16)$$

Evaluation factors for *ZSI* and *DBI* as a function of voltage gain are enlisted in *Table. 3.3.2*.

Table 3.3.2.Evaluation factors for ZSI and DBI as a function of voltage gain			
Supply → ↓Evaluation factors		ZSI	DBI
VS		$\frac{2G-1}{G}$	$\frac{7}{6}$
CS	CS_P	$\frac{3+4G}{6}$	$\frac{G+6}{6}$
	CS_{AV}	$\frac{G}{3}$	$\frac{G+1}{6}$
	CS_{RMS}	$\frac{1}{\sqrt{3}}\sqrt{1+\frac{(4G-3)(G-1)}{6(2G-1)}}$	$\frac{2\sqrt{3}+\sqrt{G(G-1)}}{6}$
TU		$\frac{G}{(3G-1)(4G+3)}$	$\frac{1}{G+6}$
PS		$4G$	$2 \quad for\ 1 \le G \le 2$ $2(G-1) \quad for\ G \ge 2$

3.3.2 Sizing of Transistor and Passive components as a function of voltage gain and power contribution factor for fuel cell [14]

For the sizing of passive components a 48V, 2.8kW, 600rpm wheel PM BLDC motor that propels a city scooter [13] is considered. The traction drive is powered by a 27V, 2kW fuel cell, thus requiring a voltage boost with G equal to 1.8. The fuel cell is assisted by a 48V Li-ion battery. The supply is controlled for the fuel cell to deliver the entire power up to a traction power demand of 2kW; after that, the battery participates in fulfilling the power demand with a contribution up to 0.8kW that is reached when the traction drive absorbs the nominal power.

3.3.2.1 Fuel cell power

To broaden the study case, a situation is considered where the nominal power $P_{FC,N}$ of the fuel cell is a generic fraction of the nominal power of the traction motor. Considering that power fraction is represented by x, i.e.

$$x = \frac{P_{FC,N}}{P_N} \tag{3.3.17}$$

Battery contributes to the nominal power with the quantity $P_{B,N} = P_N - P_{FC,N}$, i.e. with the fraction

$$\frac{P_{B,N}}{P_N} = 1 - x \tag{3.3.18}$$

Since the average voltage of the Z-link in the ZSI supply is equal to V_N, (3.3.17) and (3.3.18) yield, under nominal traction power demand,

$$x = \frac{\bar{I}_{FC,N}}{GI_N}, \quad \frac{I_{B,N}}{I_N} = 1 - x \tag{3.3.19}$$

where $\bar{I}_{FC,N}/G$ is the average current generated by the fuel cell and referred to the battery

side, and $I_{B,N}$ is the continuous current generated by the battery. In the study case, x is equal to 0.7, $\bar{I}_{FC,N}/G$ to 41A and $I_{B,N}$ to 17A.

3.3.2.2 Design procedure

Considering that the specifications for the current ripple through the inductors is r_i and voltage ripple across the capacitors is r_v, i.e.

$$r_i = \frac{\Delta I_L}{I_{L,N}}; \quad r_v = \frac{\Delta V_C}{V_N} \tag{3.3.20}$$

where the nominal value of current through the inductors, $I_{L,N}$, is depending on x, and ΔI_L and ΔV_C are the specified peak-to-peak excursions of current and voltage, respectively.

The design of the ZSI and DBI supplies is carried out by limiting both the ripples in (3.3.20) at 5%. Note that, while essential in sizing the passive components, the ripples can be neglected in determining rms and peak current as well as peak voltage of the devices, provided that they are sufficiently small. Since this condition is here verified, the effect of the ripples on the above-mentioned quantities will be neglected in the design.

3.3.2.3 Sizing of Transistor

From the operation of the ZSI supply and the PM BLDC motor, the peak value of the shoot-through current is given by

$$\hat{I}_t = 2xGI_N + (1-x)I_N \tag{3.3.21}$$

and the ratings of the transistors of the VSI are [12]

$$\begin{aligned} \bar{I}_T &= \frac{GI_N}{3} \\ \hat{I}_T &= \frac{\hat{I}_t}{3} + \frac{I_N}{2} = \frac{2x(2G-1)+5}{6} I_N \\ \hat{V}_T &= \frac{2G-1}{G} V_N \end{aligned} \tag{3.3.22}$$

The peak current in (3.3.22) is determined by assuming that mode T is implemented by switching ON all the three legs of the VSI and that the short-through current equally splits into the three legs.

3.3.2.4 Sizing of the passive components

By [10] and the *Figure 3.2*, the values of inductors and capacitors of the Z-network, expressed as a function of $d_{t,N}$ and the relevant current and voltage excursions, are

$$L = \frac{V_N T_s}{\Delta I_L} d_{t.N} \quad C = \frac{\bar{I}_L T_s}{\Delta V_C} d_{t,N} \tag{3.3.23}$$

where $\bar{I}_L$ is the average current in the inductors. In terms of the ripples and the nominal values of voltage and power of the motor, (3.3.23) becomes

$$L = \frac{V_N T_s}{I_{L,N} r_i} \frac{G-1}{2G-1} = \frac{V_N^2 T_s}{x P_N r_i} \frac{G-1}{G(2G-1)}$$
$$C = \frac{I_{L,N} T_s}{V_N r_v} \frac{G-1}{2G-1} = \frac{x P_N T_s}{V_N^2 r_v} \frac{G(G-1)}{2G-1} \quad (3.3.24)$$

and the values of the inductors and the capacitors can be readily calculated from the ripple specification and the data of the study case. Moreover, rms current, peak voltage and sizing power of each inductor for both ZSI and DBI supplies are enlisted in *Table 3.3.3*. Values of L and C for DBI supply are

$$L = \frac{V_N T_s}{x I_N r_i} \frac{(G-1)}{G^3} = \frac{V_N^2 T_s}{x P_N r_i} \frac{(G-1)}{G^3}$$
$$C = \frac{x I_N T_s}{V_N r_v} \frac{(G-1)}{G} = \frac{x P_N T_s}{V_N^2 r_v} \frac{(G-1)}{G} \quad (3.3.25)$$

Table 3.3.3. Circuit variable expressions for the passive components and transistors

Supply→ ↓Sizing	ZSI	DBI
$I_{L,rms}$	xGI_N	xGI_N
$\hat{V}_L$	V_N	$\max\left(\frac{1}{G}, \frac{G-1}{G}\right)V_N$
SP_L	xGP_N	$xG\max\left(\frac{1}{G}, \frac{G-1}{G}\right)P_N$
$I_{C,rms}$	$x\sqrt{G(G-1)}I_N$	$x\sqrt{G-1}I_N$
$\hat{V}_C$	V_N	V_N
SP_C	$x\sqrt{G(G-1)}P_N$	$x\sqrt{G-1}\ P_N$
$\hat{I}_T$	$\frac{2x(2G-1)+5}{6} I_N$	I_N
$\hat{V}_T$	$\frac{2G-1}{G} V_N$	V_N

3.3.3 Discussion and comments

3.3.3.1 Discussion based on evaluation factors

Table 3.3.3 enlists the expressions for the evaluation factors for *ZSI* and *DBI* in terms of voltage gain *G*. Variations of these factors have been shown in *Figures 3.3.1*. As shown in *Figure 3.3.1*a, total voltage solicitation of the ZSI supply is higher than the DBI for G

greater than 1.2; moreover, it increases with G for the ZSI while it remains constant at 1.16 for the DBI. This means that the transistors of the ZSI supply undergo higher voltage stresses compared to the DBI for G greater than 1.2, with the stress that tends to 2 as soon as G increases. On the other hand, the ZSI is supportive for G less than 1.2 due to the contribution of transistor T_c to the cost factor VS of the DBI.

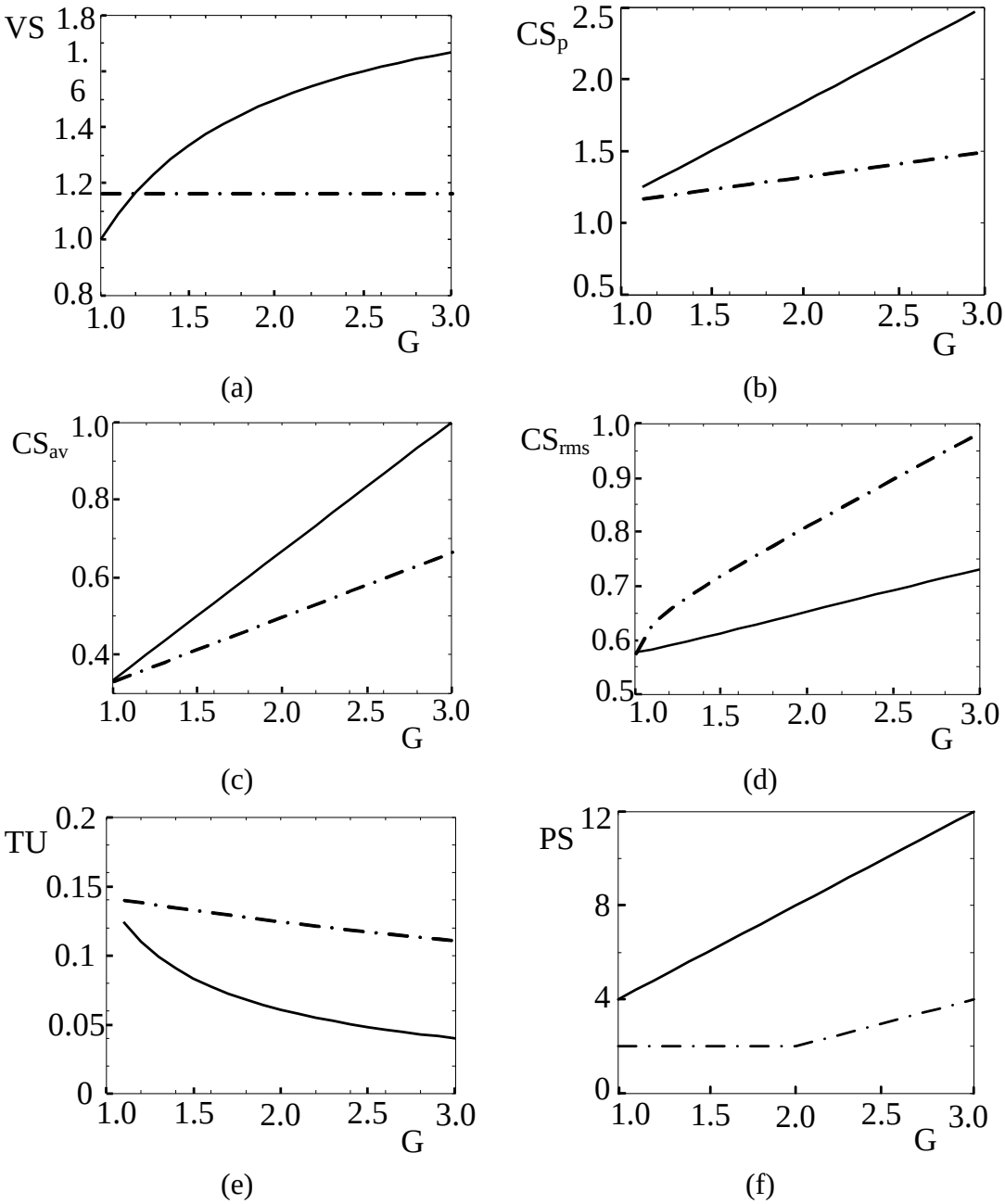

Fig.3.3.1. Variation of evaluation factors: a) *VS*; b) CS_p; c) CS_{av}; d) CS_{rms}; e) *TU* and f) *PS*, with G. (*Traces with continuous line refer to ZSI supply and that with dashed-dotted line to refer to DBI supply*)

Figures 3.3.1b, *3.3.1c* and *3.3.1d* show total current solicitations. As concerns the total peak and average current solicitations, the ZSI supply exhibits values higher than the DBI and the gap in the cost factors increases with G. On the contrary, the DBI supply is more

advantageous than the ZSI with regard to the total rms current solicitation. Higher values of peak and average current solicitation call for transistors with greater current ratings whilst high values of the rms current solicitation call for transistors with greater dissipation arrangement.

Figures 3.3.1e reveals that the total transistor utilization of the ZSI supply is poorer than the DBI, the difference between the two supplies widens faster as G increases from 1 to 2 while remaining nearly constant for G greater than 2. At last *Figure 3.3.1f* shows that the sizing power of the passive component of the ZSI supply is somewhat higher than the DBI. The main reason is that the ZSI supply includes four passive components whilst the DBI needs only two passive components. The trace for the VSI is not drawn in *Figure 3.3.1f* because this supply does not include any passive component.

3.3.3.2 Discussion based on component sizing as a function of power contribution factor

Table 3.3.3 enlists the circuit variable expressions for the passive components and transistors as a function of gain and power contribution factors. *Figure 3.3.2* shows the variation in peak transistor current, size of passive components and sizing power of the passive components with power contribution factor.

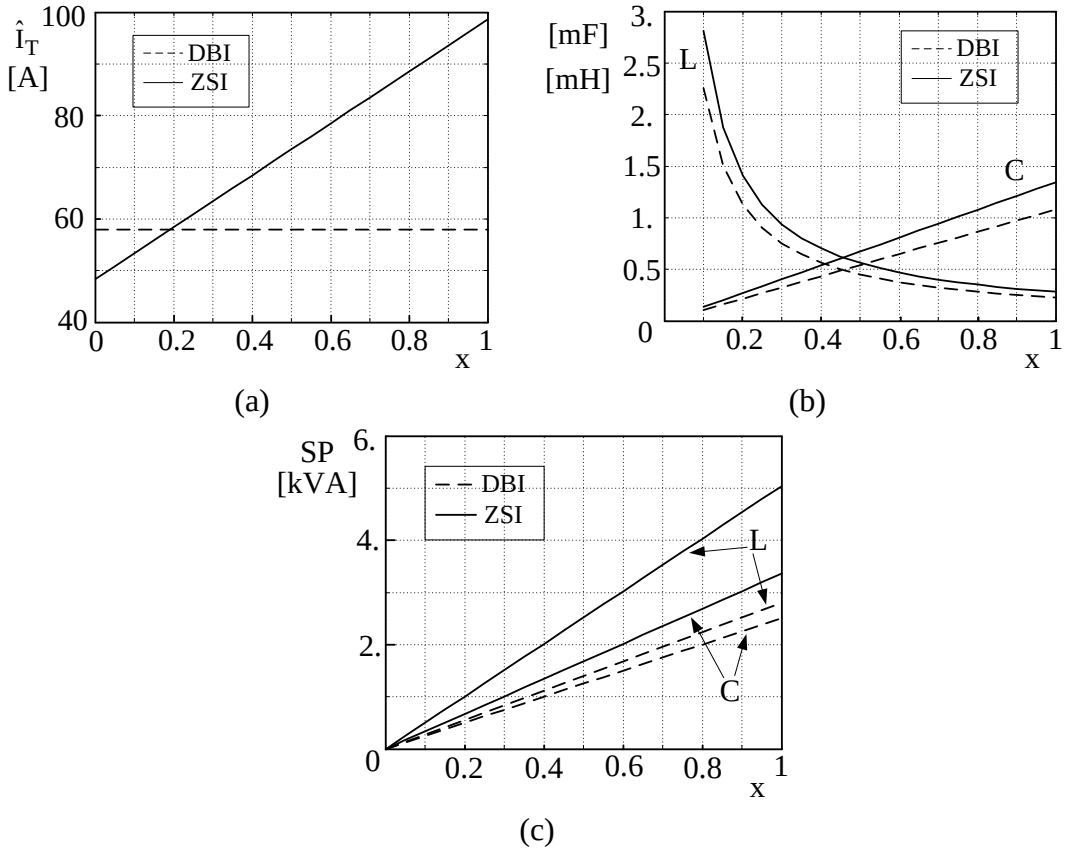

Fig.3.3.2. Variation in: a) peak transistor current, b) size of passive components, and c) sizing power of passive components, with power contribution factor *x*. (*Traces with continuous line refer to ZSI supply and that with dashed line refer to DBI supply*)

Peak current through the transistors of *DBI* supply remains constant, whereas in case of *ZSI* supply, as shown in *Figure 3.3.2a* variation with *x* is linearly increasing one. For a fraction *x = 0.2* i.e, up till 20% of power contribution form fuel cell, peak current through

the transistors are less for *ZSI* supply then *DBI* supply and keep on increasing for higher values of *x*.

Variation in the size of the inductors for the two supplies are quite sensitive for lower values of fraction *x* up till *x=0.4* and decreases with increase in *x*, after *x=0.4* variation in *L* with *x* is slower as shown in *Figure 3.3.2b*. Whereas size of capacitors increase linearly with *x*. In any case sizes of the passive components are lower for *DBI* supply than *ZSI* supply. Plots in *Figure 3.3.2b* also explain that the size of the inductors required is much higher for lower fraction of power from fuel cell compared to higher power fraction.

Variations in the sizing power for the passive components are shown in *Figure 3.3.2c*. Sizing power of the passive components increases linearly with *x*. For the higher value of *x* both the supply topologies require higher sizing power of passive components. Sizing power of inductors are noticeable one as for lower values of *x*, difference is smaller and increases widely with the increase in *x*. For all the values of *x* sizing power of *ZSI* remains higher than that of *DBI*.

Table 3.3.4. In wheel motor nominal data

Power	P_N	2.8 kW	
Voltage	V_N	48 V	
Torque	T_N	45 N·m	
Speed	ω_N	600 rpm	
SUPPLY DATA AND SPECIFICATIONS			
Fuel Cell nominal voltage	V_{FC}	27 V	
Voltage gain	G	1.8	
Inductor current ripple	r_i	5%	
Capacitor voltage ripple	r_v	5%	
Switching/modulation period	T_s	100 μs	
DESIGN RESULTS		DBI	ZSI
Chopper transistor average current	$\bar{I}_{Tb}$	33 A	
Chopper transistor peak current	$\hat{I}_{Tb}$	73 A	
Chopper transistor peak voltage	$\hat{V}_{Tb}$	48 V	
VSI transistors average current	$\bar{I}_T$	19 A	35 A
VSI transistors peak current	$\hat{I}_T$	58 A	84 A
VSI transistors peak voltage	$\hat{V}_T$	48 V	69 V
Inductor value	L	323 μH	2×402 μH
Capacitor value	C	756 μF	2×942 μF
Rms value of inductor current	$I_{L,rms}$	73 A	73 A
Peak inductor voltage	$\hat{V}_L$	27 V	48 V
Inductor sizing power	SP_L	2 kVA	2×3.5 kVA
rms value of capacitor current	$I_{C,rms}$	37 A	49 A
Peak capacitor voltage	$\hat{V}_C$	48 V	48 V
Capacitor sizing power	SP_C	1.8 kVA	2×2.3 kVA

Specifications of the wheel motor and the supply is enlisted in *Table 3.3.4*. As per the

expressions summarized in *Table 3.3.3*, values of the circuit variables and components were calculated for 1.8 times of voltage gain 70% of power contribution from fuel cell. From the calculations in *Table 3.3.4* it is clear that cost of the transistors and the components will be higher for *ZSI* due to: much higher value of transistor peak voltage and current; higher value of transistor peak voltage; bigger size of passive components and higher sizing power of passive components.

3.4 Conclusion

Two different approaches have been used to decide, which topology would be preferable for the PM BLDC motor powered by a fuel cell in assistance with a battery. Both of the approaches result into the facts that major issues, apart from the switching losses in the energy conversion unit, are voltage stress, current stresses and power utilisation of the transistors and the size of the passive components. Percentage of power contribution from the fuel cell also plays an important role in the decision for the selection of passive components and transistors. It has been found that current and voltage ratings of the transistors and sizing power of the passive components are quite higher for the ZSI supply compared to the DBI supply. This raises cost of the devices and voltage stress on the stator windings of the PM BLDC motor. Thus, although the ZSI supply provides single stage power conversion with reduced switching losses and short-circuit protection of the transistors, the DBI supply could be preferable. The influence of the fuel cell power fraction with respect to the nominal power of the traction motor on the supply design states that, for fraction less than 20%, the transistor peak current in the ZSI supply is less than in the DBI supply but this fraction requires high values for the inductors. However, as the current solicitation is an important factor affecting the cost of the supply, ZSI can be preferred in the cases where the major power source is a battery.

3.5 References

[1] Z.Q. Zhu and D. Howe, “Electrical machines and drives for electric, hybrid, and fuel cell vehicles”, Proceedings of the IEEE, Vol. 95, No. 4, pp. 746-765, April 2007.

[2] C.C. Chan, “The State of the Art of Electric, Hybrid and Fuel Cell Vehicles”, Proceedings of the IEEE, Vol. 95, No. 4, pp. 704-718, April 2007.

[3] A.F. Burke, “Batteries and Ultra Capacitors for Electric, Hybrid and Fuel Cell Vehicles”, Proceedings of the IEEE, Vol. 95, No. 4, pp. 806-820, April 2007.

[4] M. Rashid, “Power electronics: circuits, devices and applications”, Pearson Prentice Hall, Upper Saddle River, 2004.

[5] N. Mohan, T.M. Undeland and W.P. Robbins, “Power Electronics: Converters, Applications, and Design”, 2nd edition, John Wiley & Sons, New York, 1995.

[6] B.K. Bose, “Modern power electronics and AC drives”, Prentice Hall, Upper Saddle River, 2002.

[7] F.Z. Peng, “Z-source inverter”, IEEE Transaction on Industrial Applications, vol. 39, No. 2 , pp. 504-510, March/April 2003.

[8] L. Sack, B. Piepenbreier and M.V. Zimmermann, “Dimensioning of Z-source inverter for general purpose drives with three-phase standards motors”, Proceedings of the Power Electronics Specialists Conference, 2008, pp. 1808-1813.

[9] M. Shen, A. Joseph, J.Wang, F.Z. Peng and D. J. Adams, Comparison of Traditional

Z-Source Inverter for Fuel Cell Vehicles", IEEE Transaction on Power Electronics, vol. 22, no. 4, pp. 1453-1463, July 2007.

[10] W.T. Franke, M. Mohr and F.W. Fuchs, "Comparison of a Z-source inverter and a voltage-source inverter linked with a DC/DC boost-converter for wind turbines concerning their efficiency and installed semiconductor power", Proceedings of the Power Electronics Specialists Conference, 2008, pp. 1814-1820.

[11] J. Wang, L. Zhou, G. Tao and Jing Shi, "Modeling and simulation of a permanent magnet brushless DC motor fed by PWM Z-source Inverter", Proceedings of the International Conference on Electrical Machines and Systems, 2007, pp. 834-838.

[12] G. Buja, R. Keshri and R. Menis, "Characteristics of Z-source inverter supply for permanent magnet brushless motors", Proceedings of the Annual Conference of the IEEE Industrial Electronics Society, 2009, pp.1230-1235.

[13] M. Bertoluzzo and G. Buja, "Development of Electric Propulsion Systems for Light Electric Vehicles", *IEEE Trans. on Industrial. Informatics*, vol. 7 no. 3, pp. 428-435, Aug. 2011.

[14] G. Buja, R. Keshri and R. Menis, "Comparison of DBI and ZSI supply for PM brushless DC drives powered by fuel cell", Proceedings of the International Symposium on Industrial Electronics, 2011, pp. 165-170.

Chapter 4

Analytical Study of the Behavior of PM BLDC Motor Drive under Square-wave Phase Current

Summary: PM BLDC motors are fed by square-wave phase currents for the production of flat and ripple free torque. However in practice due to phase inductance and limited supply voltage, phase currents deviate from their ideal square-wave shape. This results in the problem of phase-commutation in terms of torque ripple and drop in the average torque of the motor, which increases with the increase in motor speed. Present chapter correlates the current and torque behaviours, explains the behaviour of the current and the torque during phase commutation to discuss the torque vs speed characteristics of the motor. Current and torque behaviour are explained as function of defined motor-distinctive quantity and motor speed. Finally analytical results are cross verified with the experimental result.

4.1 Correlation between current and torque behaviour

PM BLDC motors have trapezoidal back-emf with the flat top portion of 120° electrical angular duration. Therefore to achieve flat and maximum torque per ampere, injection of Square-wave Phase Currents (SqPC) synchronised with the flat portion of the corresponding phase back-emf is required. Injection of SqPC is ensured by the 120° mode of operation of VSI switches. Commutations of phase-currents take place in the interval of 60°. In practice injection and removal of phase currents during commutation are constrained by the phase inductance and limited supply voltage. Thus motor phase currents deviates from the ideal square-wave nature and cause torque ripples.

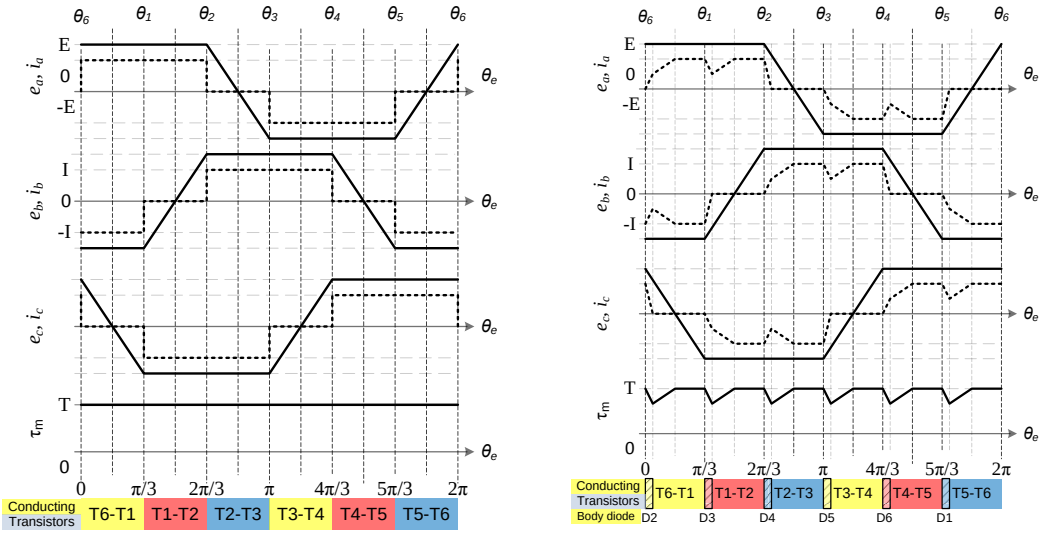

(a) (b)

Fig. 4.1.1. Back-emf, phase current and motor torque of PM BLDC motor: a) ideal behaviour; b) indicative non-ideal behaviour

Trapezoidal behaviour of the stator back-emf is shown in *Figure 4.1.1*. Ideal and non-ideal behaviour of phase currents and motor torque with rotor position are shown in *Figures 4.1.1a* and *4.1.1b*.

Consider a case of phase commutation as shown in *Figure 4.1.2* where i_a and i_b are commutating currents and i_c is a non-commutating current. i_a is an outgoing current.

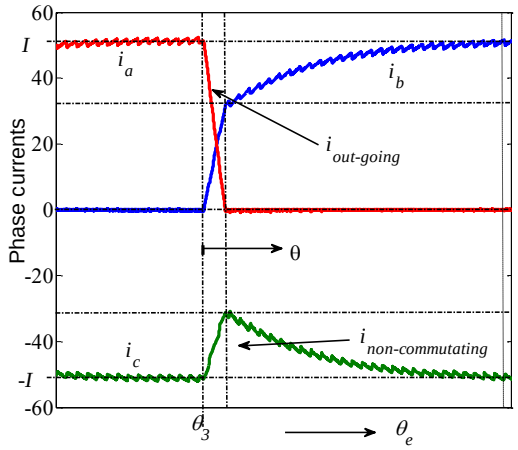

Fig. 4.1.2. Phase current commutations at θ_2 [Figure 4.1.1b]

General expression for the motor torque during commutation in terms of outgoing current and non-commutating current can be written as

$$\tau_m = 2ks\left(-i_{non\_commutating} - \frac{3\theta}{\pi} i_{out\_going}\right) \qquad (4.1.1)$$

where'k'is the motor back-emf constant and is equal to E/ω_m. ω_m is the motor mechanical speed and E is the magnitude of flat portion of the back-emf. θ is the rotor position measured from the starting instant of phase commutation and is equal to $(\theta_e - \theta_j)$. θ_j's with $j=1, ..6$ are the phase commutation instants as shown in *Figure 4.1.1*. $i_{non\_commutating}$ is the non-commutating current[1] and i_{out_going} is the outgoing current. 's' is +1 for positive current commutation[2] and -1 for negative current commutation[3]. Instantaneous torque expression (4.1) is obtained with the help of the expressions of back-emf and torque as in (2.6) and (2.7) respectively of chapter 2.

In ideal situation as the commutations are instantaneous at the instant of commutations, say θ_j, second term in (4.1) does not come into the picture and torque remains constant to the set value and no ripple in torque is observed as it is shown in *Figure 4.1.1a*. Whereas in practice, during commutation, outgoing current continues beyond θ_j due to phase inductance and vanishes after some duration. Once outgoing current vanishes, motor torque follows the non-commutating current which in turn is equal to the incoming current. Sign of outgoing current and the non-commutating current are always opposite to each other. Therefore during commutation any delay in outgoing current results in decrease or increase, i.e. ripple in the motor torque.

As the motor torque is affected by the phase currents, so it is necessary to understand their behaviour during phase commutation.

[1] Phase current which do not take part in commutation during phase current commutation is termed as non-commutating current.
[2] Positive commutation is termed for the case where commutation of two positive currents takes place.
[3] Negative commutation is termed for the case where commutation of two negative currents takes place.

4.2 Current behaviour during phase commutation

Expressions of the commutating and non-commutating currents can be derived from the Kirchhoff's equations for the circuital representation of PM BLDC motor drive as shown in *Figure 4.2.1*.

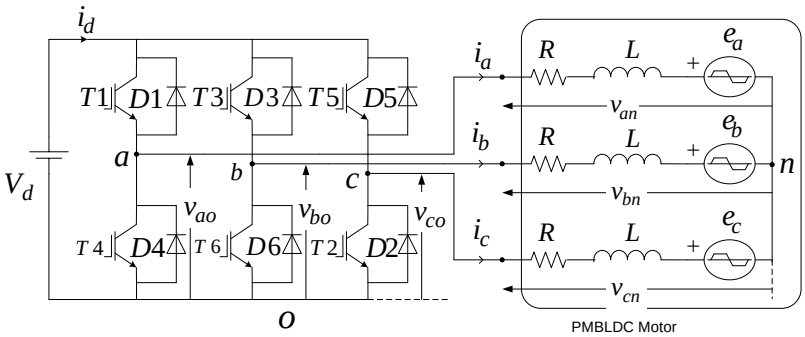

Fig. 4.2.1. Circuital representation PM BLDC motor drive

With respect to the circuital arrangements shown in *Figure 4.2.1,* circuit variables are expressed as

$$\left.\begin{aligned} v_{Pn} &= Ri_j + L\frac{di_j}{dt} + e_j \\ v_{jn} &= v_{jo} - v_{no}\,; \quad \sum_{j=a,b,c} i_j = 0 \\ v_{no} &= \frac{1}{3}\sum_{j=a,b,c}\left(v_{jo} - e_j\right) \end{aligned}\right\} \qquad (4.2.1)$$

where $j = a, b$ and c. V_{jn} is phase to neutral point voltage; i_j is phase current; e_j is phase back-emf and v_{no} is the neutral point voltage. Term 'o' corresponds to the negative terminal of the battery and the reference point for the measurement of voltages. R is the phase resistance and L is the phase inductance including the effect of mutual inductance. As the phase resistances are very small, therefore these can be neglected.

Control of PM BLDC motor can be accomplished by the control of either phase or dc-link variables voltage or current. Current control schemes for PM BLDC motor drive are popular due to their capability to maintain the phase currents near to square wave type.

For the present case dc-link current control is considered. *Figure 4.2.2* shows the schematic of dc-link current control. In the case of dc-link current control switches of the VSI are controlled as per the information of rotor position obtained from the Hall sensors in terms of six different hall-states. Once a Hall-state is over switches are left under the influence of forced commutation circuits to get turn OFF. Under such a control two switches conduct at time. The current reference I_{ref} is compared with the feedback current i_d coming from the dc-link before being manipulated by the PI regulator. The latter one outputs the duty-cycle δ for chopping one of the two conducting transistors. In the study, I_{ref} is set at the rated current magnitude I_R and the current regulator is assumed to deliver the maximum effort in presence of a small current error.

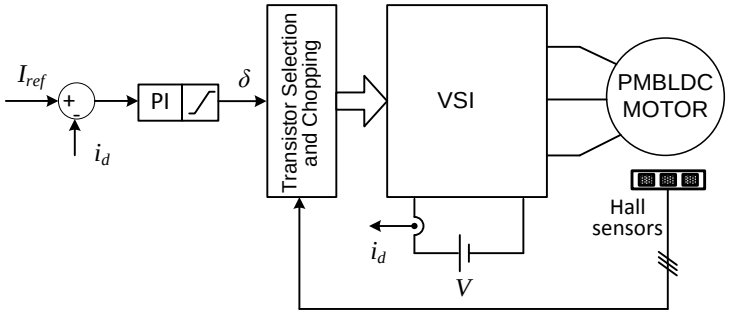

Fig.4.2.2. Current control scheme of PM BLDC motor drive

As a template, the commutation at θ_e=0 is examined. With this for a very short duration of phase commutation compared to π/3, θ_e can be considered to be equal to equal to θ. At this position, T_1 is turned ON to allow the incoming current i_a to get the value I_R, T_5 is turned OFF to force the outgoing current i_c to vanish and T_6 is kept ON. Both the incoming and outgoing transients take time to be completed.

Therefore, from (4.2.1) variation in commutating phase currents i_a and i_c with respect to time is expressed as

$$\begin{aligned} \frac{3}{2}L\frac{di_a}{dt} &= V - e_a + \frac{e_b}{2} + \frac{e_c}{2} \\ \frac{3}{2}L\frac{di_c}{dt} &= -\frac{V}{2} + \frac{e_a}{2} - e_b + \frac{e_c}{2} \end{aligned} \qquad (4.2.2)$$

Let I_R, V and Ω_b are the rated current, terminal voltage and motor speed respectively and are considered as the base values, and then the expression (4.2.2) can be represented in the form of per unit representation of phase quantities as in (4.2.3)

$$\begin{aligned} 3\Theta_m\Omega_{pu}\frac{di_{a,pu}}{d\theta} &= \frac{V}{E_R} - e_{a,pu} + \frac{e_{b,pu}}{2} + \frac{e_{c,pu}}{2} \\ 3\Theta_m\Omega_{pu}\frac{di_{c,pu}}{d\theta} &= -\frac{V}{2E_R} + \frac{e_{a,pu}}{2} + \frac{e_{b,pu}}{2} - e_{c,pu} \end{aligned} \qquad (4.2.3)$$

where $\Theta_m = n_pLI_R/2k$ is a motor-distinctive quantity expressed in radians, for most of the PM BLDC motors value of Θ_m is fraction of percentage of maximum allowed duration of commutation π/3 to maintain the rated torque; n_p is the number of pole pairs and Ω_m is the motor mechanical speed.

During the steady state, for negligible phase resistance first equation of (4.2.1) results in V/E_R=2. E_R is the back-emf at rated speed. Thus (4.2.3) reduces to the first equation of (4.2.4) and the remaining equations of (4.1.1) are written as

$$\begin{aligned} \frac{di_{a,pu}}{d\theta} &= \frac{1}{3\Theta_m\Omega_{pu}}\left(2 - e_{a,pu} + \frac{e_{b,pu}}{2} + \frac{e_{c,pu}}{2}\right) \\ \frac{di_{c,pu}}{d\theta} &= \frac{1}{3\Theta_m\Omega_{pu}}\left(-1 + \frac{e_{a,pu}}{2} + \frac{e_{b,pu}}{2} - e_{c,pu}\right) \end{aligned} \qquad (4.2.4)$$

For small values of θ_e, e_c can be approximated to its flat-top value E. For the present case

in per unit form of representation $e_{a,pu} = -e_{b,pu} = e_{c,pu} = \Omega_{pu}$. Solution of (4.2.4) results in the expressions of phase-A and phase-C currents as in (4.2.3)

$$i_{a,pu}(\theta) = \frac{1}{3\Theta_m}\frac{2-\Omega_{pu}}{\Omega_{pu}}\theta$$
$$i_{c,pu}(\theta) = 1-\frac{1}{3\Theta_m}\frac{1+\Omega_{pu}}{\Omega_{pu}}\theta \qquad (4.2.3)$$

Current i_b of the non-commutating phase is given by

$$-i_{b,pu}(\theta) = i_{a,pu}(\theta)+i_{c,pu}(\theta) = 1+\frac{1}{3\Theta_m}\left(\frac{1-2\Omega_{pu}}{\Omega_{pu}}\right)\theta \quad (4.2.4)$$

Once the switch *T5* is turned OFF and *T1* is turned ON, keeping *T6* ON, incoming current i_a starts rising through *T1* and *T6*. At the same time outgoing current i_c freewheels through *T6* and body diode *D2* until it extinguishes. Three states of the inverter before during and after the end of commutation are shown in *Figures 4.2.3a, 4.2.3b and 4.2.3c* respectively.

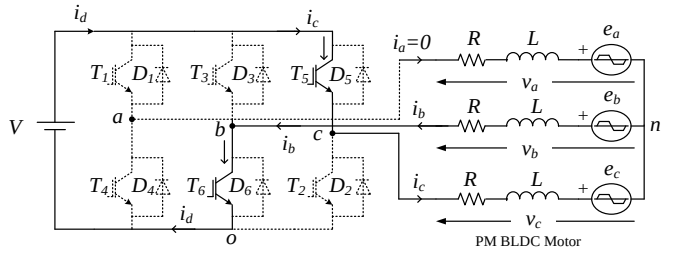

(a)

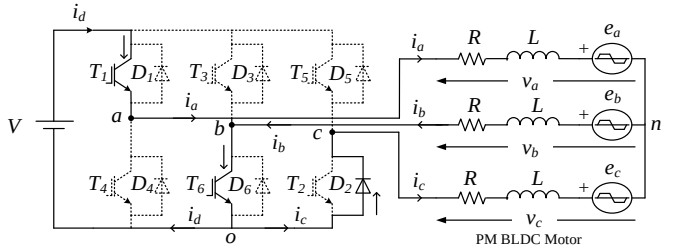

(b)

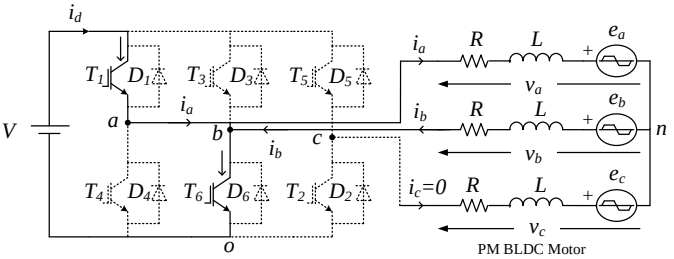

(c)

Fig. 4.2.3. Phase currents a) before; b) during and c) after the commutation $\theta_e=0$.

Depending upon the rate of rise or fall of the commutating currents, which in turn is a function of speed, either of commutating current can reach to their final value earlier or simultaneously. Three possible cases are: a) incoming current i_a reaches to final value I_R before the outgoing current i_c vanishes [Fig. 4.2.4a]; b) i_a reaches to final value after i_c

vanishes [Fig. 4.2.4b] and c) both of i_a and i_c reaches to their final value at the same instant [Fig. 4.2.4c].

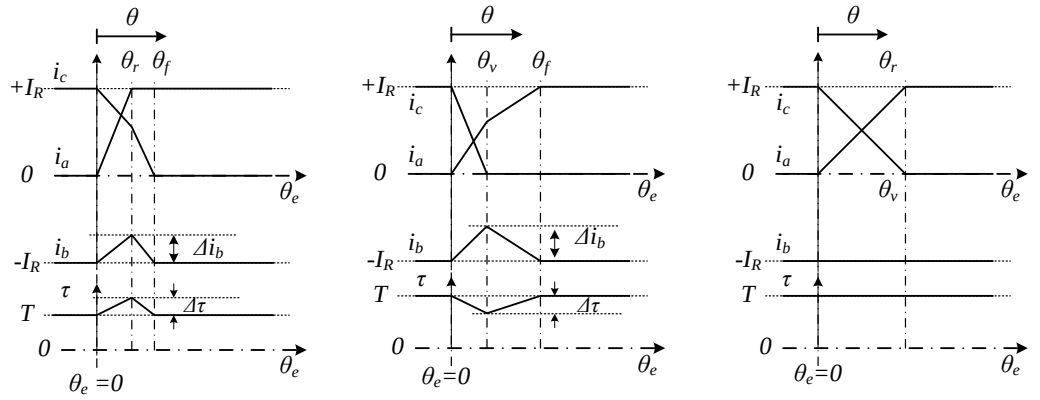

Fig. 4.2.4. Phase commutations with: a) $\theta_r < \theta_v$; b) $\theta_r > \theta_v$; and c) $\theta_r = \theta_v$

Therefore from (4.2.3) rise interval θ_r of i_a and vanishing interval θ_v of i_c are given by

$$\theta_r = 3\Theta_m \frac{\Omega_{pu}}{2-\Omega_{pu}}$$
$$\theta_v = 3\Theta_m \frac{\Omega_{pu}}{1+\Omega_{pu}} \qquad (4.2.5)$$

Expressions for θ_r and θ_v are not valid at the same time. Θ_r is less than θ_v in the speed zone $\Omega<\Omega_b/2$ (low-speed zone) whilst θ_r is greater than θ_v in the speed zone $\Omega>\Omega_b/2$ (high-speed zone). It is clear that the commutation interval consists of two parts: in the first part both the commutating currents are subjected to transients toward their final values whilst in the second part only one of them is subjected to the transients. The angular interval taken by the slowest commutating current to reach its final value is denoted by θ_f and represents the (total) commutation interval.

In the case of $\theta_r < \theta_v$, behavior of i_c can be explained the help of KVL equation for its freewheeling path written as in (4.2.6)

$$-2L\frac{di_c}{dt} = e_c - e_b - L\frac{di_a}{dt} = 2E - L\frac{di_a}{dt} \qquad (4.2.6)$$

Once i_a reaches to its final value, it is modulated to maintain the desired value. Thus second term in (4.2.3) vanishes after θ_r and increase in slope of i_c takes place.

Along the commutation interval, current i_b undergoes a fluctuation due to unbalanced behavior of the commutating currents. The fluctuation is superimposed to the constant amplitude of $-I_R$ and attains its maximum magnitude at the angle where the quicker of the commutating currents reaches its final value.

In terms of voltage quantities, the low-speed zone is encountered when $V>4E_R$ and the high-speed zone when $V<4E_R$. The speed $\Omega_b/2$ separates the two zones. For this speed value, θ_r is equal to θ_v, no unbalance occurs in the commutating currents and i_b does not undergo any fluctuation. The transients of both the commutating currents and the non-

commutating current in the two speed zones are exemplified in the upper graphs of *Figure 4.2.4*. The traces clearly show the different behavior of the currents in the two speed zones. Therefore it is convenient to study separately in each speed zone the torque characteristics ensuing from the behavior of the commutating currents.

4.3 Torque behaviour during phase commutation

In per unit form of representation, expression of the motor torque in (4.1.1) reduces to

$$\tau_{m,pu} = s\left(-i_{non\_commutating,pu} - \frac{3\theta}{\pi} i_{out\_going,pu} \right) \quad (4.3.1)$$

Under the approximation: for small value of θ, value of e_c is equal to the flat top value E, (4.3.1) reduces to (4.3.2) for phase commutation at θ_e=0.

$$\tau_{m,pu} = -i_{b,pu}\,; \quad \forall \theta_e \in \left(0, \frac{\pi}{3}\right) \quad (4.3.1)$$

i.e. motor torque is equal to the opposite of the non-commutating current. Similar torque equations can be derived for the other intervals along the supply period. Torque behavior in the two speed zones is exemplified in the graphs of *Figure 4.2.4*.

If Δi_b is the ripple in the non-commutating current i_b then i_b can be expressed as

$$i_{b,pu}(\theta) = -1 + \Delta i_{b,pu}(\theta) \quad (4.3.2)$$

Average value of the motor torque calculated over a supply period is given by

$$T_{pu} = 1 - \frac{3}{\pi} \int_0^{\theta_f} \Delta i_{b,pu}(\theta) d\theta \quad (4.3.3)$$

Because of the triangular behavior of i_b during the commutation interval, (4.3.3) can be rewritten as

$$T_{pu} = 1 - \frac{3\theta_f}{2\pi} \Delta i_{b,pu}(\theta_m) \quad (4.3.4)$$

From (4.3.1) torque ripple is defined as the peak-to-peak excursion and is equal to the magnitude of current excursion.

$$\Re T = \left| \Delta i_{b,pu}(\theta_m) \right| \quad (4.3.5)$$

where θ_m is equal to θ_r for $\Omega<\Omega_b/2$ and to θ_v for $\Omega>\Omega_b/2$.

4.4 Torque vs speed characteristics

4.4.1 Torque characteristics for $\Omega_{pu}<0.5$

In the low-speed zone, i_a reaches the reference value I_R before i_c vanishes. The rising interval θ_r of i_a is given by the first of (4.2.5); its maximum value is Θ_m and is taken for Ω_{pu}=0.5. This proves that the approximation $e_c \cong E$ is well grounded for $\theta_e<\theta_r$. The amplitude of i_c at θ_r is

$$i_{c,pu}(\theta_r) = 1 - \frac{1+\Omega_{pu}}{2-\Omega_{pu}} \qquad (4.4.1)$$

Along θ_r, the current regulator keeps T_1 ON until the current reaches I_R and i_d is equal to i_a. For $\theta_e > \theta_r$, T_1 is chopped. Taking into account that i) the feedback current is i_d and ii) i_d coincides with i_a when T_1 is ON, the control scheme must operate in a discrete way and sample i_d during the ON time of T_1 to regulate i_a at I_R. Due to the chopping of T_1, VSI does not more apply the source voltage V across the motor phases but δV. Then the term V in (4.2.4) must be substituted for by δV. For the second part of commutation rate of variation of i_c is given by

$$-2L\frac{di_c}{dt} = 2E; \quad \forall \theta \in (\theta_r, \theta_f) \qquad (4.4.2)$$

By (4.4.1) and (4.4.2), the expression of i_c in the second part of the commutation interval is

$$i_{c,pu}(\theta) = -\frac{1}{2\Theta_m}(\theta - \theta_r) + i_{c,pu}(\theta_r); \quad \forall \theta \in (\theta_r, \theta_f) \qquad (4.4.3)$$

Current i_c vanishes for

$$\theta_f - \theta_r = 2\frac{1-2\Omega_{pu}}{2-\Omega_{pu}}\Theta_m \qquad (4.4.4)$$

By substituting the first equation of (4.2.5) in (4.4.3), it turns out that the commutation interval is equal to

$$\theta_f = \Theta_m \qquad (4.4.4)$$

(4.4.4) shows that, in the low-speed zone, θ_f is depending only on motor data through the motor-distinctive parameter Θ_m whilst it is independent of the speed. Moreover, (4.4.4) proves that the approximation $e_c \cong E$ also used (4.3.1) is well grounded.

From (4.2.4), (4.3.2) and (4.4.1), the amplitude of $\Delta i_{b,pu}$ at θ_r is calculated in

$$\Delta i_{b,pu}(\theta_r) = -\frac{1-2\Omega_{pu}}{2-\Omega_{pu}} \qquad (4.4.5)$$

By substituting (4.4.4) and (4.4.5) in (4.3.5) and (4.3.4), the motor torque and the torque ripple are formulated as a function of the speed for a PM BLDC drive operating in the low-speed zone. They are expressed as

$$T_{pu} = 1 + \frac{3\Theta_m}{2\pi}\frac{1-2\Omega_{pu}}{2-\Omega_{pu}} \qquad (4.4.6)$$

$$\Re T = \frac{1-2\Omega_{pu}}{2-\Omega_{pu}} \qquad (4.4.7)$$

(4.4.6) shows that the motor torque exceeds the requested value of a quantity that is maximum as the speed approaches zero and reduces as the speed increases, becoming zero at $\Omega = \Omega_b/2$. Eq. (4.4.7) shows that the torque ripple has the same profile vs. the speed as

the excess of the motor torque. (4.4.6) and (4.4.7) do not apply at zero speed, i.e. at standstill, where the motor develops a torque exactly equal to its rated value and the torque ripple due to the commutations disappears.

4.4.2 Torque characteristics for Ωpu>0.5

In the high-speed zone, i_c vanishes before i_a reaches to I_R. The vanishing interval θ_v of i_c is given by the (4.2.5); its maximum value is 1.5 Θ_m and is taken for Ω_{pu}=1. This proves that the approximation $e_c \cong E$ used to derive (4.2.3) is well grounded for $\theta_e < \theta_v$. As a consequence, the approximation is also well grounded when used in deriving (4.3.1). Value of i_a at θ_v is

$$i_{a,pu}(\theta_v) = \frac{2-\Omega_{pu}}{1+\Omega_{pu}} \qquad (4.4.8)$$

Along θ_v, i_d is equal to i_a. For $\theta_e > \theta_v$, T1 is kept ON since i_a is still less than I_R, and i_d remains equal to i_a. As phase-c is now no more conducting, so rate of variation of i_a can be obtained from the voltage equation for the mesh formed by phase-a and phase-b.

$$2L\frac{di_a}{dt} = V - 2E; \quad \forall \theta \in (\theta_v, \theta_f) \qquad (4.4.9)$$

By (4.4.8) and (4.4.9), the expression of i_a in the second part of the commutation interval is

$$i_{a,pu}(\theta_e) = \frac{1}{2\Theta_m}\frac{1-\Omega_{pu}}{\Omega_{pu}}(\theta_e - \theta_v) + i_{a,pu}(\theta_v); \quad \forall \theta \in (\theta_v, \theta_f) \qquad (4.4.10)$$

Current i_a reaches to I_R for

$$\theta_f - \theta_v = 2\Theta_m \frac{\Omega_{pu}}{1-\Omega_{pu}}\left[1 - i_{a,pu}(\theta_v)\right] \qquad (4.4.11)$$

from (4.2.5) and (4.4.11), the commutation interval is

$$\theta_f = \Theta_m \frac{\Omega_{pu}}{1-\Omega_{pu}} \qquad (4.4.12)$$

Expression (4.4.12) shows that, different from the low-speed zone, in the high-speed zone θ_f depends upon both the motor-distinctive quantity Θ_m and the motor speed. As Ω_{pu} approaches 1, (4.4.12) is no more applicable, since the drive operates under voltage limitation.

To calculate the motor torque and the torque ripple in the high-speed zone it is necessary to determine $\Delta i_{b,pu}$ at θ_v. From (4.2.4), (4.3.2) and (4.4.8), we get

$$\Delta i_{b,pu}(\theta_r) = \frac{2\Omega_{pu}-1}{1+\Omega_{pu}} \qquad (4.4.13)$$

On substituting (4.4.13) in (4.3.3) and (4.3.4), we get

$$T_{pu} = 1 - \frac{3\Theta_m}{2\pi}\frac{(2\Omega_{pu}-1)\Omega_{pu}}{1-\Omega_{pu}^2} \qquad (4.4.14)$$

$$\Re T = \frac{2\Omega_{pu} - 1}{1 + \Omega_{pu}} \qquad (4.4.15)$$

Expression (4.4.13) and (4.4.14) formulate the torque characteristics of a PM BLDC drive in the high-speed zone. (4.4.14) explains that the motor torque drops below the requested value of a quantity that is zero for Ω_{pu}=0.5 and increases to a maximum as the speed approaches the no-load speed. (4.4.15) explains that the torque ripple has a similar profile vs. the speed as the drop of the motor torque.

4.5 Nominal speed and torque values

Nominal speed Ω_N is defined as the maximum speed at which the source voltage is able to bring the incoming phase current to the rated value of current I_R, at maximum by the end of the sixty-degree of supply interval of phase-a and phase-b, i.e. at $\pi/3$ where the successive current commutation starts. Under this situation, θ_f coincides with $\pi/3$. Thus on substituting $\theta_f = \pi/3$ in (4.4.12), nominal value of motor speed is given by,

$$\Omega_{N,pu} = \frac{1}{1 + \frac{3\Theta_m}{\pi}} \qquad (4.5.1)$$

Equation (4.5.1) states that Ω_N is less than the rated speed. From (4.4.14) to (4.5.1), nominal vlaues of the motor torque and corresponding torque ripple are given by (4.5.2) and (4.6.1) respectively.

$$T_{N,pu} = 1 - \frac{1}{2}\left(\frac{1 - \frac{3\Theta_m}{\pi}}{2 + \frac{3\Theta_m}{\pi}}\right) \qquad (4.5.1)$$

$$\Re T = \frac{1 - \frac{3\Theta_m}{\pi}}{2 + \frac{3\Theta_m}{\pi}} \qquad (4.5.2)$$

4.6 Case study

An inwheel suface mounted PM BLDC motor drive used in a city electric scooter is considered as a case of study for the present analytical study. Data of the motor are enlisted in *Table 4.6.1*. Experimental setup for the cross verification of analytical study is shown in *Figure 4.6.1*. Calculated values of motor-distinctive quantity Θ_m and nominal speed Ω_N are 47mrad and 0.96pu respectively.

Figure 4.6.2 plots the rising interval θ_r of i_a and the commutation interval θ_f in the low-speed zone, and the vanishing interval θ_v of i_c and again the commutation interval θ_f in the high-speed zone. The graphs point out that that i) the commutation interval is constant and equal to Θ_m in the low-speed zone whilst it increases notably in the high-speed zone, reaching the value of $\pi/3$ at the nominal speed, ii) in the low-speed zone the rising interval increases from zero to commutation interval Θ_m at Ω_{pu}=0.5, and iii) in the high-speed zone the vanishing interval starts from the value of Θ_m at Ω_{pu}=0.5 and then increases little by little up to 69 mrad at the nominal speed; the corresponding value of e_c is about 0.87 times

E, meaning is that certain mismatch exists in the upper part of the high-speed zone regarding the approximation $e_c \cong E$ made in deriving (4.2.3) and (4.3.1).

Tab. 4.6.1. PM BLDC motor data		
Data	Symbol	Value
Rated motor voltage	V_R	48 V
Rated motor current	I_R	50 A
Rated torque	T_R	32 Nm
Pole pairs	n_p	8
Phase resistance	R	50 mΩ
Inclusive phase inductance	L	75μH
Motor constant	k	0.32 V·s/rad

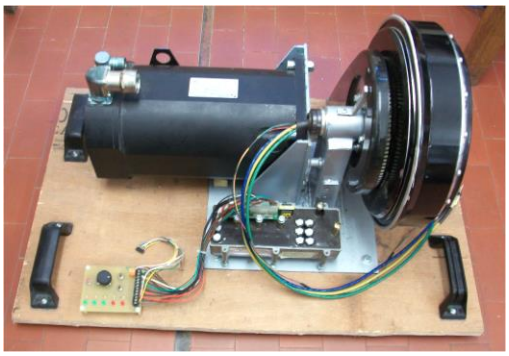

Fig. 4.6.1 Experimental setup

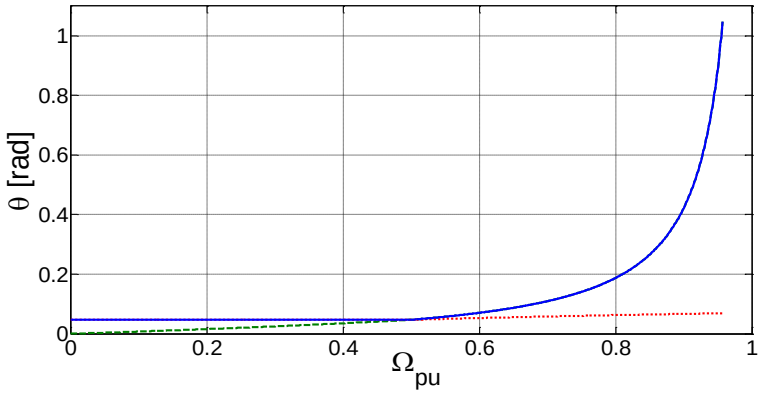

Fig. 4.6.2. Commutation interval (blue solid line), rising interval of i_a in the low-speed zone (green dashed line) and vanishing interval of i_c in the high-speed zone (red dotted line).

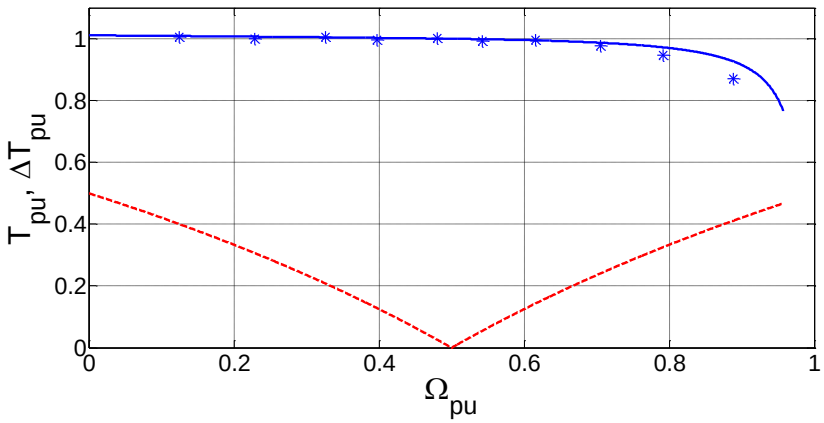

Fig. 4.6.3. Per-unit motor torque: analytical (blue solid line), experimental (blue star dots) and torque ripple (red dotted line).

The motor torque and the torque ripple are plotted in *Figure 4.6.3* with the blue solid line

and the red dotted line, respectively. The graphs show that i) the motor torque continuously drops with the increase in speed and falls by 23% of the rated value at the nominal speed, ii) the torque ripple has a symmetrical profile with respect to Ω_{pu}=0.5, as it can easily deduced by inspecting (4.4.15) and (4.4.7), and is as high as 50% both at low speeds and at high speeds.

To validate the theoretical findings, the study case consisting of an in-wheel PM BLDC motor fed by a dc-link current-controlled VSI has been considered and the experimental set-up of *Figure 4.6.1* has been arranged. The PM BLDC motor, which is visualized on the right hand side of *Figure 4.6.1*, has been coupled to a brake motor, which is visualized on the upper side of *Figure 4.6.1*. The brake motor, together with its drive, is in charge of developing the load torque. For testing purposes, a closed-loop control of speed has been built up around the PM BLDC drive. For a given speed, the motor torque has been measured by increasing the torque of the braking motor until the speed regulator of the PM BLDC drive outputs a current request equal to I_R and by detecting the corresponding torque developed by the braking motor. This test has been repeated for different speeds up to the nominal one to span the torque characteristic. To account for the phase resistances, it has been assumed that i) the effective voltage source is given by V minus the drop on the resistances of two conducting phases, and ii) the relevant phase currents are equal to I_R all along the conduction interval. The resulting speed value, given by

$$\Omega = \frac{V - 2RI_R}{2k} \qquad (4.6.1)$$

is equated to the base speed of the motor. Under these assumptions, the measured torque-speed values, denoted by stars, are reported in *Figure 4.6.3*. They are in good agreement with the theoretical findings, apart from at higher speeds where the transition interval of the vanishing current is comparable and the approximation of constant back emf assumed for the phase of the vanishing current starts to be rough.

4.7 Conclusion

An analytical study of the torque characteristics of a PM BLDC drive with DC-side current control has been performed, stressing the effects of the commutations on motor torque and torque ripple. The study has divided the speed range into two zones each of them having a proper behaviour of the phase currents during the commutations. The calculated motor torque exhibits a continuous drop with the speed whilst the calculated torque ripple is high both at low and high speeds, becoming zero just at half the speed range. The theoretical results on the motor torque have been supported by experimental tests executed on a commercial in-wheel PM BLDC drive.

4.8 References

[1] R.Carlson, M. Lajoie-Mazenc and J.C. dos S.Fagundes, “Analysis of Torque Ripple Due to Phase Commutation in Brushless DC Machine”, *IEEE Transaction on Industrial Applications*, vol. 28, no. 3, pp. 632-638, May/June 1992.

[2] M. Bertoluzzo, G. Buja, R. Keshri, “Brushless DC Drive Operation during Phase Commutation under Various Switching Patterns”, The 7th IEEE International Symposium on Diagnostics for Electric Machines, Power Electronics and Drives, 2009, SEDEMPED '09, pp 1-7, August 31-September 3,2009.

[3] R. Keshri, M. Bertoluzzo, A. Kumar, P. Thakura and G. Buja, “Generation of Possible Switching Patterns for VSI Using Micro-controller for the Control of PM BLDC Motor”, Proceedings of the Indian International Conference on Power Electronics, 2010, January 28-30, 2011, New Delhi, India.

[4] M. Bertoluzzo, G. Buja, R.K. Keshri and R. Manis, “Analytical Study of Torque vs. Speed Characteristics of PM Brushless DC Drives”, Proceedings of IECON 2012, pp. 1684-1689, October 25-28, 2012, Montreal Canada.

Chapter 5

Sinusoidal Phase Current Supply for PM BLDC Motor

Summary: PM BLDC motor fed by square-wave phase current (SqPC) suffers the problem of torque ripple causing drop in average motor torque with the increase in speed. Such a problem limits the utilisation of the motor up till the nominal speed and affects the life of the on board dc-source. Due to phase inductance outgoing current does not vanish instantly rather it starts freewheeling through the body diode of the another switch of the same phase and non-commutating phase switch. This changes the state of VSI from conduction of two phases to conduction of three phases causing a short of imbalance in circuital conditions. Under the consideration of same copper losses in stator winding injection of sinusoidal phase current (SPC) results in higher power and motor torque in constant torque zone. Although, phase commutation is present in this case, but the state of inverter remains same with the conduction of all the three phases before, during and after the phase commutation. Thus it is possible to achieve an average torque that remains independent of rotor position and limited by the magnitude of back-emf. In this case torque ripple remains constant in contrary with SqPC, where it increases with speed. Thus use of SPC in coordination with SqPC can result in overall improvement in speed vs torque behaviour of the motor.
Present chapter discusses the torque behaviour of the PM BLDC motor in terms of torque ripple and average torque in the case SPC supply. Discussion is further extended for the control issues of PM BLDC motor for SPC supply. Discussion is supported by the simulation and experimental results.

5.1 Torque-speed characteristic for the sinusoidal phase current supply

From the discussion on SqPC supply for PM BLDC motor it is clear that, motor suffers with the problem torque ripple due to phase commutation. Magnitudes of the torque ripples continue to increase with the increase in speed and can be 50-60% at higher speed. Dropping torque speed characteristics limits its application up till the end of constant torque zone. As it is observed that problem of ripple associated with commutation is due to the non-uniformity in the in the state of inverter due to phase inductances, i.e. during regular interval two phases of the inverter operate whereas during commutation all the three phases comes into action. In case of sinusoidal phase current (SPC) supply, inverter state before, during and after the phase commutation remains same and result in smooth and balanced phase commutations. SPC is achieved by properly modulating the voltage applied to the phases in order to maintain the corresponding phase current as sinusoidal one. To maximize the torque, phase currents are kept in phase with the phase back-emf. SPC supply for PM BLDC motor in constant torque zone is an un-traditional approach. Therefore speed torque characteristic of the motor is analysed.

Figure 5.1.1 shows the phase currents and corresponding phase back-emf waveforms for a PM BLDC motor drive fed by SPC.

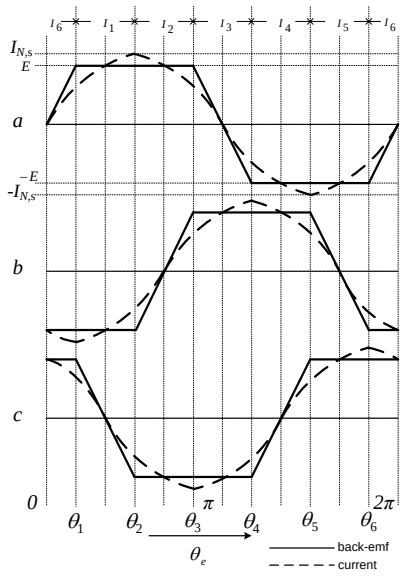

Fig.5.1.1 Sinusoidal phase currents and back-emf of PM BLDC motor drive.

In order to limit the cu-losses for the two cases of supply, rms value for SPC and SqPC must be same i.e $I_{rms,s}=I_{rms,sq}$. 'sq' is used to represent square-wave 's' is used to represent sinusoidal. With the consideration that there is no ripple in the quasi square phase current, if I_N is the nominal current, then the corresponding peak value of the sinusoidal phase current $I_{N,s}$ is given

$$I_{N,s} = \frac{2}{\sqrt{3}} I_N \qquad (5.1.1)$$

Phase-a current i_a in terms of rotor position θ_e is equal to $I_{N,s} \sin(\theta_e)$. Phase-b and phase-c currents are displaced from i_a by $-2\pi/3$ and $2\pi/3$ radians. Back-emf for phase-a is expressed as

$$e_a(t) = \begin{cases} \frac{6}{\pi}\theta_e E & \theta_e \in \left[0, \frac{\pi}{6}\right) \\ E & \theta_e \in \left[\frac{\pi}{6}, \frac{5\pi}{6}\right) \\ \left[1 - \frac{6}{\pi}\left(\theta_e - \frac{5\pi}{6}\right)\right] E & \theta_e \in \left[\frac{5\pi}{6}, \frac{7\pi}{6}\right) \\ -E & \theta_e \in \left[\frac{7\pi}{6}, \frac{11\pi}{6}\right) \\ -\left[1 - \frac{6}{\pi}\left(\theta_e - \frac{11\pi}{6}\right)\right] E & \theta_e \in \left[\frac{11\pi}{6}, 2\pi\right) \end{cases} \qquad (5.1.2)$$

Fourier series representation of e_a in terms of rotor position is given by (5.1.3). For phase-b and phase-c, θ_e is replaced by $\theta_e - 2\pi/3$ and $\theta_e + 2\pi/3$.

$$e_a(\theta_e) = \frac{24E}{\pi^2} \sum_{n=1,2,3.....} \frac{(-1)^{\frac{n-1}{2}} \cos\left(\frac{n\pi}{3}\right)}{n^2} \sin n\theta_e \qquad (5.1.3)$$

Table 5.1.1. Percentage of harmonic components in trapezoidal back-emf		
Harmonic order	$e_{a,peak}$(n)/E	Normalized in (%)
1	1.2158	100.00
3	0.2708	22.27
5	0.0446	3.67
7	-0.0248	2.03
9	-0.0300	2.46
11	-0.0100	0.82
13	0.0072	0.59
15	0.0100	0.82
17	0.0042	0.35

Percentage contributions of odd harmonic components of trapezoidal back-emf are shown in *Table 5.1.1*. From the table it is clear that only first and fundamental components are dominant in nature and the effect of other components can be neglected. As the fundamental component of the back-emf is responsible for the production of necessary electrical power and so torque, power can be expressed in terms of fundamental component of back-emf and is given by

$$P_s = \frac{3}{2} I_{N,s} e_{a1} \qquad (5.1.4)$$

where e_{a1} is the fundamental component of e_a and is equal to $12E/\pi^2$. On substituting the values in (5.1.4), electrical power is given by

$$P_s = \frac{12\sqrt{3}}{\pi^2} E I_{N,sq} \approx 1.053 P_{sq} \qquad (5.1.5)$$

where P_{qs} is the electrical power with SqPC supply and is equal to $2EI_N$. From (5.1.5) it can be concluded that in case of SPC it is possible to obtain approximately 5% higher power and hence torque as compared to SqPC fed PM BLDC motor. Corresponding expression for nominal torque is given by

$$T_{N,s} = \frac{P_s}{\Omega_m} = \frac{6\sqrt{3}}{\pi^2} (2kI_{N,sq}) \approx 1.053 T_{N,sq} \qquad (5.1.6)$$

5.1.1 Torque ripple vs speed for the sinusoidal supply

Instantaneous torque of the motor in terms of fundamental component of the back-emf is expressed by (5.1.7)

$$\tau_m = \frac{1}{\Omega_m} \left[e_a i_a + e_b i_b + e_c i_c \right] \qquad (5.1.7)$$

where ω_m is the motor speed in rad/sec. for the fundamental components of back-emf, instantaneous torque (5.1.7) is re-written as

$$\tau_{m1} = \frac{12kI_{N,s}}{\pi^2}\left[\sin^2\theta_e + \sin^2\left(\theta_e - \frac{2\pi}{3}\right) + \sin^2\left(\theta_e + \frac{2\pi}{3}\right)\right] \qquad (5.1.8)$$

where τ_{m1} is the motor torque due to fundamental components of the back-emf.

Expression within the bracket of (5.1.8) have constant value equal to 1.5 for all the values of θ_e and results in constant value of torque $\tau_{m,avg} = \tau_{m1} = 18kI_{N,s}/\pi^2$ and is equal to (5.1.6). This validates the consideration of fundamental component of back emf to calculate average value of torque and motor power. Thus (5.1.8) gives the average value of torque.

Instantaneous value of the motor torque is calculated by considering expression of trapezoidal back-emf as a function of θ_e in (5.1.7). Variation in instantaneous torque and average torque with rotor position is shown in *Figure 5.1.2*. Instantaneous motor torque $\tau_6$for the region $\theta_e \epsilon [0, \pi/6)$ is given by (5.1.9).

$$\tau_6 = kI_p\left(\frac{6}{\pi}\theta_e \sin\theta_e + \sqrt{3}\cos\theta_e\right) \qquad (5.1.9)$$

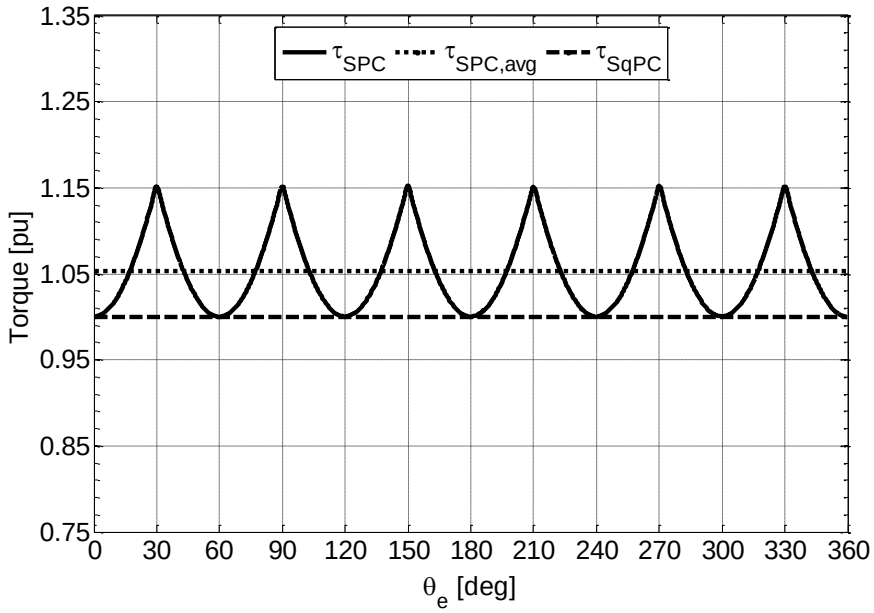

Fig. 5.1.2 variation in average and instantaneous value of motor torque

Torque ripple of the motor is given by the (5.1.10).

$$\Delta\tau = \tau_6\left(\frac{\pi}{6}\right) - \tau_6(0) = (2-\sqrt{3})kI_{N,s} = \left(\frac{2-\sqrt{3}}{\sqrt{3}}\right)(2kI_{N,sq}) \approx 0.1547T_{N,sq} \qquad (5.1.10)$$

Thus the motor torque ripple in case of SPC remains constant and is equal to approxemately15% of the nominal motor torque.

From the study of SqPC and SPC supply it is observed that although SqPC provide a flat torque characteristic, problem of torque ripple during phase commutation results in dropping speed torque characteristic. Magnitude of the torque ripples increases with speed and go up to 50-60% of the rated torque before the motor fails to build up the necessary

electrical torque. In contrary SPC supply result in pulsating torque with a ripple of approximately 15%. Both the average torque (5.1.8) and torque ripple (5.1.10) in case of SPC supply are independent of motor speed. Therefore overall torque behaviour of the PMBL DC motor in constant torque zone can be improved with the conditional utilisation of SPC supply together with SqPC supply. Condition for the utilisation can be the shift to SPC from SqPC when the torque ripple goes beyond 15% of the rated torque with the preset motor speed. This approach can result in the extension of constant torque zone of the motor. From the table (5.1.1) it is clear that the effect of third harmonic component of trapezoidal back-emf cannot be neglected. Consideration of third harmonic component for the analysis results in 12% of torque ripple. As the difference is not big, for the sake of simplification only fundamental component of back-emf is considered.

5.1.2 Base speed in case of SPC supply

For the SPC supply, the base speed $\Omega_{s,B}$ of the motor is defined as the maximum speed at which VSI is able to inject SPC of nominal magnitude into the motor. $\Omega_{s,B}$ depends on the maximum output voltage of the VSI.

Line-to-line voltage v_{ab} of the motor is expressed as

$$v_{ab} = L\frac{d}{dt}(i_a - i_b) + e_{ab} \qquad (5.1.11)$$

First term on the right hand side of (5.1.11) is inductive voltage drop $v_{L,ab}$ and e_{ab} (= e_a - e_b) is the line back-emf. $v_{L,ab}$ and e_{ab} as a function of rotor position θ_e are expressed by (5.1.12).

$$v_{L,ab} = \sqrt{3}n_p\Omega LI_{N,s}\cos\left(\theta_e + \frac{\pi}{6}\right); \quad e_{ab}\big|_{\theta_e \in [0,\pi/6]} = E\left(1 + \frac{6}{\pi}\theta_e\right) \qquad (5.1.12)$$

$v_{L,ab}$ has cosine variation and continues to decrease in the interval $\theta_e \epsilon [-\pi/6, \pi/6]$ where as e_{ab} increases with θ_e up till $\theta_e = \pi/6$ where e_{ab} becomes equal to $2E$. Thus overall increase in v_{ab} is observed. As from $\theta_e = \pi/6$, e_{ab} becomes constant and $v_{L,ab}$ continues to decrease in v_{ab} is observed. Therefore it can be concluded that at $\theta_e = \pi/6$, v_{ab} reaches to its peak value. Variations in line voltages v_{ab}, $v_{L,ab}$ and e_{ab} with θe are shown in *Figure 5.1.3*.

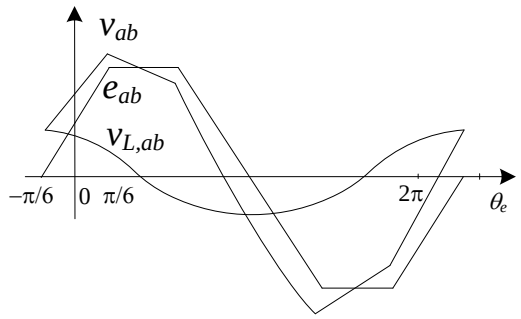

Fig. 5.1.3 Line voltages

Condition for v_{ab} to reach its peak value is confirmed by the condition of increasing function with respect to θ_e for (5.1.11) in the interval $\theta_e \epsilon [-\pi/6, \pi/6]$ i.e.

$$\frac{dv_{ab}}{d\theta_e} > 0 \Rightarrow \sin\left(\theta_e + \frac{\pi}{6}\right) < \frac{2\sqrt{3}E}{\pi n_p \Omega L I_{N,s}} \qquad (5.1.13)$$

(5.1.13) further simplifies to the condition (5.1.14).

$$\frac{2\sqrt{3}k}{\pi n_p L I_{N,s}} > 1 \Rightarrow 1.05\Theta_m < 1 \qquad (5.1.14)$$

(5.1.14) is true for a PM BLDC drive, as motor specific quantity Θ_m is very small compared to one and confirms the behaviour of v_{ab} to reach its peak value at $\theta_e = \pi/6$. Further (5.1.14) can be rearranged as

$$E_N > \frac{\pi}{2\sqrt{3}} V_{L,N} \qquad (5.1.15)$$

where $V_{L,N}$ is equal to $n_p \Omega_N L I_{N,s}$. Thus the inequality (5.1.15) is satisfied by an ordinary PM BLDC drive, where under nominal condition conditions, back-emf is much larger than the voltage drop across the phase inductance. From (5.1.11) and (5.1.12) for speed Ω, Ω peak value of v_{ab} is equal to

$$V_{ab} = \frac{\sqrt{3}}{2} n_p \Omega L I_{N,s} + 2k\Omega \qquad (5.1.16)$$

As the maximum line-to-line voltage generated by the VSI in linear modulation zone is equal to V_N. Thus by substituting $V_{ab} = V_N$ and $\Omega = \Omega_{B,s}$ in (5.1.16) with the approximation $V_N \approx 2E_N$ for negligible voltage drop across phase resistance, (5.1.16) results in the expression for base speed of PM BLDC drive for SPC supply and is equal to

$$\Omega_{B,s,pu} = \frac{1}{1 + \Theta_m} \qquad (5.1.17)$$

Beyond the base speed, motor operates under the voltage limitation. For the speed range beyond $\Omega_{B,s}$ and up to Ω_o, magnitude of SPC must be reduced for the VSI to operate in linear modulation zone. Magnitude of the $I_{s,L}$ is derived from (5.1.16) and is equal to

$$I_{s,L} = \frac{2}{\sqrt{3}} \frac{V_N - 2k\Omega}{n_p \Omega L} \qquad (5.1.18)$$

From (5.1.8) and (5.1.18), corresponding value of motor torque and torque ripple are

$$T_{B,s,pu} = \frac{18}{\sqrt{3}\pi^2 \Theta_m} \left(\frac{1 - \Omega_{pu}}{\Omega_{pu}}\right) \cong \frac{1.05}{\Theta_m} \left(\frac{1 - \Omega_{pu}}{\Omega_{pu}}\right) \qquad (5.1.19)$$

$$TR_{B,s,pu} = \frac{2/\sqrt{3} - 1}{\Theta_m} \left(\frac{1 - \Omega_{pu}}{\Omega_{pu}}\right) \cong \frac{0.155}{\Theta_m} \left(\frac{1 - \Omega_{pu}}{\Omega_{pu}}\right) \qquad (5.1.20)$$

From the analytical study of PM BLDC motor drive for SqPC supply as carried out in the previous chapter, base speed and the corresponding torque are summarized as

$$\Omega_{B,sq,pu} = \left(1 + \frac{3\Theta_m}{\pi}\right)^{-1} \qquad (5.1.21)$$

$$T_{B,sq,pu} = \frac{3}{2}\left(1+\frac{3\Theta_m}{\pi}\right)\left(2+\frac{3\Theta_m}{\pi}\right)^{-1} \qquad (5.1.21)$$

5.1.3 Convenience analysis of SPC over SqPC

The per-unit motor torque and torque ripple for SPC and SqPC supplies are plotted in *Figures 5.1.4* and *5.1.5*, respectively for the considered PM BLDC motor drive.

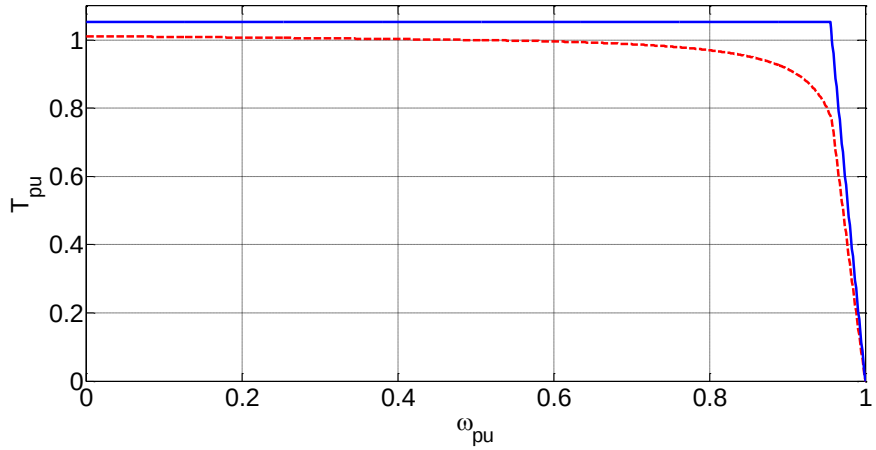

Fig. 5.1.4. Torque speed characteristics of PM BLDC motor drive with a) SPC supply (red dots) and b) SqPC supply (blue line)

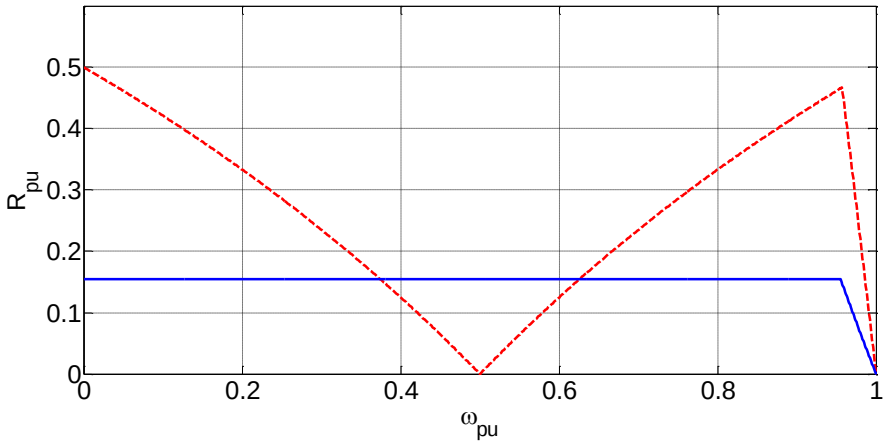

Fig. 5.1.5. Torque ripple vs speed characteristics of PM BLDC motor drive with a) SPC supply (red dots) and b) SqPC supply (blue line)

In both the figures, the red dashed lines refer to the SqPC supply whilst the blue solid lines refer to the SPC supply. A cross-examination of the graphs shows the better performance of the sinusoidal current supply both from the motor torque and torque ripple point of view. Indeed, besides the above-mentioned 5% higher value of the motor torque, the graphs in *Figure 5.1.4* together with the help of the data reported in *Table 5.1.2*, point out that i) the base speeds for both the types of current supply are almost equal, ii) the PM BLDC drive with SPC supply develops a constant torque up to the base speed while its SqPC supply counterpart develops a lower torque starting from about half the nominal speed to about

0.76 times at the base speed, and iii) above the nominal speed, the torque of the PM BLDC drive with SPC supply decreases linearly, approximately likely to that one of the SqPC supply counterpart but keeping a higher value. In turn, the graphs of *Figure 5.1.5* point out that the torque ripple in the case of SPC supply is much lower at both low and high speeds while it exceeds that one of the SqPC supply in a speed interval of about 0.22 pu centered at half of the nominal speed.

Table 5.1.2 PM BLDC motor drive quantities		
Data	Symbol	Value
	Θ_m	46.8 mrad
Base speed with sinusoidal current supply	$\Omega_{B,s,pu}$	0.955
Base speed with square-wave current supply	$\Omega_{B,s,pu}$	0.957
Torque at base speed with square-wave current supply	$T_{B,sq,pu}$	0.766

Numerical simulations have been executed to investigate the effect of the phase resistances on the torque performance of the PM BLDC drives with the two types of current supply. The simulations have demonstrated that the voltage drop across the resistances reduces the base speed of about 0.9 times the value reported in *Table 5.1.2* for the SPC supply and of about 0.89 for the SqPC. Therefore the results obtained above are not substantially modified by accounting for the motor resistances.

Theoretical findings have demonstrated that the torque performance obtained with SPC supply outperforms the SqPC supply in almost all over the speed range. The torque-speed characteristic is higher all along the speed range, especially nearly the base speed. The torque ripple is less almost all along the speed range, apart from a speed interval centered at half the nominal speed and about 22% the nominal speed long, where the torque ripple of a PM BLDC drive with SqPC reduces due to the nearly matching profile between the injected current and the removed current.

5.2 Control strategy for SqPC and SPC supply

Sinusoidal phase current supply for PM BLDC motor drive can be realized by the current control scheme. Conventional current control scheme for PM BLDC motor drive is shown in *Figure 5.2.1*.

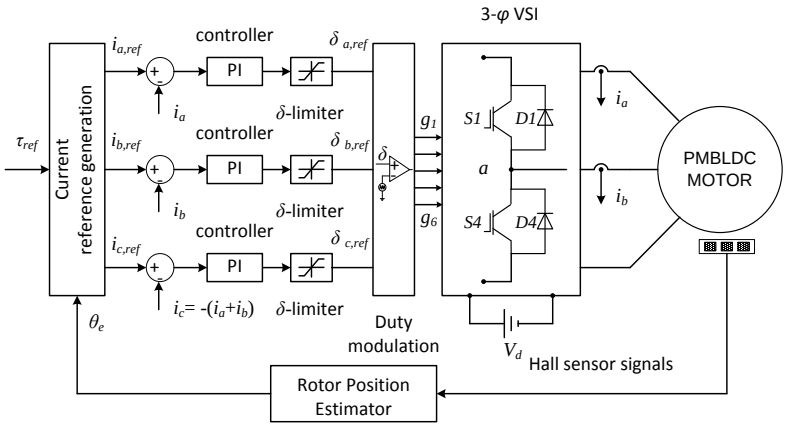

Fig.5.2.1. Conventional current control scheme for PM BLDC motor drive

In such a scheme as per the rotor position and torque reference current references for the

three phases are generated. Generated reference current is compared with the feed-back current from the motor. PI controllers to generate the references for the duty-ratios for the corresponding inverter legs. These reference duty-ratios are modulated with the carrier signal to generate driver signals g_1 *to* g_6 for the switches of the 3-φ VSI Generated duty ratio corresponds to the phase voltage to be applied to the motor to ensure the phase current as per the reference.

5.2.1 Estimation of speed, rotor position and generation reference current

Rotor position is estimated from the information of hall signals. Hall sensor gives a high value, when it remains in the vicinity of North Pole of the permanent magnet for 180° electrical angle duration and low value for next 180° duration when it comes in the vicinity of South Pole of the magnet. Hall sensors are displaced from each other by 120° electrical angle in positive negative direction.

Figure 5.2.2a and *5.2.2b* shows the back-emf and Hall sensor signals for the three phases with sinusoidal and square-wave current refrence simultaneously. Rotor position is estimated with respect to Hall-c and starting point of the measurment is considered from the instant where Hall-c fall down to zero as shown in *Figure 5.2.2*. Reason behind the consideration of hall-c and its falling to zero instant for the position measurement is, at this particular instant phase-a current can be expressed by *cosine* function of rotor position with peak at this particular instant as shown in figure.

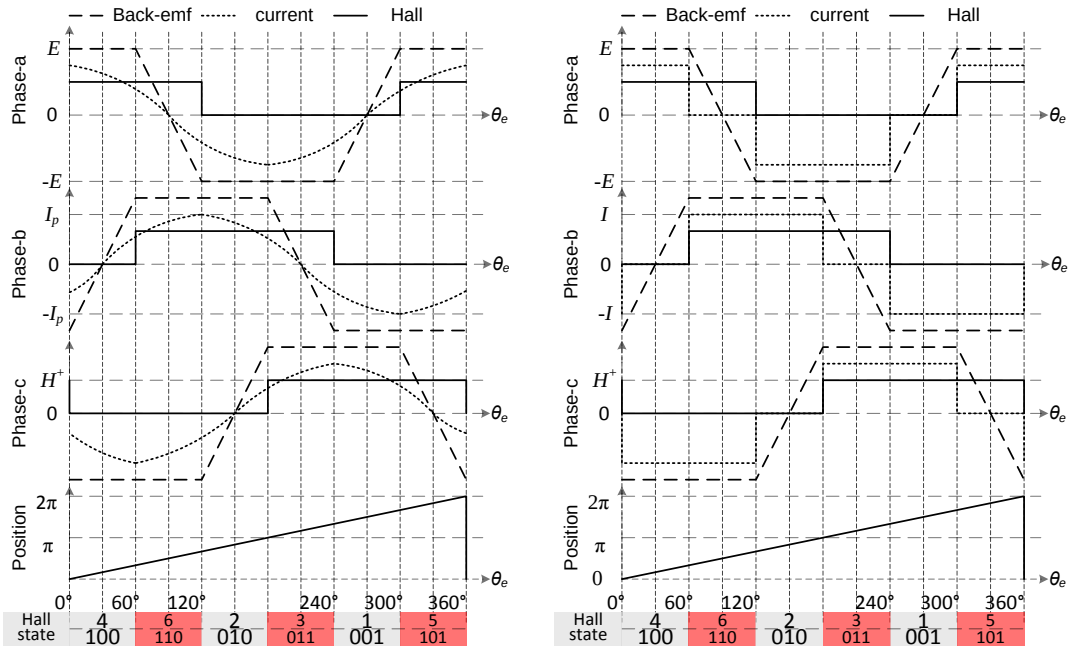

Fig.5.2.2 Phase back-emf, hall signal and rotor position with: a) sinusoidal phase current reference and b) square-wave phase current reference

Thus the refrence currents are written as

$$\left.\begin{aligned} i_a &= I_p \cos(\theta_e) \\ i_b &= I_p \cos(\theta_e - 2\pi/3) \\ i_c &= I_p \cos(\theta_e + 2\pi/3) \end{aligned}\right\} \qquad (5.2.1)$$

where $\theta_e=\Omega_e t$. ω_e is the motor electrical speed in rad/sec and is equal to $p\Omega_m$.

Speed of the motor Ω_e , can be calculated with two approaches:

- measurement of duration of each of the six hall states is considered
- measurement of duration of high or low state of individual hall sensors

In the first approach, if $\Delta t_{\text{hall\_sate}}$ is the duration of any of the hall state, then the estimated period T of the supply cycle will be equal to $6 \times \Delta t_{\text{hall\_sate}}$. Therefore the speed of the motor is estimated as

$$\Omega_e = \frac{2\pi}{T} = \frac{\pi}{3\,\Delta \text{t}_{\text{hall\_state}}} \qquad (5.2.2)$$

In this case speed is updated at the end of each of the six hall state i.e. with each 60° duration of supply cycle speed is updated. Up till the next speed update, previous value of speed is considered for the calculation of rotor position. Rotor position is calculated with the previous value of speed multiplied by the time laps from the start of falling edge of Hall-c.

In the second approach speed is updated with the falling edge of each of the hall sensor. If $\Delta t_{\text{hall\_high}}$ is the duration for which particular hall remains high, then the estimated period T of the supply cycle is equal to $2\times \Delta t_{\text{hall\_high}}$. Therefore the speed of the motor is estimated as

$$\omega_e = \frac{2\pi}{T} = \frac{\pi}{\Delta \text{t}_{\text{hall\_high}}} \qquad (5.2.3)$$

In this case speed update is available with the gap of 120° electrical angle duration. If Δt_{hall_c} is the time laps from the instant of falling edge of hall-c and $\omega_{\text{e,prev}}$, is the previous updated of motor electrical speed, then the position is estimated by the relation

$$\theta_e = \omega_{e,prev} \Delta t_{hall\_c} \qquad (5.2.4)$$

At the end of each falling edge of hall-c, Δt_{hall_c} is set to zero for the start of next cycle of position measurement from *0* to 2π as shown in *Figure 5.2.2*. Rotor position can also be extracted from the information of phase variables like phase currents and terminal voltages. This type of estimation is placed under sensor-less control of the PM BLDC motor. Present chapter consider only position estimation through hall sensor. With the information of position from (5.2.3) square-wave or sinusoidal phase current reference can be generated as listed in *Table 5.2.1*.

Table 5.2.1 Reference currents for SqPC and SPC supply

Hall state	Rotor position θ_e	SqPC			SPC		
		i_a	i_b	i_c	i_a	i_b	i_c
4	0-π/3	+*I*	0	-*I*	$I_P sin(\theta_e)$	$I_P sin(\theta_e-2\pi/3)$	$I_P sin(\theta_e+2\pi/3)$
6	π/3-2π/3	0	+*I*	-*I*			
2	2π/3-π	-*I*	+*I*	0			
3	3π/3-4π/3	-*I*	0	+*I*			
1	4π/3-5π/3	0	-*I*	+*I*			
5	5π/3-2π	+*I*	-*I*	0			

5.2.2 Calculation of controller parameters

Figure 5.2.3 shows the Block diagram representation of the transfer function model for phase current control scheme for SqPC supply.

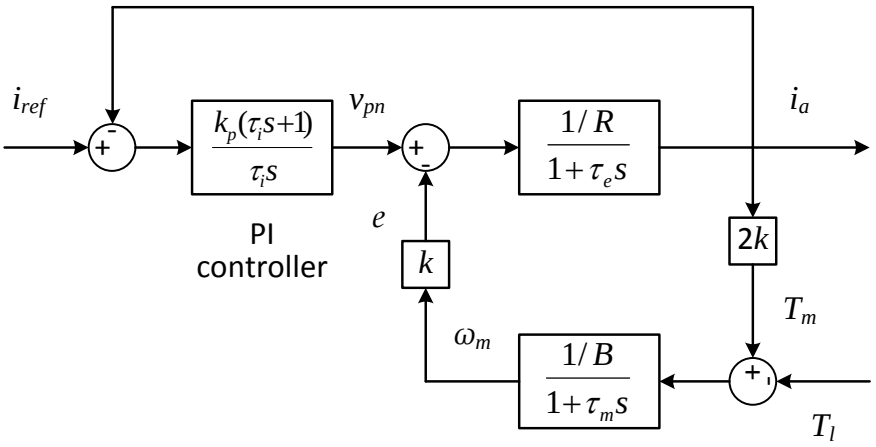

Fig.5.2.3 Block diagram representation of transfer function model of phase current control scheme.

where $\tau_e=L/R$ is electrical time constant, $\tau_m=J/B$ is mechanical time constant. J is combined moment of inertia of the motor and B is the coefficient of viscous friction, k_p and τ_i are the proportional gain and integral time constant of the PI controller.

As the speed mechanical dynamics is much slower than the current dynamics, for a supply interval, back-emf can be consider as a disturbance for the current loop. This assumption results in the closed loop transfer function for the phase current control, and is given by

$$\frac{I_a(s)}{I_{ref}(s)} = \frac{k_p(\tau_i s+1)/R}{\tau_e\tau_i s^2 + \tau_i\left(1+\frac{k_p}{R}\right)s + \frac{k_p}{R}} \qquad (5.2.5)$$

For a given damping ratio ζ and natural frequency ω_n (= $2\pi f_{band\_width}$), where f_{band_width} is the bandwidth of the current loop, controller parameter are given by

$$k_p = (2\zeta\omega_n\tau_e - 1)R; \quad \tau_i = \frac{k_p}{\tau_e\omega_n^2 R} \qquad (5.2.6)$$

For the motor used for experimentation with parameters R= *35m*Ω, L = *75μ*H (including mutual inductance), J = 0.1kg-m^2 and B=*0.5*N-m/rad/sec and control specification as ζ=0.7 and f_{band_width}= 700Hz, values of k_p and τ_i are 0.427 and 2.94×10^{-3}. For the purpose of simulation and experimentation parameters of PI controller were kept same for the case of SqPC supply and SPC current supply

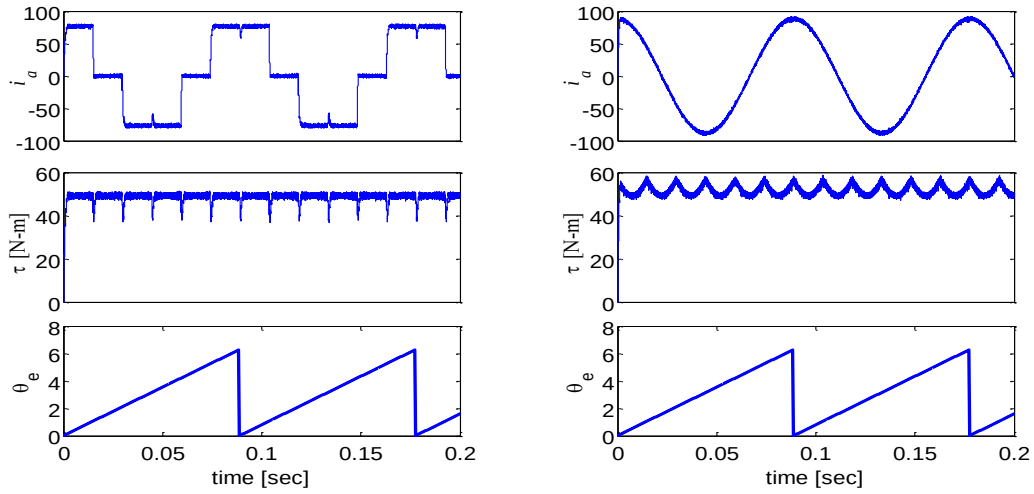

(a) (b)

Fig. 5.2.5 Phase current, torque and rotor position with: a) SqPC; b) SPC at motor mechanical speed equal to 70.74rad/sec.

Figure 5.2.5a and *5.2.5b* show the phase-a current, torque and rotor position with SqPC and SPC supply respectively, at motor mechanical speed equal to 70.74rad/sec.

As discussed in theoretical analysis and observed in simulation, motor suffers with the torque ripple of 26% in case of SqPC supply and 18% in case of SPC supply with around 5% higher average torque. Lesser torque ripples in case of SPC support the consideration of SPC during constant torque zone of the PM BLDC motor. Thus combined use of SqPC and SPC supply can be preferred for the improvement of overall torque behaviour of the motor in constant torque zone. Combined use of SqPC and SPC supplies are demonstrated in *Figures 5.2.6a* and *5.2.6b*

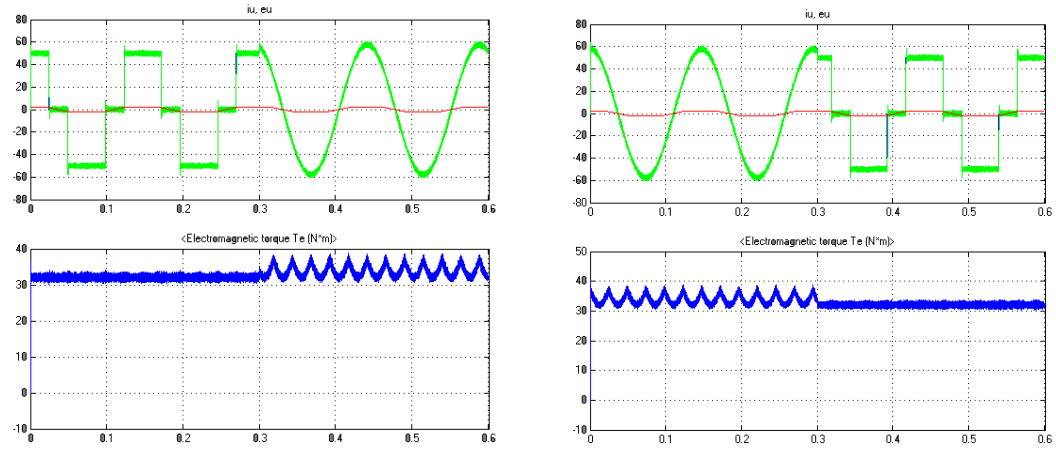

(a) (b)

Fig. 5.2.6 Phase-a current, back-emf, and torque with SqPC and SPC, shift from: a) SqPC supply to SPC supply; b) SPC supply to SqPC supply

5.3 Implementation of current control schemes

5.3.1 Implementation strategy

Figures 5.3.1a shows the PM BLDC as discussed earlier with two servomotors as load used for experimentation. *Figure 5.3.1b* shows the VSI together with DSP-interface circuits.

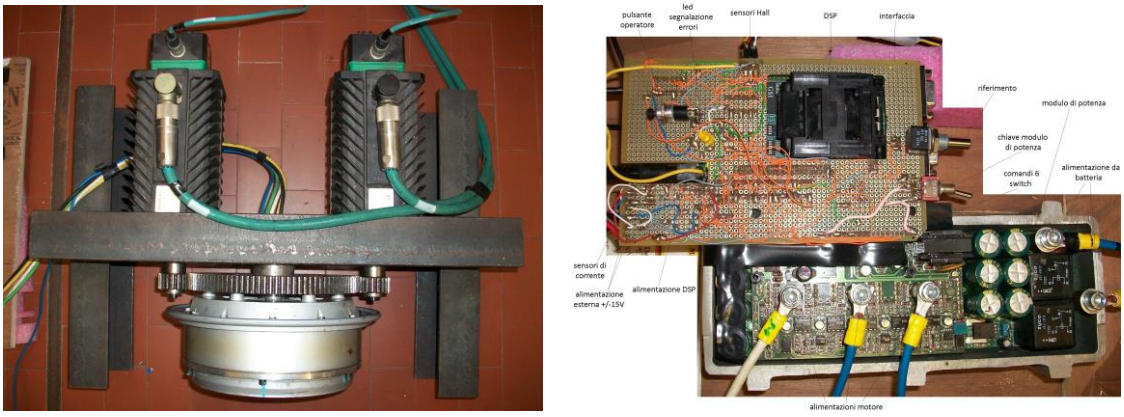

(a) (b)

Fig. 5.3.1 a) PM BLDC motor with two servomotors as load and b) VSI with DSP-interface circuits

Flow chart representation of main program, ADC subroutine and the scheme for discrete PI controller used in the PI_Update subroutine are shown in *Figures 5.3.2a – 5.3.2c*. In scheme of *Figure 5.3.2c*, T is sampling period, *Kp* is proportional gain and *Ki*. Frequency for the PWM moudlation is selected as 14*k*Hz. Therefore $T = 35.71\mu Sec$.

For the purpose of current refrence generation and transformation of circuit variables, calculation of cosine function is required. For this cosine series up to 9^{th} term is considered as this gives more accurate value. Since the computation of cosine is a quite costly in terms of time, therefore for the reduction in evaluation time, cosine table for 0 to 90° is pre-considered, and method of interpolation is used to evalueate cosine for a perticular rotor positon. Like wise limitiation of duty ratio on the circle also require computation of function *square_root*. This is also evaluated by the method of interpolation.

Cosine series used for the the computation is

$$\cos\theta_e = 1 + \sum_{i=1,2..9} (-1)^n \frac{\theta_e^{2n}}{(2n)!} \qquad (5.3.1)$$

code for the computation of cosine is given in *Table 5.3.1*.

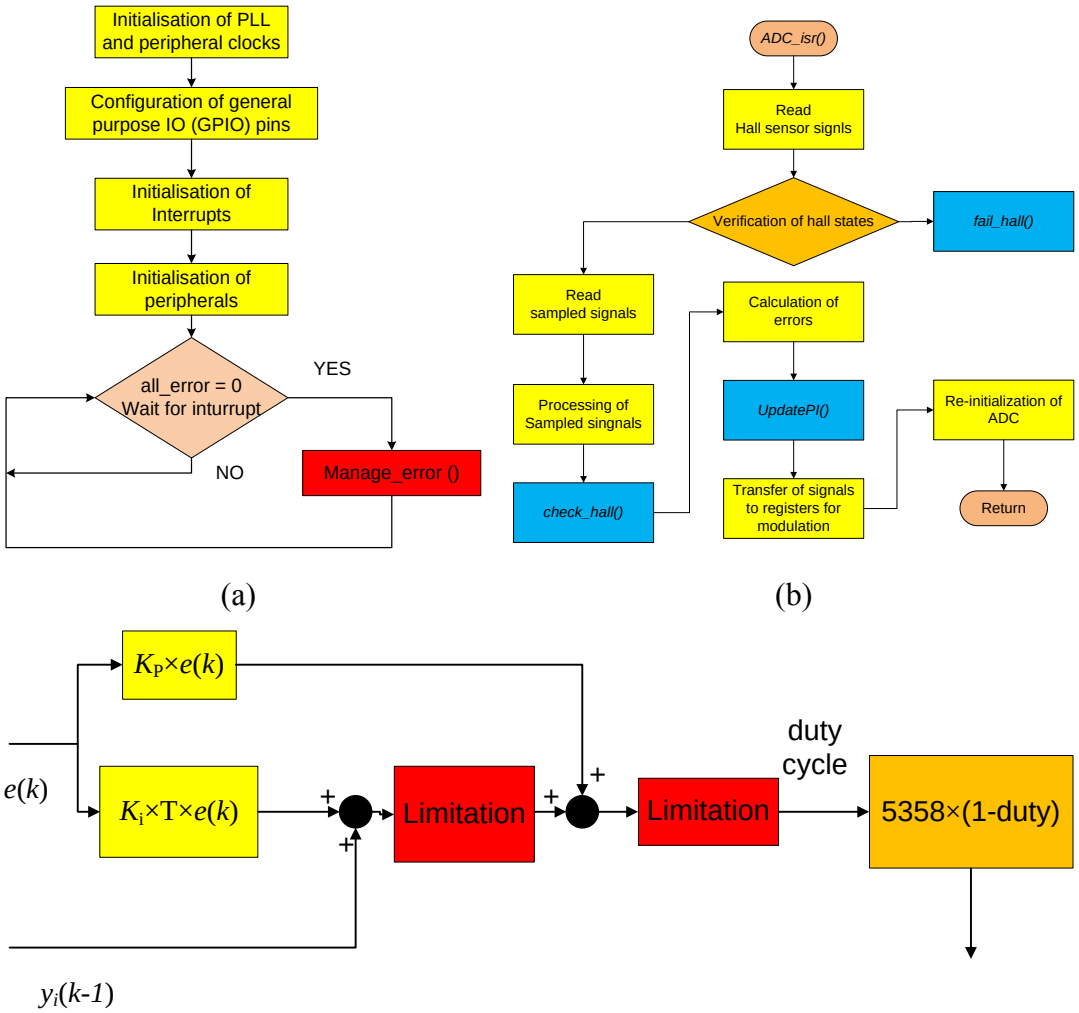

Fig. 5.3.2. Flow chart for: a) main program b) interrupt service subroutine for ADC, c) scheme for PI update.

For the measurment of speed time laps is calculated as per the counting of call of ADC subroutine. Counter selected for the measurment of speed is incremented by one with each call. Therefore Δt in (5.2.2) and (5.2.3) for the caluculation of speed is equal to number of counts of the the counter *count* multiplied by $2T$, i.e $\Delta t = 35.71 \times count$ μSec. Codes used for the computation of speed and position are placed in *Table 5.3.1*.

Table 5.3.1 Codes for the computation of cosine, speed and position

/*Computation of cosine with table*/

```
float cosine_table(float angle)
{
if (angle<0)
        angle += 360;
if (angle>360)
        angle -= 360;
angle_ip = angle;
        if(angle_ip>=0 && angle_ip<90)
cos = cos_table[angle_ip] + (angle- angle_ip)*(cos_table[angle_ip+1]-
cos_table[angle_ip]);
        if(angle_ip>=90 && angle_ip<180)
                {
                angle_ip = angle_ip - 90;
cos = -( cos_table[90-angle_ip] + (angle-90-angle_ip)*(cos_table[90-
angle_ip-1]-cos_table[90-angle_ip]));
                }
        if(angle_ip>=180 && angle_ip<270)
                {
angle_ip = angle_ip - 180;
cos = -( cos_table[angle_ip] + (angle-180-
angle_ip)*(cos_table[angle_ip+1]-cos_table[angle_ip]));
                }
        if(angle_ip>=270 && angle_ip<360)
                {
                angle_ip = angle_ip - 270;
cos = cos_table[90-angle_ip] + (angle-270-angle_ip)*(cos_table[90-
angle_ip-1]-cos_table[90-angle_ip]);
                }
return cos;

}
```

/* code for calculation of speed based on period of three Hall sensors*/

```
        if (hCBA.bit.hA == prevA)
                count_a++;
        else
                {
                deltat_1_A = 2*count_a*35.71e-6;
                speed1_A = 2*3.14159/deltat_1_A;
                count_a = 0;
                prevA = hCBA.bit.hA;
                }

        if (hCBA.bit.hB == prevB)
                count_b++;
        else
                {
                deltat_1_B = 2*count_b*35.71e-6;
                speed1_B = 2*3.14159/deltat_1_B;
                count_b = 0;
                prevB = hCBA.bit.hB;
                }

        if(hCBA.bit.hC == prevC)
                count_c++;
        else
                {
                deltat_1_C = 2*count_c*35.71e-6;
                speed1_C = 2.*3.14159/deltat_1_C;
                count_c = 0;
                prevC = hCBA.bit.hC;
                }
```

/*Start of the code for the calculation of position*/

```
        if(hCBA.all==prev)
theta_e = theta_e + speed/28000;
        else
                {
                position();
                theta_e = theta_e + speed/28000;
                prev = hCBA.all;
                }
/*End of the code for the calculation of position*/

void position()
{
switch(hCBA.all)
        {
        case 0x0:
        case 0x7:   //fail_hall();
                break;
        case 0x4: //0 gradi
                theta_e = 0;
                break;
        case 0x6: //60 gradi
                theta_e = 1.04719755;
                break;
        case 0x2: //120 gradi
                theta_e = 2.09439510;
                break;
        case 0x3: //180 gradi
                theta_e = 3.14159265;
                break;
        case 0x1: //240 gradi
                theta_e = 4.18879020;
                break;
        case 0x5: //300 gradi
                theta_e = 5.23598775;
                break;
                }
        return;
}
```

5.3.2 Experimental results

Figures 5.3.3a and *5.3.3b* shows the acquird hall states and refrence currents generated for the two cases of phase current supply.

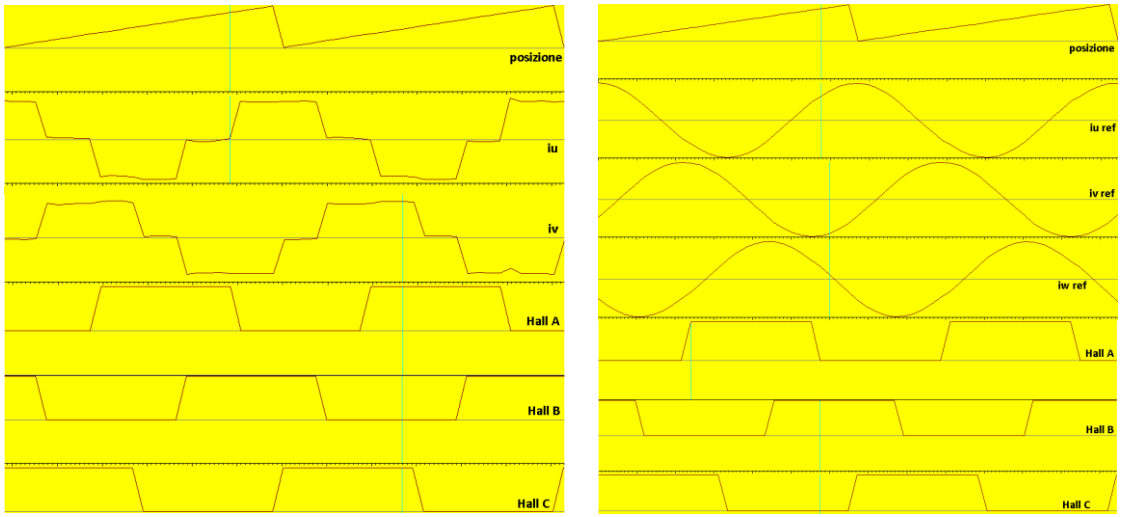

(a) (b)

Fig.5.3.3 Hall states and generated reference currents for: a) SqPC b) SPC supply

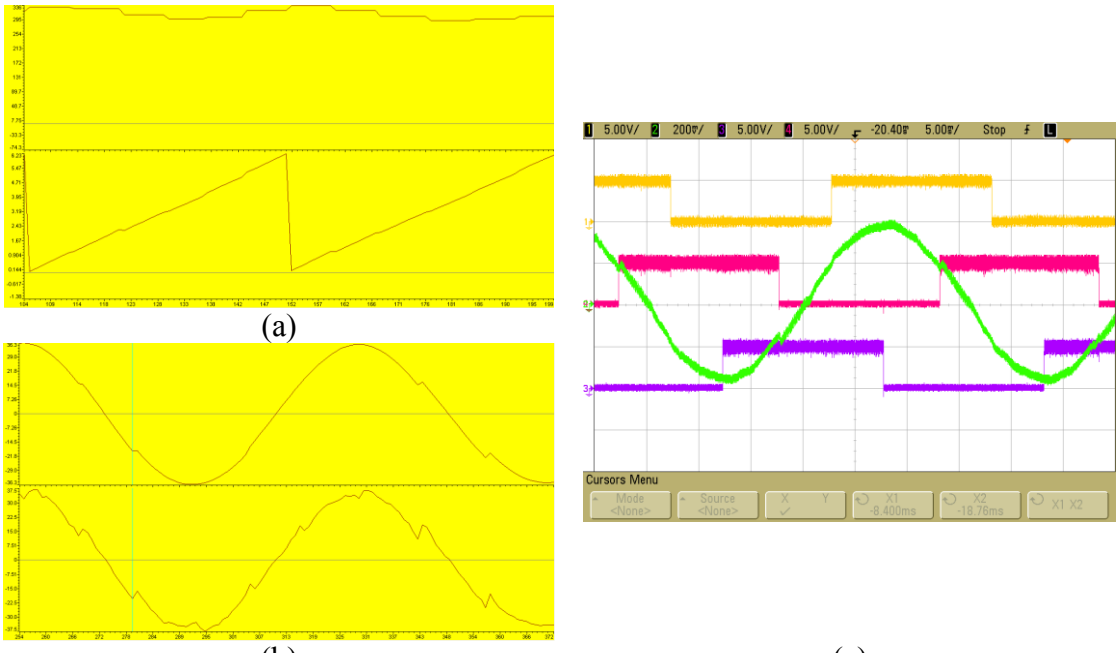

(a) (b) (c)

Fig. 5.3.4 a) estimated speed and position as per hall sensor positions; b) phase-a generated reference current and sampled current; c) phase-a current and hall signals as from oscilloscope, 25rad/sec mechanical speed

In *Figure 5.3.3* hall sensor signals aquired are complemented one. This so because in DSP interface circuit, the aquired hall signls are complemented from that of actual signals. *Figure 5.3.4a* shows the estimated speed and postion. *Figure 5.3.3b* shows the plot of

sampled value of phase-a current of as shown in *Figure 5.3.4c.* Ripples in actual and sampled current with the interval of 60° i.e. with each commutation and its correspondace with the ripples in estimated speed is confirmed by the appearance of ripple in the estimated position and refrecence current. Therefore, the selection of method for speed estimation is important. This problem of ripple is solved by adopting the approach, to update of speed information with measurement of duration of low state of individual hall sensors. And the position estimation is carried out with the falling edge of hall sensor *c*. Shift between square-wave and sinusoidal phase current supplies are shown in *Figure 5.3.5*.

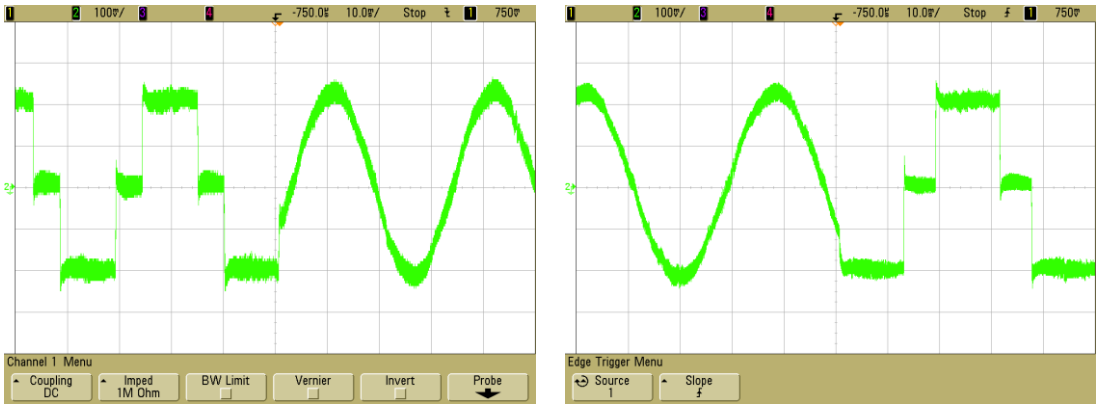

(a) (b)

Fig.5.3.5 Shift between square-wave and sinusoidal phase current supply

Figures 5.3.6a and *5.3.6b* show the traces of phase currents for a motor speed of about 200 and 600 rpm respectively, pointing out that they are effectively sine waves with superimposed oscillations at the PWM frequency.

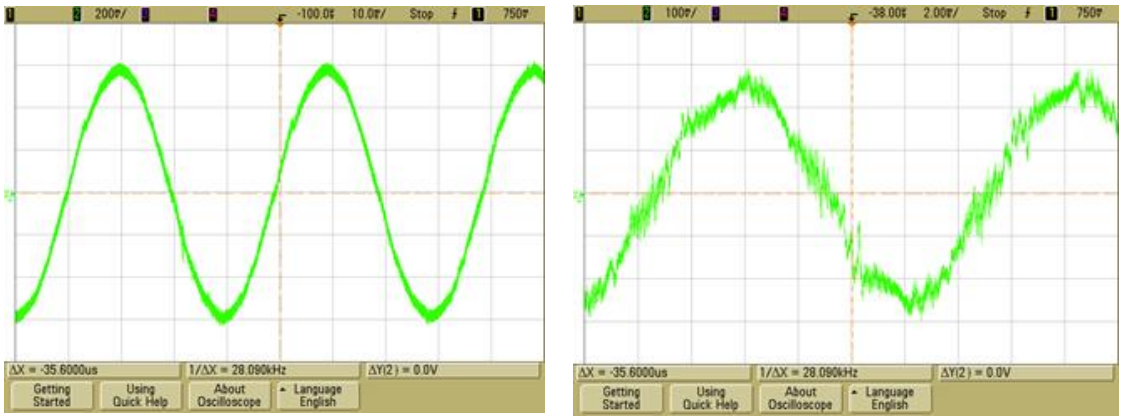

(a) (b)

Fig.5.3.6 Current waveform with sinusoidal current supply at about: a) 200 rpm and b) 600 rpm.

The first test refers to the PM BLDC drive operating in the constant torque zone at the nominal current whilst the second one refers to the drive operating in the voltage-limited zone at about half the nominal current. Note that the oscillations superimposed to the current are somewhat large due to the low inductance of the motor under test.

The torque-speed characteristic of the PM BLDC drive is found by measuring the torque developed by the motor for different speeds. With the view to find it correctly, a preliminary set of tests have been executed to determine the friction torque of the setup. To this purpose, the PM BLDC motor has been disconnected from the VSI and the torque requested to rotate the motor has been measured for different speeds. The friction torque helps braking the drive under test and hence it must be added to the torque developed by the brake drive to obtain the total torque developed by the motor under test. The resulting torque-speed characteristic of the PM BLDC drive both in the constant-torque zone and in the voltage-limited zone is reported in *Figure 5.3.7* with the blue circles. In the same figure, the results measured in [4] and reported in Chapter 4 for the same PM BLDC drive with square-wave current supply are reported with the red stars. The experimental characteristics fully agree with the theoretical findings, and demonstrate the overall superior torque characteristic achievable with the sinusoidal current supply.

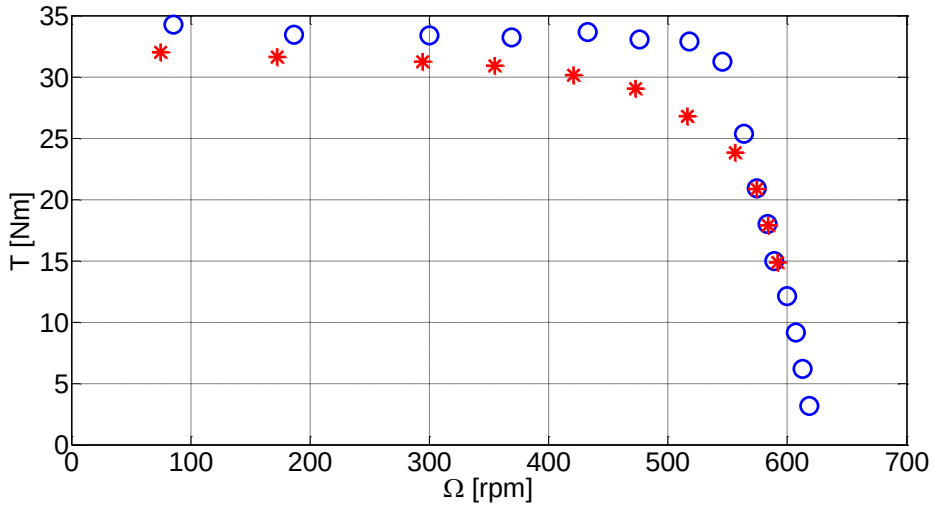

Fig.5.3.7 Current waveform with sinusoidal current supply at about: a) 200 rpm and b) 600 rpm.

5.4 Conclusion

This chapter has analyzed the convenience of supplying a PM BLDC motor with sinusoidal currents instead of with square-wave currents from the point of view of the torque performance, namely the motor torque and the torque ripple. Theoretical findings, corroborated by experimental results, have demonstrated that the torque performance obtained with sinusoidal current supply outperforms the square-current supply almost all over the speed range. The torque-speed characteristic is higher all along the speed range, especially nearly the nominal speed. The torque ripple is lower almost all along the speed range, apart from a speed interval centered at half the nominal speed and long about 22% of the nominal speed, where the torque ripple of a PM BLDC drive with square-wave current supply reduces due to the nearly complimentary profile between the injected current and the removed current.

5.5 References

[15] R.Carlson, M. Lajoie-Mazenc and J.C. dos S.Fagundes, “Analysis of Torque Ripple

Due to Phase Commutation in Brushless DC Machine", *IEEE Trans. on Ind. Appl.*, vol. 28, no. 3, pp. 632-638, May/June 1992.

[16] M. Bertoluzzo, G. Buja, R. Keshri, "Brushless DC Drive Operation during Phase Commutation under Various Switching Patterns", The 7th IEEE International Symposium on Diagnostics for Electric Machines, Power Electronics and Drives, 2009, SEDEMPED '09, pp 1-7, August 31-September 3,2009.

[17] R.Keshri, M.Bertoluzzo, A.Kumar, P.Thakura and G.Buja, "Generation of Possible Switching Patterns for VSI Using Micro-controller for the Control of PM BLDC Motor", Proceedings of the Indian International Conference on Power Electronics, 2010, January 28-30, 2011, New Delhi, India.

[18] M.Bertoluzzo, G.Buja, R.K.Keshri and R.Menis, "Analytical Study of Torque vs. Speed Characteristics of PM brushless DC drives", Proc. of 38th Annual Conf. on IEEE Industrial Electronics Society (IECON), 2012, pp. 1684-1689.

Chapter 6

Stationary-plane based investigation of PM BLDC drives

Summary - Vector approach in either stationary or synchronous plane is commonly used for the analysis of the AC drives like induction and PM brushless AC drives whilst it has been hardly ever used for the PM brushless DC (BLDC) drives. A possible reason is that they require injection of square-wave currents into the motor phases, which are non-sinusoidal in nature. This chapter proposes and applies vector approach in the stationary plane to an in-depth analysis of the operation of the PM BLDC drives during the current commutations, illustrating the potentialities of the approach in giving a better insight into the current transients and the ensuing torque characteristics [5]-[6]. At last, two voltage control strategies proposed to eliminate the torque ripple due to the current commutations are considered, showing that they can be readily understood by the vector approach.

6.1 Electrical dynamics of PM BLDC motor drive in stationary axis plane

6.1.1 PM BLDC drive

As discussed in *Chapter 4*, circuital schematic of PM BLDC drive is shown in *Figure 6.1.1.*

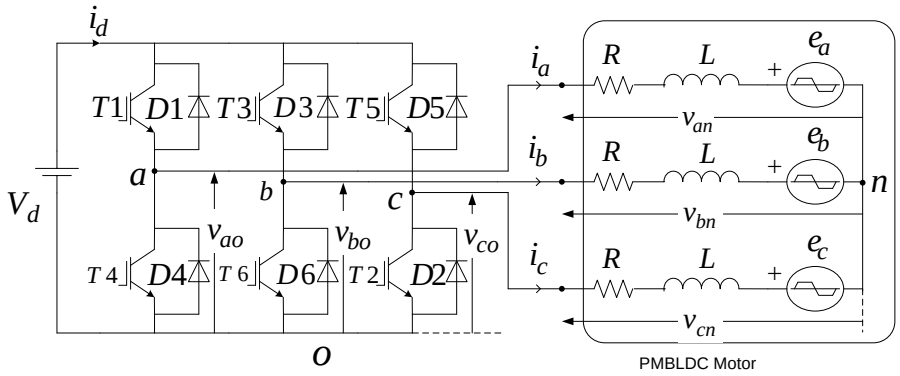

Fig. 6.1.1 Circuital schematic of a PM BLDC motor drive

Electrical dynamics of the drive expressed by (4.2.1) [Chapter 4] can be re-written as a function of rotor position in electrical radians θ_e

$$\left.\begin{aligned} &\frac{di_j(\theta_e)}{d\theta_e} = -\frac{R}{\Omega_e L} i_j(\theta_e) + \frac{1}{\Omega_e L} \underbrace{\left[v_{jn}(\theta_e) - e_j(\theta_e)\right]}_{v_{jL}(\theta_e)}; \quad j = \text{a, b, c} \\ &v_{jn} = v_{jo} - v_{no}; \quad \sum_{j=a,b,c} i_j = 0 \\ &v_{no} = \frac{1}{3}\sum_{j=a,b,c}\left(v_{jo} - e_j(\theta_e)\right) \end{aligned}\right\} \qquad (6.1.1)$$

Where $\theta_e = \Omega_e t$; $\Omega e = n_p \Omega$ is the electrical speed of the motor, n_p is the number of pole pairs and Ω is the mechanical speed of the motor in rad/sec.

The instantaneous electrical power p converted into mechanical form and the corresponding motor torque τ can be expressed as

$$p(\theta_e) = \sum_{j=a,b,c} e_j(\theta_e)\, i_j(\theta_e); \quad \tau(\theta_e) = \frac{p(\theta_e)}{\Omega} \qquad (6.1.2)$$

Figure 6.1.2 shows the trapezoidal back-emfs of the PM BLDC motor phases and the corresponding SqPCs (square-wave phase currents) injected into the motor phases in synchronism with the flat portion of the back-emf, so as to develop flat and constant torque.

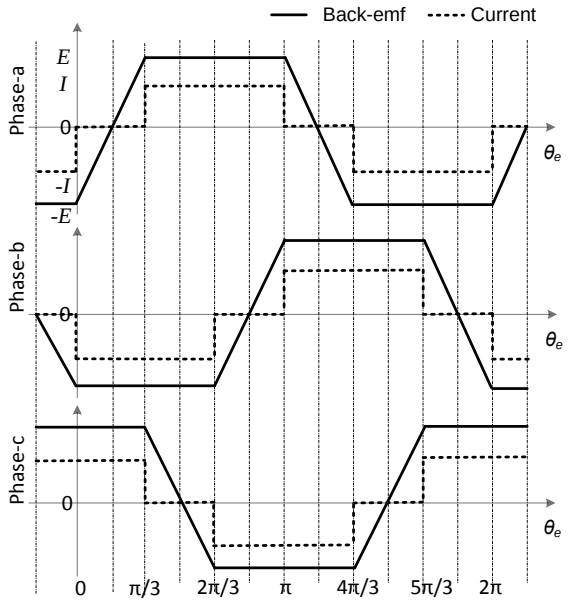

Supply intervals	S_6	S_1	S_2	S_3	S_4	S_5	S_6	S_1
Conducting transistors	5,4	5,6	1,6	1,2	3,2	3,4	5,4	5,6

Fig. 6.1.2 Circuital schematic of a PM BLDC motor drive

Magnitude of the flat portions of the back-emf equal to $+E$ or $-E$ and their duration equal to $2\pi/3$ (electrical) radians. The value of E is given by

$$E = k\Omega \qquad (6.1.3)$$

where k is the motor constant. For motor operation, the phase currents occupies $+I$ or $-I$ as per the sign of the back-emfs.

From *Figure 6.1.2*, it emerges that the supply period of the motor can be divided into six supply intervals S_1, S_2, ..., and S_6 of the duration of $\pi/3$ radians. At the beginning of each supply interval, one phase starts to conduct (incoming phase) and another one finishes of conducting (outgoing phase). During the remaining part of the supply interval, only two-phases with back-emfs of opposite polarities conduct (conducting phases). To identify the supply interval and, from it, the conducting transistors of the VSI, the drive control uses

the information delivered by three Hall sensors mounted on the stator and displaced of 2π/3 electrical radians. The required voltage is applied to the conducting phases by stepping down the DC link voltage V_d through choppering of the conducting transistors.

For the present case of study, DC-link current control of the PM BLDC drive is considered. Schematic of the control is shown in *Figure 6.1.3*.

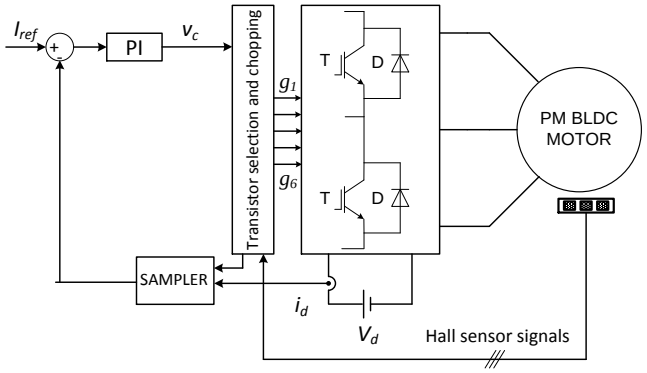

Fig. 6.1.3 Schematic of the control of a PM BLDC drive.

Regulation of the phase currents at the reference value I_{ref} can be accomplished by the closed-loop control of the DC link current i_d. In fact, this current remains equal to the current flowing into a motor phase when both the conducting transistors are ON; therefore, if properly sampled, the DC link current gives the feedback of the phase currents. The current error is processed by a PI regulator that delivers the required voltage v_c for the motor phases.

Application of v_c across the phases of the motor is commonly attained by chopping only one of the two conducting transistors to reduce the switching losses; a common strategy is to chop the transistor carrying either the incoming or the outgoing current. Hereafter, it is assumed that the control applies the required voltage without any delay.

6.1.2 Stationary plane representation

Time-varying three phase periodic quantities can be transformed to the quantities in stationary axis by α-β transformation. In case of star connected windings, where neutral point is not accessible, zero component of the transformation is not considered. For a three phase system with isolated neutral-point; if the variables in time space are x_a, x_b and x_c with phase displacement of -2π/3 and +2π/3 for phase-b and phase-c with respect to phase-a, stationary axis transformation is carried out by the expression (6.1.1).

$$\begin{bmatrix} x_\alpha \\ x_\beta \end{bmatrix} = \frac{2}{3}\begin{bmatrix} 1 & -\frac{1}{2} & -\frac{1}{2} \\ 0 & \frac{\sqrt{3}}{2} & -\frac{\sqrt{3}}{2} \end{bmatrix}\begin{bmatrix} x_a \\ x_b \\ x_c \end{bmatrix} \qquad (6.1.4)$$

Where x_α and x_β are the components of the time varying periodic quantity in stationary plane. Factor 2/3 in expression (6.1.1) is used to maintain amplitude variance, whereas

factor $(2/3)^{1/2}$ is used for power variance.

Equations of the PM BLDC motor can be written in terms of the vectors $\mathbf{i} = [i_\alpha\ i_\beta]^T$, $\mathbf{e} = [e_\alpha\ e_\beta]^T$, and $\mathbf{v} = [v_\alpha\ v_\beta]^T$ of the currents and the back-emfs of the motor phases, and the VSI output voltages in the stationary plane. The vectors, calculated with a magnitude-invariant transformation, are given by

$$\begin{aligned}
\mathbf{i}(\theta_e) &= i_a(\theta_e) + j\frac{1}{\sqrt{3}}\left[i_b(\theta_e) - i_c(\theta_e)\right] \\
\mathbf{v}(\theta_e) &= \frac{2}{3}\left[v_{ao}(\theta_e) - \frac{v_{bo}(\theta_e)}{2} - \frac{v_{co}(\theta_e)}{2}\right] + j\frac{1}{\sqrt{3}}\left[v_{bo}(\theta_e) - v_{co}(\theta_e)\right] \\
\mathbf{e}(\theta_e) &= \frac{2}{3}\left[e_a(\theta_e) - \frac{e_b(\theta_e)}{2} - \frac{e_c(\theta_e)}{2}\right] + j\frac{1}{\sqrt{3}}\left[e_b(\theta_e) - e_c(\theta_e)\right]
\end{aligned} \qquad (6.1.5)$$

By (6.1.5), the voltage equations in (6.1.1) become

$$\frac{d\,\mathbf{i}(\theta_e)}{d\theta_e} = -\frac{R}{\Omega_e L}\mathbf{i}(\theta_e) + \frac{1}{\Omega_e L}\underbrace{\left[\mathbf{v}(\theta_e) - \mathbf{e}(\theta_e)\right]}_{\mathbf{v_L}(\theta_e)} \qquad (6.1.6)$$

Calculation of the current and back-emf vectors for the waveforms in *Figure 6.1.2* shows that:

i). the current vector **i** remains stationary within the supply intervals S_1, S_2, ..., and S_6, and coincides with the radii $\mathbf{I_1}$, $\mathbf{I_2}$, **…**, and $\mathbf{I_6}$, respectively, of an hexagon (current hexagon)

ii). the back-emf vector **e** moves along the sides of an hexagon (back-emf hexagon) during the supply intervals, and coincides with the radii $\mathbf{E_1}$, $\mathbf{E_2}$, **…**, and $\mathbf{E_6}$ of the hexagon at the beginning of the supply intervals.

Current and back-emf vectors are traced in *Figure 6.1.4* whilst their values as a fraction of *I* and *E* are reported in *Table 6.1.1*.

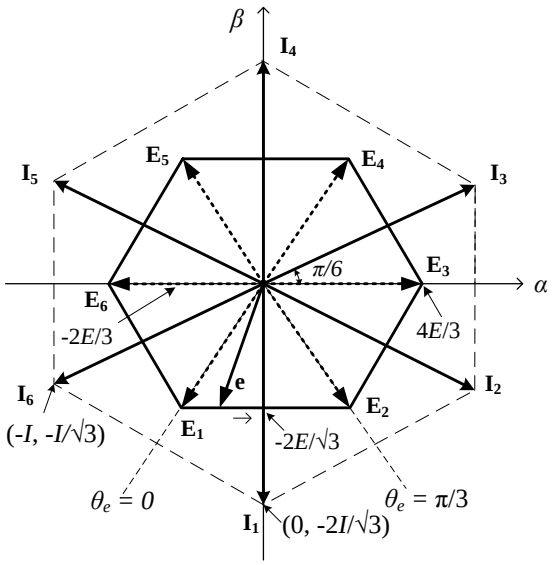

Fig. 6.1.4 Current and back-emf vectors in the stationary plane.

Table 6.1.1 Current and back-emf vectors in stationary plane		
Supply Interval	Current vectors (in fraction of *I*)	Back-emf vectors (in fraction of *E*)
S_1	$\mathbf{I_1} = -j\frac{2}{\sqrt{3}}$	$\mathbf{E_1} = -\frac{2}{3} - j\frac{2}{\sqrt{3}}$
S_2	$\mathbf{I_2} = 1 - j\frac{1}{\sqrt{3}}$	$\mathbf{E_2} = \frac{2}{3} - j\frac{2}{\sqrt{3}}$
S_3	$\mathbf{I_3} = 1 + j\frac{1}{\sqrt{3}}$	$\mathbf{E_3} = \frac{4}{3}$
S_4	$\mathbf{I_4} = j\frac{2}{\sqrt{3}}$	$\mathbf{E_4} = \frac{2}{3} + j\frac{2}{\sqrt{3}}$
S_5	$\mathbf{I_5} = -1 + j\frac{1}{\sqrt{3}}$	$\mathbf{E_5} = -\frac{2}{3} + j\frac{2}{\sqrt{3}}$
S_6	$\mathbf{I_6} = -1 - j\frac{1}{\sqrt{3}}$	$\mathbf{E_6} = -\frac{4}{3}$

As an example, in the supply interval S_1 the current vector jumps from $\mathbf{I_6}$ (-*I*, *I*/√3) to $\mathbf{I_1}$ (0, -2*I*/√3) at $\theta_e = 0$ and, after that, stays at $\mathbf{I_1}$ within the whole S_1. Instead, the back-emf vector takes the value $\mathbf{E_1}$ (-2*E*/3, -2*E*/√3) at $\theta_e = 0$ and moves towards $\mathbf{E_2}$ (2*E*/3, -2*E*/√3) during S_1, reaching $\mathbf{E_2}$ at $\theta_e = \pi/3$. For given values of *I* and *E*, the magnitude of the current vector remains the same and equal to 2*I*/√3, whereas the magnitude of the back-emf vector undergoes a continuous change from the maximum value of 4*E*/3 at the beginning of the supply interval to the minimum value of 2*E*/√3 at the mid of supply interval and then again to the maximum value of 4*E*/3 at the end of the supply interval.

Power equation in (6.1.2) can be expressed in terms of the inner product of the vectors **e** and **i** as

$$p(\theta_e) = \frac{3}{2}\mathbf{e}(\theta_e) \bullet \mathbf{i}(\theta_e) = \frac{3}{2}\left[e_\alpha(\theta_e) i_\alpha(\theta_e) + e_\beta(\theta_e) i_\beta(\theta_e)\right] \qquad (6.1.7)$$

For the ideal case of instantaneous commutation, during the interval -$0 \le \theta_e \le \pi/3$ the magnitude of the projection of **e** over **i** is constant and equal to 2*E*/√3. Thus the motor torque in (6.1.2) turns out to be constant and equal to

$$\mathrm{T} = 2kI \qquad (6.1.8)$$

6.2 Current commutation

In practice, the incoming and outgoing currents take some time to get the required magnitude and the current commutation is not instantaneous. The analysis of the PM BLDC drive operation during the current commutations is carried out by supposing that

i). the voltage drop across the phase resistances is negligible compared to the other voltage terms in (6.1.6), so that it can be disregarded,

ii). the commutation interval is small compared to the maximum allowed interval of $\pi/3$ [1] so that **e** remains equal to the back-emf vector taken at the beginning of the relevant supply interval.

Above assumptions reduce (6.1.6) to

$$\frac{d\,\mathbf{i}(\theta_e)}{d\theta_e} = \frac{1}{\Omega_e L}\underbrace{\left[\mathbf{v}(\theta_e) - \mathbf{E_1}\right]}_{\mathbf{v_L}(\theta_e)} \qquad (6.1.9)$$

For the supply interval S_1 (6.1.9) shows that the change in the current vector is parallel to $\mathbf{v_L}$.

Let us consider the current commutation taking place at the beginning of the supply interval S_1, which starts at $\theta_e = 0$ as in *Figure 6.1.2*. The drive control system turns T_4 OFF and T_6 ON, and keeps T_5 ON. The commutating currents are i_b and i_a, with i_b that is ingoing and i_a that is outgoing, whilst i_c is the non-commutating current. Current i_a freewheels through D_1 until it extinguishes.

Generally, the commutation interval is divided into two subintervals, and the current transients depend on whether the motor runs in the low-speed zone, which occurs for $V_d > 4E$, or in the high-speed zone, which occurs for $V_d < 4E$ [2]. The current transients in the two speed zones and for $V_d = 4E$ are shown in *Figure 6.2.1*, where the duration of the commutation interval is denoted with θ_c, and the two commutation subintervals are marked with #1 and #2. Hereafter, quantities pertinent to the low-speed zone are identified with the subscript *l* and those to the high-speed zone with the subscript *h*.

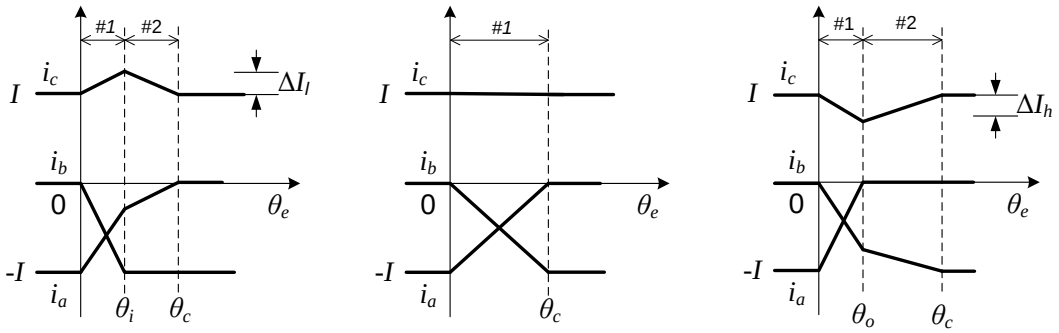

Fig. 6.2.1 Current transients during commutation: a) in the low-speed zone ($4E<V_d$), b) for $4E=V_d$, and c) in the high-speed zone ($4E>V_d$).

6.2.1 Current transients in subinterval #1

During subinterval #1, all the three motor phases conduct and the VSI exerts the maximum effort to the motor for the commutating currents to reach the required magnitudes, i.e. it is $v_{ao} = V_d$, $v_{bo} = 0$ and $v_{co} = V_d$. From (6.1.5), the vector of the VSI output voltages during subinterval #1is

$$\mathbf{V_1} = \left(\frac{1}{3} - j\frac{1}{\sqrt{3}}\right)V_d \qquad (6.2.1)$$

The vector has fixed magnitude and is aligned along $\mathbf{E_2}$. By (6.19) and (6.2.1), the vector of the voltage drops across the phase inductances is

$$\mathbf{V_{L,1}} = \mathbf{V_1} - \mathbf{E_1} = \frac{1}{3}(V_d + 2E) - j\frac{1}{\sqrt{3}}(V_d - 2E) \qquad (6.2.2)$$

The vector in (6.2.2) has a slope of

$$m_1 = -\sqrt{3}\left(\frac{V_d - 2E}{V_d + 2E}\right) \qquad (6.2.3)$$

which is a function of E and, therefore, depends upon the motor speed Ω.

Integration of (6.1.9) with the initial condition $\mathbf{i}(0) = \mathbf{I}_6$ leads to the current vector $\boldsymbol{i}$ during subinterval #1

$$\mathbf{i_1}(\theta_e) = \frac{1}{\Omega_e L}\left[\frac{1}{3}(V_d + 2E) - j\frac{1}{\sqrt{3}}(V_d - 2E)\right]\theta_e + \mathbf{I}_6 \qquad (6.2.4)$$

From (6.2.3) and (6.2.4) it can be concluded that the current vector during subinterval #1 moves towards $\mathbf{I_1}$ along a straight line with the slope in (6.2.3).

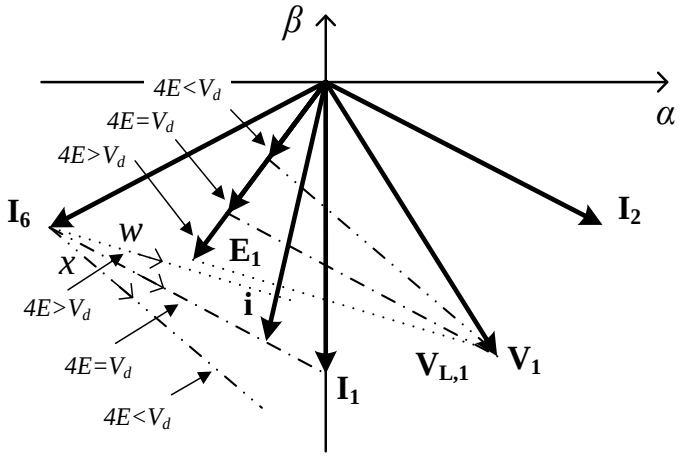

Fig. 6.2.2 Current vector trajectories during subinterval #1.

So, as shown in *Figure 6.2.2*, there are three possible trajectories of the tip of the current vector:

i). in the low speed zone, i.e. for $4E<V_d$, m_1 is less than $-1/\sqrt{3}$ and the tip of $\boldsymbol{i_1}$ moves along a line like *x,* which has an angular slope in the range from $-\pi/6$ to $-\pi/3$,

ii). for $4E=V_d$, m_1 becomes equal to $-1/\sqrt{3}$ and the tip of $\boldsymbol{i_1}$ moves along the line joining $\boldsymbol{I_6}$ and $\boldsymbol{I_1}$, which has an angular slope of $-\pi/6$, and

iii). in the high speed zone, i.e. for $4E>V_d$, m_1 becomes greater than $-1/\sqrt{3}$ and the tip of $\boldsymbol{i_1}$ moves along a line like *w*, which has an angular slope in the range from 0 to $-\pi/6$.

Subinterval #1 ends in three possible modes:

i). for $4E<V_d$, the incoming current i_b reaches the required magnitude $-I$ at the angle θ_i before that i_a the outgoing current vanishes [*Figure 6.2.1a*];

ii). for $4E=V_d$, i_b reaches $-I$ at the same angle that i_a vanishes and the commutation completes at the end of the subinterval #1, [*Figure 6.2.1b*]

iii). for $4E>V_d$, i_a vanishes at the angle θ_o before that i_b reaches $-I$ [*Figure 6.2.1c*].

In both the modes i) and iii), the commutation continues with a second subinterval where i_a vanishes and i_b gets the required magnitude; at the completion of this subinterval, denoted with #2, commutation is completed and the current vector becomes equal to $\boldsymbol{I_1}$. Subinterval #2 lasts $\theta_{ci} = \theta_{cl} - \theta_i$ in mode i) and $\theta_{co} = \theta_{ch} - \theta_o$ in mode iii).

6.2.2 Current transients in low-speed zone

During subinterval #1 the tip of the current vector moves along a line like *x*, as explained in the previous Subsection. At the end of the subinterval #1, the current of phase *b* reaches the required magnitude $-I$, i.e. it is $i_{bl}(\theta_i) = -I$, while the current of phase *a* is still flowing.

During subinterval #2, the drive control system regulates i_b at $-I$ by applying the voltage $v_{bo} = V_d - E$ at the output *b* of the VSI, while the other two outputs of the VSI are kept at the same voltages as before, i.e. it is $v_{ao}=V_d$, and $v_{co} = V_d$, for i_a to vanish. The vectors of the VSI output voltages and the voltage drops across the phase inductances are expressed as

$$\mathbf{V}_{2\ell} = \left(\frac{1}{3} - j\frac{1}{\sqrt{3}}\right)E \qquad (6.2.5)$$

$$\mathbf{V}_{L,2\ell} = \left(1 + j\frac{1}{\sqrt{3}}\right)E \qquad (6.2.6)$$

Both the vectors have a magnitude that depends on the speed and a slope that is independent of the speed. In particular, the slope of the vector in (6.2.6) is

$$m_{2\ell} = \frac{1}{\sqrt{3}} \qquad (6.2.7)$$

that, as shown in *Figure 6.2.3*, is the same as the line *s*. Substitution of (6.2.6) into (6.1.9) and integration of (6.1.9) give the current vector in subinterval #2

$$\mathbf{i}_{2\ell}(\theta_e - \theta_i) = \left(1 + j\frac{1}{\sqrt{3}}\right)\frac{E}{\Omega_e L}(\theta_e - \theta_i) + \mathbf{i}_{1\ell}(\theta_i) \quad \theta_e > \theta_i \qquad (6.2.8)$$

where $\mathbf{i}_{1l}(\theta_i)$ is the current vector at the end of subinterval #1. The angle θ_i can be obtained by calculating the current vector at $\theta_e=\theta_i$ by means of the first equation in (6.1.5), which becomes

$$\mathbf{i}_{1\ell}(\theta_i) = i_a(\theta_i) + j\frac{1}{\sqrt{3}}\left[-2I + i_a(\theta_i)\right] \qquad (6.2.9)$$

Then, by equating the real and imaginary parts of (6.2.9) to (6.2.4), also calculated at $\theta_e=\theta_i$, the values of θ_i and $i_a(\theta_i)$ can be obtained. In particular, θ_i results in

$$\theta_i = \frac{3\Omega_e LI}{2(V_d - E)} \qquad (6.2.10)$$

Finally, substitution of (6.2.10) into (6.2.4) yields $\mathbf{i}_{1l}(\theta_i)$.

The trajectory of the tip of the current vector in subinterval #2, i.e. of $i_{2l}(\theta_e - \theta_i)$, is a straight line having the slope in (6.2.7). Since the current vector coincides with $\mathbf{I_1}$ at the end of subinterval #2, and the slope of the vector $\mathbf{I_{21}}=\mathbf{I_2} - \mathbf{I_1}$ is the same as (6.2.7), the trajectory is represented by the line *s* of *Figure 6.2.3* that passes through the tips of the vectors $\mathbf{I_1}$ and $\mathbf{I_2}$. Thus, it can be stated that subinterval #1 ends when the line *x* intersects the line *s*.

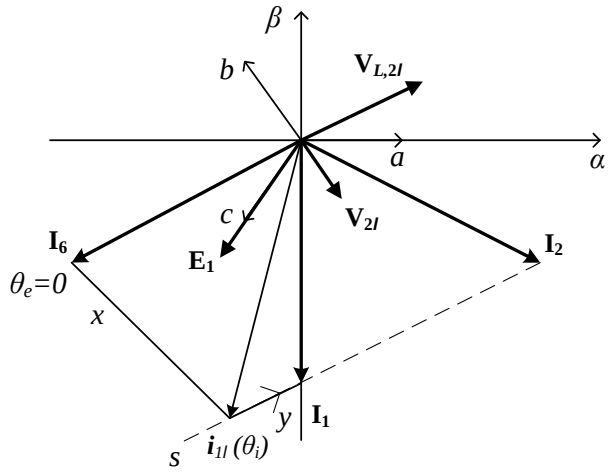

Fig. 6.2.3. Phase vectors during subinterval #2 in low-speed zone.

Subinterval #2 finishes when the current vector reaches $\mathbf{I_1}$. This occurs when the current of the phase *a* vanishes. Being i_a equal to the real part of the current vector, the duration of subinterval #2 can be obtained by equating to zero the real part of (6.2.8) calculated at $\theta_e=\theta_{cl}$. It is

$$\theta_{ci} \equiv \theta_{c\ell} - \theta_i = \frac{\Omega_e LI}{2E}\left(\frac{V_d - 4E}{V_d - E}\right) \qquad (6.2.11)$$

and, from (6.2.1.) and (6.2.11), the duration of the commutation interval is

$$\theta_{c\ell} = \frac{\Omega_e LI}{2E} \equiv \frac{n_p LI}{2k} \qquad (6.2.12)$$

It is worth to note that the commutation interval does not depend on the motor speed and, furthermore, it coincides with the commutation interval as obtained for $4E=V_d$.

The transients of the phase currents in the low-speed zone drawn in *Figure 6.2.1a* can be readily found by projecting the current vector on the axes *a, b*, and *c* of *Figure 6.2.3*.

6.2.3 Current transients in high-speed zone

During subinterval #1 the tip of the current vector moves along a line like *w*, as explained in Subsection A). At the end of the subinterval #1, the current of phase *a* vanishes, i.e. it is $i_{ah}(\theta_o)=0$, while the current of phase *b* is still on the way to get the required magnitude. This means that at $\theta_e=\theta_o$ the real part of the current vector becomes zero and hence subinterval #1 finishes when the line *w* intersects the current vector $\mathbf{I}_1$.

The angle θ_o is found by equating to zero the real part of (6.2.4) calculated at $\theta_e=\theta_o$ and is equal to

$$\theta_o = \frac{3\Omega_e LI}{V_d + 2E} \tag{6.2.13}$$

Substitution of $\theta_e=\theta_o$ in (6.2.4) results in only imaginary part and gives the current vector at the end of subinterval #1; it is

$$\mathbf{i}_{1h}(\theta_o) = -j\left[4\left(\frac{V_d - E}{V_d + 2E}\right)\right]\frac{I}{\sqrt{3}} \tag{6.2.14}$$

As anticipated, the vector is aligned along $\mathbf{I}_1$ and has a magnitude lower than $2I/\sqrt{3}$.

During subinterval #2, the control system does not chop the VSI transistors T_6 and T_5 but keeps them ON to facilitate the incoming current to reach the required magnitude. Then only the legs *b* and *c* of the VSI conduct and the voltage of the neutral point of the motor with respect to *o* is $V_d/2$. Let us suppose that the leg *a* is fictitiously chopped at the voltage of $v_{ao} = e_a + V_d/2$ so as to maintain the zero current condition for the phase *a*. The other output voltages of the VSI are $v_{bo} = 0$ and $v_{co} = V_d$. Thus the vector of the output VSI voltages can be determined and results in

$$\mathbf{V}_{2h} = -\frac{2}{3}E - j\frac{1}{\sqrt{3}}V_d \tag{6.2.15}$$

whilst the vector of the voltage drops across the phase inductances becomes

$$\mathbf{V}_{L,2h} = -j\frac{1}{\sqrt{3}}(V_d - 2E) \tag{6.2.16}$$

The two voltage vectors in (6.2.15) and (6.2.16) have both the magnitude and the slope that depend on the motor speed.

From (6.1.9) and (6.2.16), the current vector is given by

$$\mathbf{i}_{2h}(\theta_e - \theta_o) = -j\frac{1}{\sqrt{3}}\left(\frac{V_d - 2E}{\Omega_e L}\right)(\theta_e - \theta_o) + \mathbf{i}_{1h}(\theta_o) \tag{6.2.17}$$

Eqs. (6.2.14) and (6.2.17) points out that the tip of the current vector moves along the imaginary axis as shown in *Figure 6.2.4*. Magnitude of the vector increases and then the tip continues to advance along $\mathbf{I}_1$ until it reaches the tip of $\mathbf{I}_1$ at $\theta_e = \theta_{ch}$. Duration of subinterval #2 is obtained by equating (6.2.17) at $\mathbf{I}_1$. It is

$$\theta_{co} \equiv \theta_{ch} - \theta_o = \frac{2\Omega_e LI\left(4E - V_d\right)}{\left(V_d - 2E\right)\left(V_d + 2E\right)} \qquad (6.2.18)$$

and, from (6.2.13) and (6.2.18), the duration of the commutation interval is

$$\theta_{ch} = \frac{\Omega_e LI}{V_d - 2E} \qquad (6.2.19)$$

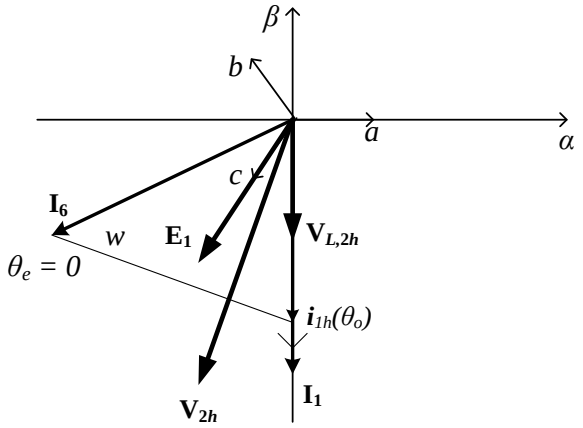

Fig. 6.2.4. Phase vectors during subinterval #2 in high-speed zone.

The transients of the phase currents in the high-speed zone drawn in *Figure 6.2.1c* can be readily found by projecting the current vector on the axes *a, b*, and *c* of *Figure 6.2.4*. As discussed in [1], in high-speed zone $\mathbf{i}_{2h}$ must equate $\mathbf{I}_1$ within $\theta_e=\pi/3$ to get the required current reference at least at the end of the allowed commutation interval, i.e. of the supply interval.

6.3 Effects of current commutations on motor torque

The instantaneous motor torque during current commutations can be still calculated by (6.1.3) and (6.1.7). For the current commutation occurring at the beginning of supply interval S_1, the instantaneous motor torque can be expressed as

$$\tau\left(\theta_e\right) = \frac{3}{2\Omega}\mathbf{E}_1 \bullet \mathbf{i}\left(\theta_e\right) \qquad (6.3.1)$$

By (6.3.1), the torque changes during the commutation interval. The change is proportional to the projection of $[\mathbf{i}(\theta_e) - \mathbf{I}_1]$ on $\mathbf{E}_1$ and, by accounting of the expressions of $\mathbf{i}(\theta_e)$, the change is a linear function of θ_e.

In the low-speed zone, the projection of $\mathbf{i}(\theta_e)$ on $\mathbf{E}_1$ is greater than the projection of $\mathbf{I}_1$ and the instantaneous motor torque has a positive dip. The torque ripple, which is the absolute of the maximum excursion, is equal to

$$TR_\ell = \left|\frac{3}{2}\left\{\frac{\mathbf{E_1} \bullet \left[\mathbf{i}_{1\ell}(\theta_i) - \mathbf{I}_1\right]}{\Omega}\right\}\right| \qquad (6.3.2)$$

After some manipulations the following expression is obtained for (6.3.2)

$$TR_{\ell} = \frac{n_p I}{\Omega_e}\left[\frac{(V_d - 4E)E}{V_d - E}\right] \tag{6.3.3}$$

In the high-speed zone, the projection of $\mathbf{i}(\theta_e)$ on $\mathbf{E}_1$ is lower than the projection of $\mathbf{I}_1$ and the instantaneous motor torque has a negative dip. The torque ripple is now equal to

$$TR_h = \left|\frac{3}{2}\left\{\frac{\mathbf{E_1} \bullet [\mathbf{i}_{1h}(\theta_o) - \mathbf{I}_1]}{\Omega}\right\}\right| \tag{6.3.4}$$

After some manipulations the following expression is obtained for (6.3.4)

$$TR_h = \left|\frac{2n_p I}{\Omega_e}\left[\frac{(4E - V_d)E}{V_d + 2E}\right]\right| \tag{6.3.5}$$

From *Figures. 6.2.3* and *6.2.4*, it can be easily realized that the torque ripple in both the low-speed and high-speed zones is proportional respectively to the maximum swing of the current of phase *c*.

Due to the torque dip, the motor torque, defined as the average value of the instantaneous motor torque over a supply period, changes with respect the expected value in (6.1.8), by increasing in the low-speed zone and decreasing in the high-speed zone. The terms in excess and in defect can be found by calculating the average value of the torque dip over the supply interval $\pi/3$. It comes out

$$\Delta T_l = \frac{3}{\pi}\frac{1}{2} TR_l \theta_{cl} \tag{6.3.6}$$

$$\Delta T_h = -\frac{3}{\pi}\frac{1}{2} R_h \theta_{ch} \tag{6.3.7}$$

By substituting (6.2.12) and (6.3.3) into (6.3.6), and (6.2.19) and (6.3.5) into (6.3.7), the following expressions can be obtained for the two terms

$$\Delta T_l = \frac{3n_p L I^2}{4\pi}\left[\frac{V_d - 4E}{V_d - E}\right] \tag{6.3.8}$$

$$\Delta T_h = -\frac{3n_p L I^2}{\pi}\left[\frac{(4E - V_d)E}{(V_d + 2E)(V_d - 2E)}\right] \tag{6.3.9}$$

6.4 Exemplification

To demonstrate the potentialities of the vector approach in analyzing the operation of a PM BLDC drive, two control techniques of the VSI during the current commutations are considered, that have been proposed to eliminate the torque ripple produced by the commutations in the low-speed zone [3] and in the high-speed zone [4], respectively.

6.4.1 Low-speed zone

The control technique in [3] proposes to slow down reaching of the required magnitude from the incoming current i_b by forcing it to have a magnitude complementary to that one of the outgoing current i_a, i.e. by taking constant the sum of the magnitudes of i_b and i_a and equal to the required current magnitude $-I$. To fulfill this condition, [3] chops the transistor T_6 of the incoming phase during the commutation interval with the following duty-cycle:

$$\delta_l = \frac{4E}{V_d} \tag{6.4.1}$$

The VSI output voltages are then: $v_{ao}=V_d$, $v_{bo}=(1-\delta_l)V_d$, $v_{co}=V_d$. By (6.1.5) and (6.1.9), the vectors of the VSI output voltages and the voltage drops across the phase inductance become

$$\mathbf{V}_{1l} = \left[\frac{1}{3} - j\frac{1}{\sqrt{3}}\right]4E \tag{6.4.2}$$

$$\mathbf{V}_{L,1l} = \left[1 - j\frac{1}{\sqrt{3}}\right]2E \tag{6.4.3}$$

Note that the voltage vector in (6.4.2) has the same direction as $\mathbf{V}_1$ in (6.2.1) and a magnitude scaled of δ_l. As it can be recognized from *Figure 6.4.1*, this control technique forces the voltage vector (6.4.3) to stay in parallel to the line joining $\mathbf{I}_6$ and $\mathbf{I}_1$ irrespectively from the motor speed, so that the current vector during the commutation moves along this line and its magnitude does not exhibit any positive swing. The commutation interval spans only subinterval #1 as the incoming current reaches the required magnitude at the same time as the outgoing current vanishes, and the commutation angle is still given by (6.2.12).

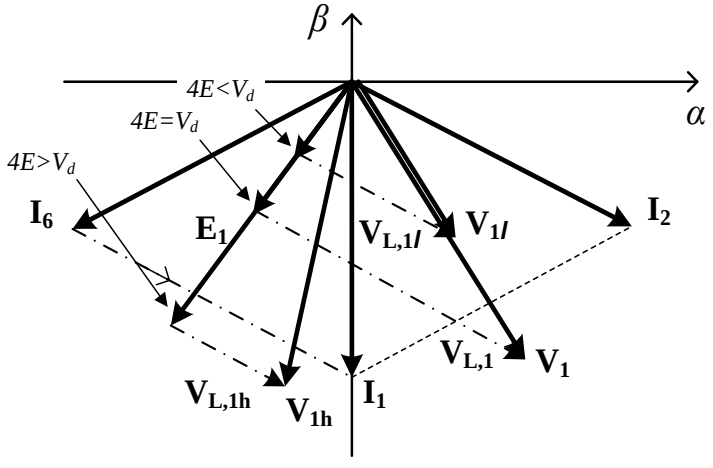

Fig. 6.4.1. PM BLDC control techniques to eliminate torque ripple.

Clearly, the duty-cycle in (6.4.1) can be applied only for $4E<V_d$, i.e. for $\delta_l<1$, and hence this technique is effective only in the low-speed zone.

6.4.2 High-speed zone

The control technique in [4] proposes to slow down vanishing of the outgoing current i_a by forcing it to have a magnitude complementary to that one of the incoming current i_b, i.e. by taking constant the sum of the magnitudes of i_b and i_a and equal to the required current magnitude -*I*. To fulfill this condition, [4] chops the transistor T_4 of the outgoing phase during the commutation interval with the following duty-cycle:

$$\delta_h = \frac{4E}{V_d} - 1 \qquad (6.4.4)$$

The VSI output voltages are then: $v_{ao}=(1-\delta_h)V_d$, $v_{bo}=0$, $v_{co}=V_d$. By (6.1.5) and (6.1.9), the vectors of the VSI output voltages and the voltage drops across the phase inductance become

$$\mathbf{V}_{1h} = \left(V_d - \frac{8}{3}E\right) - j\frac{1}{\sqrt{3}}V_d \qquad (6.4.5)$$

$$\mathbf{V}_{L,1h} = \left(1 - j\frac{1}{\sqrt{3}}\right)(V_d - 2E) \qquad (6.4.6)$$

Note that direction of the vector in (6.4.5) depends on the motor speed; in spite of this, the vector in (6.4.6) is parallel to the line joining $\mathbf{I}_6$ and $\mathbf{I}_1$ irrespectively from the motor speed, as shown in *Figure 6.4.1*, so that the current vector during the commutation moves along this line and does not exhibit any swing. Therefore this control technique operates in a similar way that the technique in the low-speed zone but with the difference of chopping the output VSI voltage of the outgoing phase instead of the incoming one. As above, the commutation interval spans only subinterval #1 as the incoming current reaches the required magnitude at the same time as the outgoing current vanishes. Here, instead, the commutation angle changes with the speed and is given by

$$\theta_c = \frac{\Omega_e LI}{V_d - 2E} \qquad (6.4.7)$$

As an example, *Figure 6.4.2* gives the trajectory on α, β plane of the current vector obtained without and with the control technique. The curves, obtained by simulation, clearly show the beneficial effect of the control.

Clearly, the duty-cycle in (6.4.4) can be applied only for $4E>V_d$ and up to $2E=V_d$, i.e. for $\delta_h<1$, and hence this technique is effective only in the high-speed zone. Note that extension of (6.4.5)-(6.4.7) to the case of $2E=V_d$ leads to the situation where the DC link voltage is no more able to inject any current into the motor phases at the voltage drop on the phase inductances is zero.

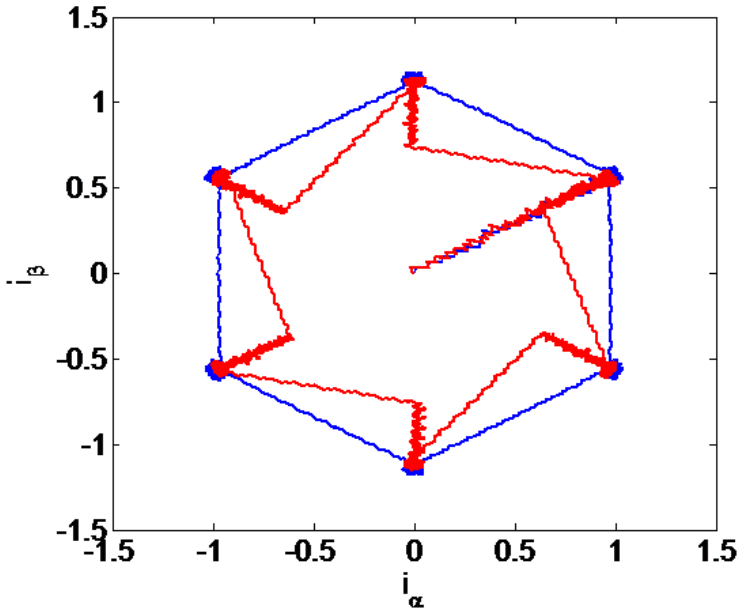

Fig. 6.4.2. Example of α, β plane trajectory of the current vector without (red line) and with (blue line) VSI control during the current commutations at high speed.

6.5 Conclusions

The current transients during the commutations of the PM BLDC drives have been analyzed in the stationary plane with the help of the vector representation of the drive variables. Vectors of the VSI output voltages and the voltage drops on the phase inductances have been calculated and utilized to get the current vector trajectories for different motor speeds as well as to find out the commutation intervals. The results of the analysis have been used to obtain the motor torque and the torque ripples due to the current commutations. Lastly, the vector approach has been applied to two control techniques of the PM BLDC drives with the end of explaining how they operate to eliminate the torque ripples due to the current commutations.

6.6 References

[1] M.Bertoluzzo, G.Buja, R.Keshri, and R.Menis, "Analytical study of torque vs. speed characteristics of PM brushless DC drives," in Proc. Annual Conf. of Industrial Electronics Society (IECON), 2012, pp. 1675-1680.

[2] R.Carlson, M.Lajoie-Mazenc, and J.C. dos S.Fagundes, "Analysis of torque ripple due to phase commutation in brushless DC machine," IEEE Trans. on Industry Applications, vol.28, no.3, pp.632-638, May/Jun. 1992.

[3] J.Fang, H.Li, and B.Han, "Torque ripple reduction in BLDC torque motor with non-ideal back EMF", IEEE Trans. on Power Electronics, vol.27, no.11, pp. 4630-4637, Nov. 2012

[4] J.H.Song and I.Choy, "Commutation torque ripple reduction in brushless DC motor drives using a single DC current sensor," IEEE Trans. on Power Electronics, vol.19,

no.2, pp. 312-319, March 2004.

[5] G.Buja, M.Bertoluzzo, R.Keshri, and R.Menis, “Stationary plane based investigation of the behavior of PM BLDC Drives,” in Proc. of IEEE Annual Conf. on Industrial Electronics (IECON), 2013, pp. 6630-6635.

[6] G.Buja, R.Menis, and R.Keshri, “Vector analysis of the current commutation in PM BLDC drives,” Bulletin of Polish Academy of Sciences: Tech Sciences, vol. 61, no. 4, pp. 1-8, 2013 [in press].

Chapter 7

Integration of Photovoltaic panel with an Electric Mini-car

Summary: Solar energy is a clean, inexhaustible, abundantly and universally available source of energy. Use of solar energy for the space exploration is common and its way of utilizations for other means of transportation especially for electric vehicles, ships and airships are being explored. Utilization of solar energy for light electric vehicles is a concern due to limited available on board space and lower efficiency of photovoltaic (PV) modules. Even under such constraints, for the cases where such vehicles are in parking during office hour and/or mobility is limited within the city, solar energy can be utilised to assist energy sources, like battery, ultra-capacitors or the combination of these. Autonomy of the electric vehicles can be improved by reducing the dependency of auxiliary supplies on main energy sources. This dependency can be reduced by delivering the energy requested by the auxiliaries through the charge to batteries from photovoltaic module mounted on the vehicle. Present chapter at first discusses the basics of solar irradiation, photovoltaic and datasheet specifications together with the characteristics of a photovoltaic module. Then a discussion on estimation of solar irradiance available in Padova, (Italy) is carried out for the calculation of input and output power of a given module. After this design and the experimentation of a high gain DC-to-DC boost converter for the integration of photovoltaic module with the battery of the mini-electric car is discussed. Efficiency measurement of the developed converter under real situation through experimental arrangement is carried and the results were explained with the help of developed analytical model for the efficiency measurement. At the end possible extension in the autonomy of the mini-electric car is explained.

7.1 Solar irradiation and photovoltaic

7.1.1 Solar irradiation

Sun is approximated as a perfect black body which radiates energy in all the directions in the form of electromagnetic waves. Average solar power received by the earth surface is approximately 1.2×10^{14}*k*W. Solar radiation reaching to earth is clean, inexhaustible, abundantly and universally available source of energy.

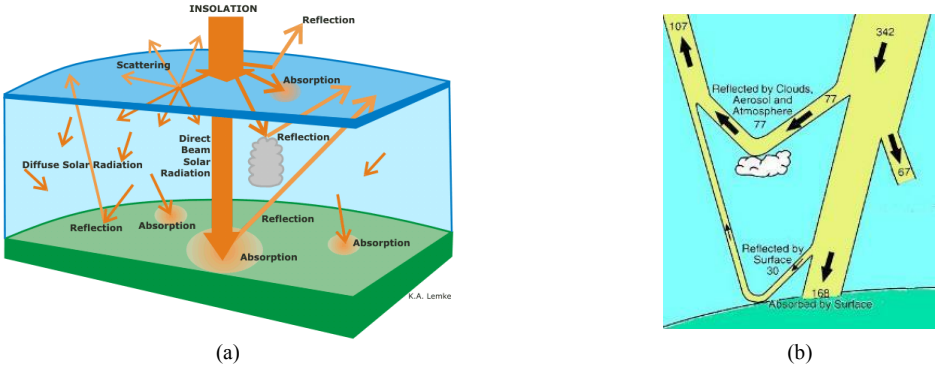

(a) (b)

Fig. 7.1.1 a) Solar radiation through Earth's atmosphere b) distribution of average flux incident

Figure 7.1.1 shows the solar radiation through the Earth's surface. Solar radiation incident on the outer atmosphere of the earth is known as extra-terrestrial radiation and the solar radiation reaching the earth surface is called terrestrial radiation. Average solar energy incident on a unit area perpendicular to the direction of propagation of the radiation outside the earth's atmosphere is known as solar constant 'S' and is equal to 1367W/m^2. Total power falling on a unit area is termed as solar irradiance.

Average solar energy incident on a unit surface area is obtained by dividing total solar energy incident on the earth (= S × πR^2) by total surface area of the Earth (=4πR^2) and is equal to S/4 i.e. 342W/m^2, where R is the radius of the Earth.

When solar radiation enters into the Earth's atmosphere, a part of it suffers scattering and absorption by aerosol, clouds and atmosphere. Scattered radiation is called diffused radiation, and a part reaching directly to the surface without any scattering is termed as direct or beam radiation. Some of the parts of direct beam after reaching the Earth's surface got reflected, whereas some part gets absorbed; reflected part is termed as albedo. Total of the direct radiation and diffused radiation is called global radiation. Amount of radiation reaching the ground is variable in nature and depends upon the climatic like clouds and geographical situations. One of the characterizations of the clear atmosphere on sun light is air mass 'AM', which is equivalent to the relative length of the direct beam path through the atmosphere. On a clear day in summer at sea level radiation from the sun at zenith corresponds to air mass 1 (AM1), and at other angles it is approximately equal to the reciprocal of the cosine of zenith angle θ_z. Spectrum of the extra-terrestrial radiation is represented by AM0 and is important for satellite applications of solar cells. AM1.5 is a typical solar spectrum on the Earth's surface on a clear day which, with total irradiance of 1kW/m^2, is used for the calibration of solar cells and modules. Available irradiance is usually less than the global irradiance value 1kW/m^2 because of earth rotation and climatic conditions.

For the design purpose of a photovoltaic system, solar irradiation or solar insolation is an important factor and is equal to total solar irradiance over a time interval. Daily solar irradiation is obtained by calculating total solar irradiance over 24 our duration (One day). As the solar irradiance observed on the surface of the earth is 30% of the incident one because of scattering and reflection, thus average daily solar radiation on the Earth's surface G_{av} is equal to 5.75kW·h/day (0.7×342×24h). This value is used as a standard value of average daily irradiation for the comparison with average irradiation to other places on the Earth's surface.

Figure.7.1.2 shows the instruments used for the measurement of solar radiation. Pyranometer is used to measure global radiation, whereas pyranometer with shadow band measures only diffused radiation. Beam radiation is measured with the help of pyrheliometer and sun shine hours are measured with the help of sunshine recorder.

(a) (b) (c) (d)

Fig.7.1.2. Solar radiation measuring instruments: a) pyranometer, b) pyranometer with shadow band, c) pyrhelometer, d) sunshine recorder.

7.1.2 Basics of Photovoltaic

7.1.2.1 Principle of operation

Solar power can be utilized in two ways, first by collecting the radiant heat and using it in a thermal system, which is called solar thermal system, and the second is by directly converting solar energy into electrical energy by photovoltaic. Feasible solution of the use of solar energy for automotive application is photovoltaic.

Photovoltaic is the process of energy conversion in which solid state material is used for the direct conversion of solar energy into electrical energy and is similar to the theory of photo-electric effect, as per which when a photon of sufficient energy falls on material of lower work-function, for example solid state materials, electrons from valance band jumps to conduction band due to sufficient gain in energy. Photovoltaic is a bit different from photo electric effect in the sense that in this case electrons do not eject out from the material. In case of semiconductor materials, light of relatively low energy like visible photon can shift electrons to conduction band. When the electrical path is completed with the semiconductor material, electric current in the electrical circuit is observed.

7.1.2.2 Solar Cell

Fundamental unit of solid state material used for the energy conversion in photovoltaic (PV) system is called solar cell or PV cell. Solar cell is basically a current source driven by the flux of solar radiation. A crystalline solar cell can generate approximately $35mA/cm^2$ current at a voltage of 550mV with a solar radiation of $1kW/m^2$. Commercial PV cells have efficiency in the range of 10-20% and produces $1\text{-}2kWh/m^2$ in a day. Next higher energy conversion unit of PV system is PV module where solar cells are connected together in series to achieve higher voltage rating. Larger number of PV modules can be connected in parallel and series to increase current and voltage ratings of the system. This arrangement of PV modules is called a PV array.

7.1.2.3 Classification of solar cells

Solar cells can be classified on the basis of its physical structure, like thickness and type of the active material used for its fabrication. As per the thickness of the active material, solar cells are classified as bulk material solar cell and thin film solar cell. In bulk material solar cells, base material itself is an active material whereas in thin film solar cell active material is deposited on a support known as substrate.

As per the type of the active material used for the fabrication, solar cells are classified as

- Mono-crystalline silicon cell
- Poly-crystalline silicon cell

- Amorphous silicon: a-Si cell (*Inorganic thin film*)
- CIGS Copper Indium diselenide cells ($CuInSe_2$) with Galium (*Inorganic thin film*)
- Organic PV cell (*Plastic solar cells*)
- Organic-inorganic PV cell (*Dye-sensitized solar cells* DSSCs)

Crystalline silicon cells possess higher conversion efficiency but are costly compared to cells of other type. A-Si, CIGS, plastic solar cells and DSSCs comes in the category of flexible cells. Thermal coefficient for power of these cells are lower compared to crystalline Si cells (0.5%/°C). Thermal coefficient for a-Si cell is 0.21% per °C. It means that at a normal cell temperature of 60° C, the relative power output of a crystalline module will reduced by approximately 17% from the standard test condition rating, whereas for a-Si cells output is reduced by about 4-6%. Thus a-Si cells have higher power output at normal than at higher cell temperature. CIGS are approaching efficiency of 20.3% of silicon based rigid cells (crystalline cells) and the conversion efficiency is very stable over time. These cells are purely self-repairing as some of the chemical bonds break easily and free the copper atoms to wander through the crystals to distribute themselves naturally in even. By this way their presence fixes the problem. DSSCs work well over a wide range of lighting conditions and orientation, as they are less sensitive to partial shadowing and low-level illumination [2]. Comparison of crystalline and thin film PV cells in terms of efficiency and cost is listed in *Table 7.1.1*.

Tab.7.1.1: Comparison of solar cells in terms of cost and efficiency

	Bulk type/ Wafer-based (Crystalline)			
	Mono-crystalline Si	Ploy-crystalline Si		Poly-crystalline
Pros	→ High efficiency	→ High efficiency with respect to price		-
Cons	→ Increased manufacturing cost caused by the supply shortage silicon			-
	Thin-film type			
	Amorphous Si	CIGS	CdTe (Cadmium telluride)	Polymer organic
Pros	→ Low price	→ Low price → Able to automate all manufacturing process		→ Low manufacturing → Can be more efficient (still in research)
Cons	→ Low efficiency	→ Low efficiency		

7.1.3 Characteristics of PV modules

Electrical characteristics of a solar cell are defined by the output-current vs terminal voltage (I~V) and output-power vs voltage (P~V) curves. Amount of electrical current generated by the solar cell due to excitation by light at a given temperature depends upon; a) intensity of the light (solar irradiance) falling on the cell surface and b) wavelength of

the incident rays. Figures 7.1.3a and 7.1.3b shows I-V and P-V curves for a solar module under different solar irradiance level.

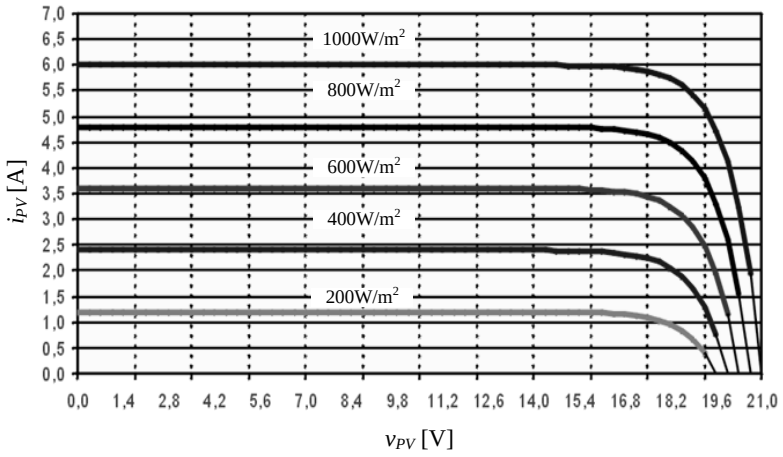

Fig.7.1.3. Output current vs voltage (I-V) characteristics curves for a photovoltaic module for different solar irradiances (image resources: www.pvresources.com)

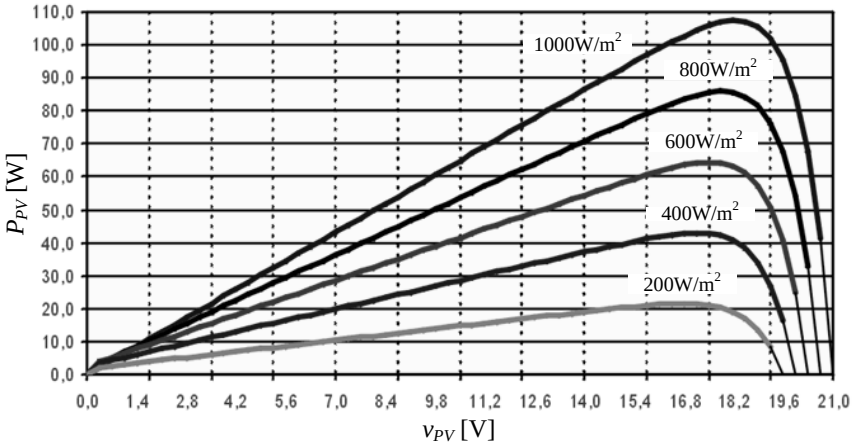

Fig.7.1.4. Output power vs voltage (P-V) characteristics curves for a photovoltaic module for different solar irradiances (image resources: www.pvresources.com)

It is clear that, there is wide variation in the current produced by the solar module in comparison of terminal voltage with solar irradiance. Corresponding to each of the curve there is a point where cell/module generates maximum power, this point is called maximum power point; it is always desirable to operate the cell/module at this point to extract maximum power from the module.

7.1.3.1 Technical specifications of a solar cell/module as per data sheet

For the utilization purpose of the PV modules there are some specification which are required and necessarily mentioned by the manufacturers in their data sheet. These are generally termed as rating at STC (Standard test condition) or SRC (Standard Reporting Conditions). STC/SRC is considered as, nominal cell temperature 25°C, nominal irradiance level 1000W/m^2, at spectral distribution of AM1.5. STC is developed by UL (Underwriters Laboratories) [3]. Electrical Parameters generally found in a data sheet are enlisted in *Table 7.1.2.*

Tab. 7.1.2: Electrical parameters of a photovoltaic module provided by manufacturers	
• Peak Power (W_p)	• Fill factor (FF)
• Power Tolerance (%)	• Module efficiency (η)
• Open circuit voltage (V_{oc})	• Temperature coefficient V_{oc}
• Short circuit current (I_{sc})	• Temperature coefficient I_{sc}
• Voltage at maximum power (V_{mp})	• Temperature coefficient power
• Current at maximum power (I_{mp})	• NOCT (Nominal operating cell temperature)
• Maximum System voltage (V_{dc})	

Module ratings are also required to be mentioned at NOCT, which is defined as the equilibrium cell junction temperature corresponding to an open-circuit module operating in a reference environment of 800W/m^2 irradiance, 20°C ambient air temperature with a 1m/s wind across the module from side to side. Other information which a data sheet includes, are mechanical characteristics, cell information, absolute maximum ratings. Mechanical characteristics includes, physical dimension of the module, type of enclosures, weight etc. Cell information includes information about the cell type, Cell size, number of cells etc. Absolute maximum ratings includes information about application, fire resistance class, maximum over current rating, operating temperature (°C), storage temperature (°C), maximum load capacity (Kg/m^2), maximum wind resistance (km/h) and maximum *Hai* diameter@80km/h.

7.1.3.2 Electrical Equivalent circuit model of a PV cell

PV cell can be modelled as a current source in parallel with a diode. In case of non-availability of light, PV cell behaves as diode, and as light intensity increases, it starts generating current.

Various electrical models such as, Anderson's method [4], Bleasser's method [5], IEC-891 procedure [6], semiconductor model [7], two-exponential model [8], F. Z. Peng's method [9] etc, have been proposed to explain the energy conversion method of a PV cell. Out of these methods, Anderson, Bleasser and IEC 891 methods work on point by point principle, whereas semiconductor model, two exponential model, and Peng's method are based on analytical models. Except Peng's method, all other mentioned methods require some data which are not available in data sheet. Circuit model with two diodes [10] is considered to be more accurate one. *Figure 7.1.5* shows the simplified equivalent circuit model for a PV cell as per the solar cell semiconductor model [7].

Total current I_{PV} for the circuit shown in the *Figure 7.1.5* in terms of circuit parameters is given by (7.1.1), [7].

$$I_{PV} = I_G - I_0\left[e^{\frac{q\left(V_{PV} + I_{PV}R_S\right)}{nkT}} - 1\right] - \frac{V_{PV} + I_{PV}R_S}{R_{SH}} \qquad (7.1.1)$$

where, I_G is the generated current, I_0 is the saturation current of the diode, q is the elementary charge (1.6×10^{-19} Coulomb), k is the Boltzmann constant (1.38×10^{-23}J/K), T is the cell temperature in Kelvin, V is the measured cell voltage or applied voltage for the purpose of voltage biasing, R_S and R_{SH} are the series and shunt resistance of the equivalent electrical model and are equal to the inverse of the slope of the I-V curve at V_{oc} and I_{sc} respectively.

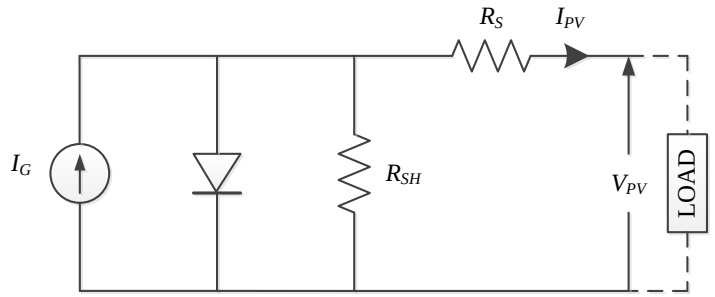

Fig. 7.1.5 Simplified Equivalent circuit model for a PV Cell

7.1.3.3 Definitions associated with the electrical characteristics of a PV cell

Various parameters defined with the help of (7.1.1) and the characteristic curves are:

a) Short circuit current I_{SC}: Short circuit current corresponds to the current from the solar cell when the load impedance is zero and the output terminal voltage is equal to zero as shown in *Figure 7.1.6a*. I_{SC} is the maximum value of the current in power quadrant. For an ideal cell it is equal to the maximum current generated by the solar cell.

b) Open circuit voltage V_{OC}: Open circuit voltage V_{OC} is the measured cell voltage when no current is delivered by the cell. V_{OC} is also equal to maximum potential difference across the cell for a forward-bias sweep in the power quadrant.

c) Peak power or Maximum power W_P: Peak power produced by the solar cell is equal to the maximum rectangular area sweep by I-V curve as shown by the shaded area in *Figure 7.1.6a*. At the point of open circuit voltage and short circuit current of the cell power generated by the cell is equal to zero and in between these two points it rises to a peak value from zero and then again reduces to zero as shown in *Figure 7.1.6b*. This peak point is called maximum power point (MPP) and is the operating point, where the maximum power from the solar cell can be extracted. Current and voltage corresponding to the MPPs are termed as I_{mp} (current at peak power point) and V_{mp} (voltage at peak power point) respectively.

d) Fill factor *FF*: Fill factor is the measure of closeness of the practical I-V curve with the ideal one. It is equal the ratio of maximum/peak power of the solar cell to total theoretical power W_{Th} (product of V_{OC} and I_{SC}). It can also be defined as the ratio of maximum area sweep by I-V curve to area formed by the V_{OC} and I_{SC} as shown in *Figure 7.1.6c*. Value of the *FF* ranges from 0.5 to 0.82. Mathematically fill factor is given by (7.1.2)

$$FF = \frac{W_p}{W_T} = \frac{V_{mp} I_{mp}}{V_{OC} I_{SC}} \qquad (7.1.2)$$

e) Efficiency η: Efficiency of a PV cell of module is defined by the ratio of the electrical power output W_{out} to solar power input W_{in}. Input power is calculated by the product of solar irradiance in (W/m^2) with the cell area in m^2. For the calculation of maximum efficiency solar irradiance is considered as 1000W/m^2.

$$\eta = \frac{W_{out}}{W_{input_{solarpower}}} \qquad (7.1.3)$$

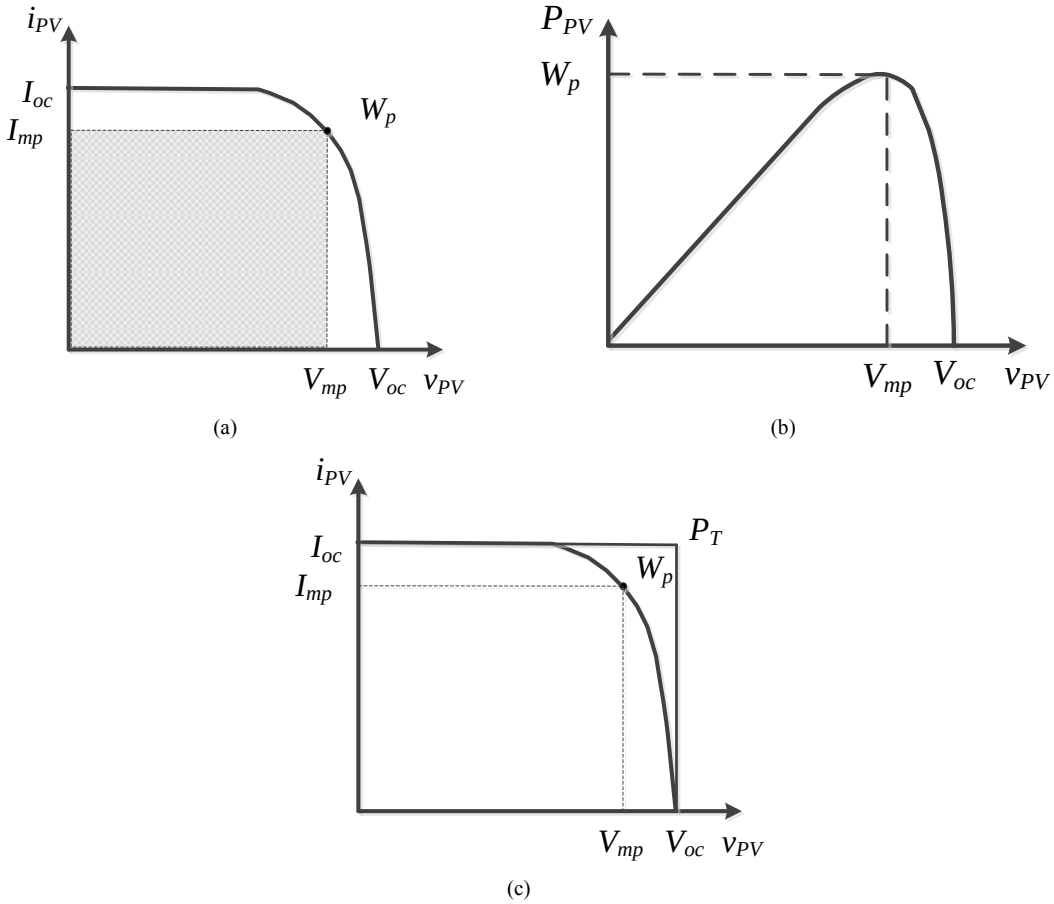

Fig. 7.1.6. a) I-V curve; b) P-V curve; c) I-V curve for the explanation of fill factor

7.1.3.4 Effect of variation of solar irradiance and cell temperature

Figure 7.1.7 shows the variation in PV cell current, voltage and power due to the variation in irradiance and cell temperature. With the increase in irradiance, movement of free electrons in conduction band is considerably higher in comparison with the thermally generated free electrons. Therefore much higher variation in the cell current is observed in case of variation in irradiance, *Figure 7.1.7a*, compared to variation in temperature, *Figure 7.1.7b*. Negative voltage thermal coefficient, result in noticeable drops in the open circuit voltage with the increase in temperature, as it is shown in *Figure 7.1.7b*. Variation in the current due to temperature is generally neglected because of much lower positive thermal coefficient.

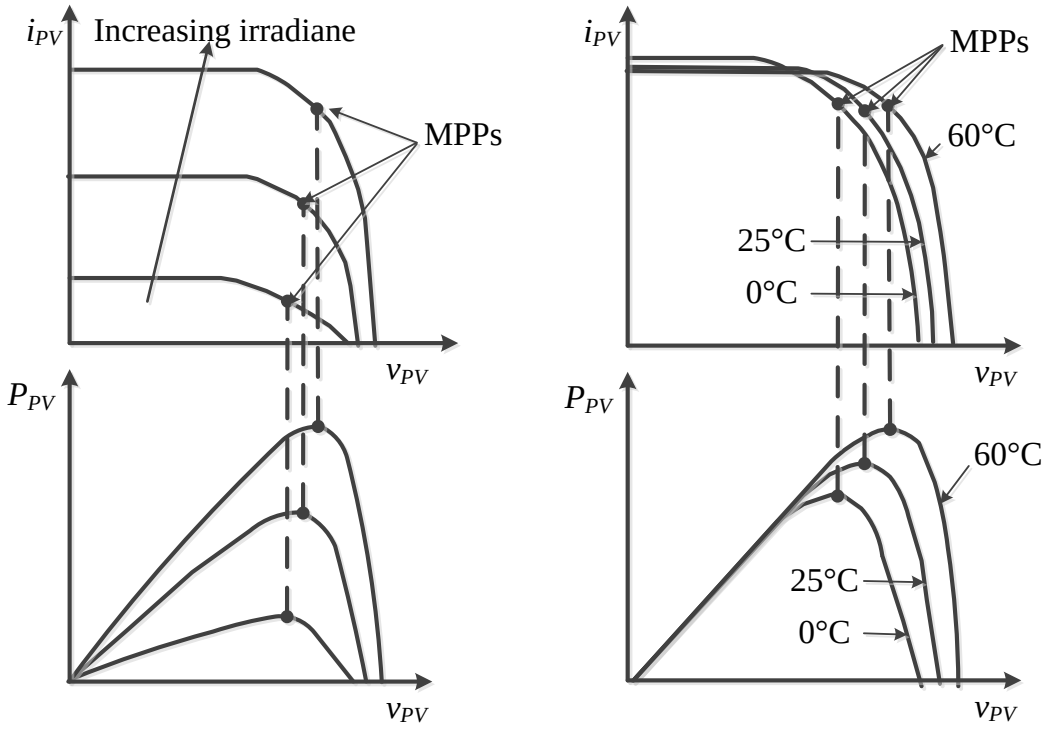

(a) (b)

Fig.7.1.7. Variation in current and voltage of a PV cell due to variation in a) irradiance; b) cell temperature, variation in output power due to variation in c) irradiance; d) cell temperature

Three different types of thermal coefficients for a solar cell are:

- short circuit thermal coefficient, expressed as percentage change in short circuit current with unit change in temperature and is represented as $\%I_{SC}$/°C.
- open circuit voltage thermal coefficient, expressed as percentage change in open circuit voltage due to unit change in temperature and is represented as $\%V_{OC}$/°C.
- nominal power thermal coefficient, expressed as percentage change in nominal power with unit change in temperature and is expressed as %W/°C.

In general, values of the thermal coefficients of open circuit voltage and nominal power thermal are negative and that of short circuit current is positive and negligible compared to two thermal coefficients.

7.1.3.5 Effect of variation in RS and RSH

As shown in *Figures 7.1.8a* and *7.1.8b*, variations in the series and shunt resistances affect the shape of I-V curve. With the increase in these parameters peak power shifts to lower value and hence the fill factor reduces due decrease in maximum area sweep by I-V curve.

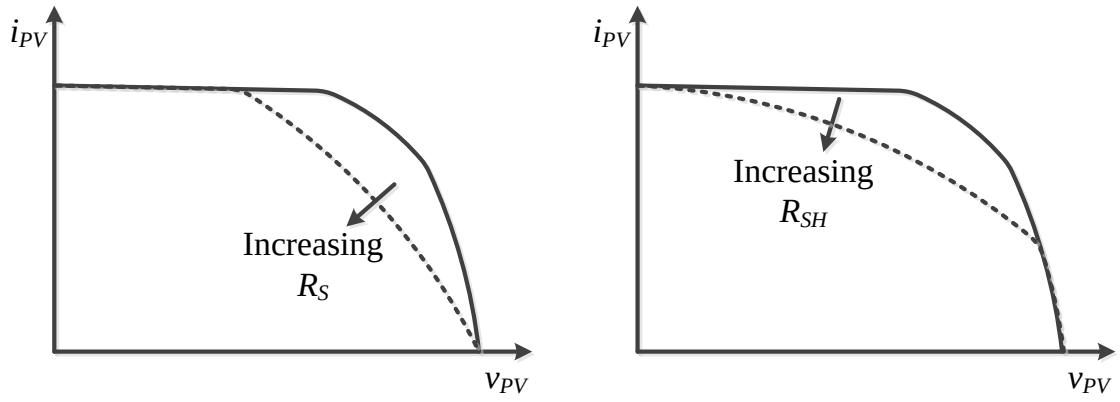

(a) (b)

Fig. 7.1.8. Variation in the shape of I-V characteristic curve due to variation in a) series resistance R_S; b) variation in shunt resistance R_{SH}

7.1.4 Solar irradiance available in Padova

JRC (Joint Research Centre) of European Commission provides information of daily and monthly irradiation for different places of Europe by using PVGIS (Photovoltaic Geographical Information System) and CM-SAF-PVGIS (Satellite Application Facility on Climate Monitoring PVGIS) data base system [11]. For the determination of irradiance in different places two methods have been adopted:

- ground measurements of solar radiation and
- solar radiation estimates from satellite.

The PVGIS database available for Europe is based on an interpolation of ground station measurements. The ground station measurement data are long-term monthly average of global and diffuse irradiation on a horizontal plane. These data were originally part of the European Solar Radiation Atlas from 1981 to 1990. CM-SAF-PVGIS database for Europe are based on calculation from satellite images performed by CM-SAF and is taken over for 12 years of duration. Data from 1998 to to 2005 are from the first generation of Meteosat satellites knows as (MFG) and from June 2006 to May 2010 data is obtained from second generation Meteosat satellite known as (MSG).

Figure 7.1.9a shows the distribution of yearly sum of global irradiation on a horizontal surface in kWh/m^2 and potential solar electricity map kWh/kW$_p$ generated by a 1kW$_P$ system per year with photo-voltaic modules mounted on a horizontal surface, assuming system performance ratio of 0.75. Distribution is averaged over ten year duration from 1981 to 1990. *Figure 7.9b* shows the irradiance distribution for optimally inclined surface. From the map we can say that global irradiation at Padova on horizontal surface is around 1400 kWh/m^2 and for optimally inclined surface is in between 1550 to 1600 kWh/m^2. PVGIS database provides estimation of the performance of grid connected photo-voltaic system to be installed in any of the place in Europe.

In case of electric vehicles (say an electric mini-car) it is a costlier affair to maintain inclination of photo-voltaic module to optimal angle of inclination in due south-east direction, to acquire maximum possible irradiance. Roof top of a vehicle is a best place to mount a module, as most of the time it remains parallel to the horizontal surface. Thus information

provided by PVGIS/CM-SAF database can also be used for the electric vehicles.

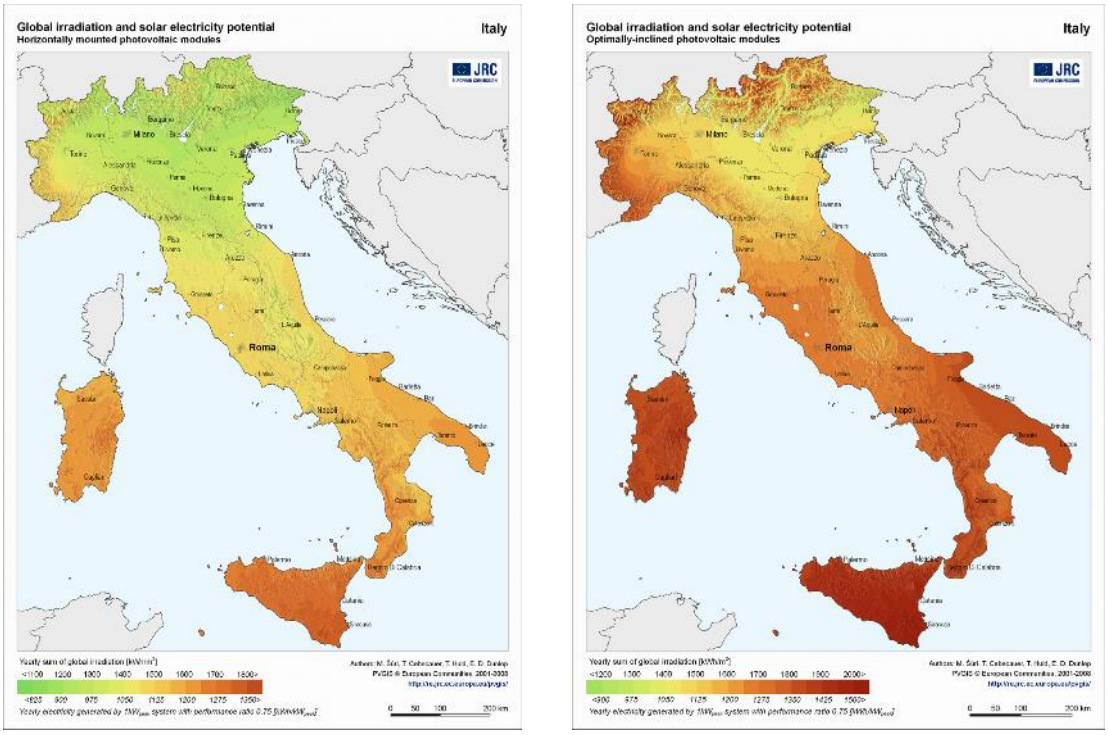

(a) (b)

Fig.6.1.9. Global irradiation and potential electricity map for: a) horizontally mounted photo-voltaic modules; b) optimal angle mounted photo-voltaic module.

Table 7.1.3 shows the global irradiation on horizontal surface at Padova as provided by PVGIS and PVGIS CM-SAF database respectively. Difference in the irradiation measured by CM-SAF and PVGIS is may be due to climatic changes as PVGIS is based on ground measurement data during 1981-1990, error due to distinction between snow and clouds and other factors specified by JRC. *Figures 7.1.10a* and *7.1.10b* shows the graphical variation in global irradiation at Padova.

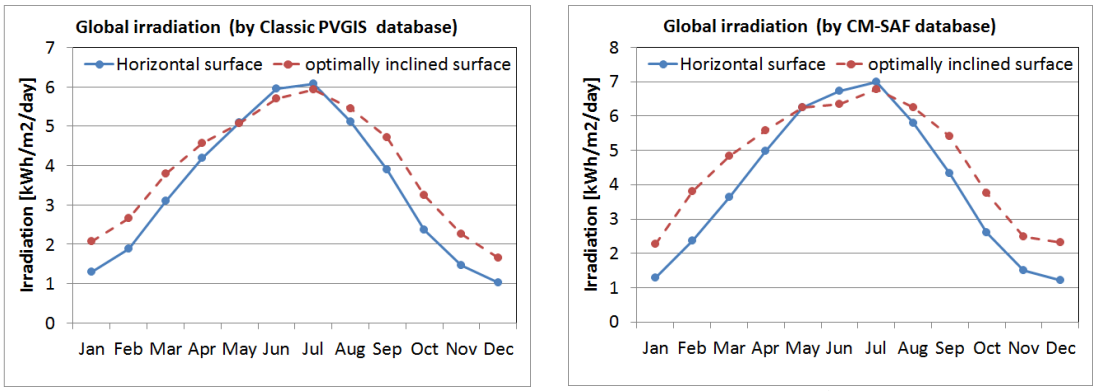

(a) (b)

Fig.7.1.10. Global irradiation on horizontal surface and optimally inclined surface at Padova estimated by: a) Classic PVGIS database and b) CM-SAF database.

Tab.7.1.3: Monthly incident global irradiation *H* at Padova, Italy					
Month	Classic PVGIS database		CM-SAF PVGIS database		Average day time temperature
	H_h (kWh/m^2/day)	H_{opt} (kWh/m^2/day)	H_h (kWh/m^2/day)	H_{opt} (kWh/m^2/day)	T_D (°C)
Jan	1.29	2.08	1.30	2.28	4.6
Feb	1.89	2.65	2.38	3.81	6.4
Mar	3.09	3.80	3.64	4.83	10.4
Apr	4.18	4.56	4.97	5.57	13.9
May	5.10	5.07	6.26	6.25	19.3
Jun	5.95	5.69	6.72	6.34	23.2
Jul	6.07	5.93	6.99	6.78	25.2
Aug	5.12	5.44	5.80	6.25	24.9
Sep	3.89	4.71	4.34	5.41	20.7
Oct	2.37	3.24	2.61	3.76	16.2
Nov	1.46	2.27	1.51	2.50	10.3
Dec	1.03	1.65	1.23	2.33	5.9
Yearly average	3.46	3.93	3.99	4.68	15.1

H_h : Irradiation on horizontal surface; H_{opt} : Irradiation on optimally inclined surface; Optimal angle of inclination: 34° (source PVGIS database system)

From the *Table 7.1.3* it is clear that irradiation is minimum in the month of December and maximum in the month of July. Therefore, for the present case both global and diffused daily irradiance during clear and real sky at Padova for two extreme cases, i.e. for the month of July and December are considered. Variations in irradiation during two months are plotted in *Figure 7.1.11*.

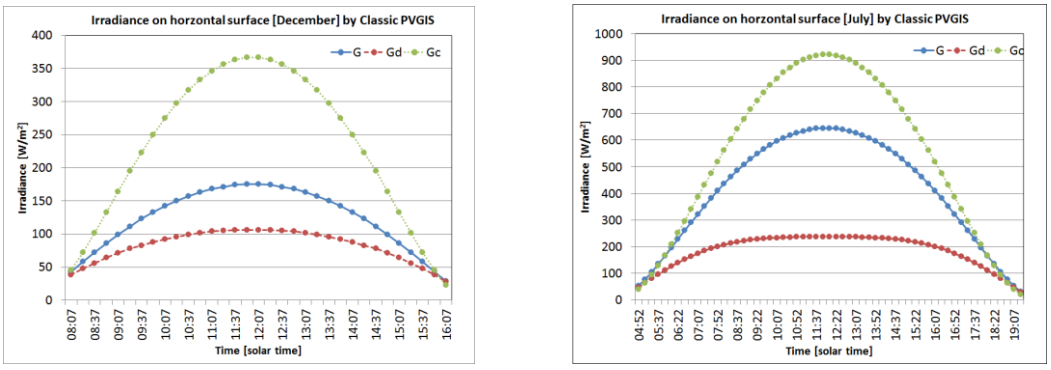

(a) (b)

Fig.7.1.11. Daily irradiance at Padova estimated by Classic PVGIS database in the month of: a) December; b) July. (G: Global; Gd: diffused; Gc: Clear sky)

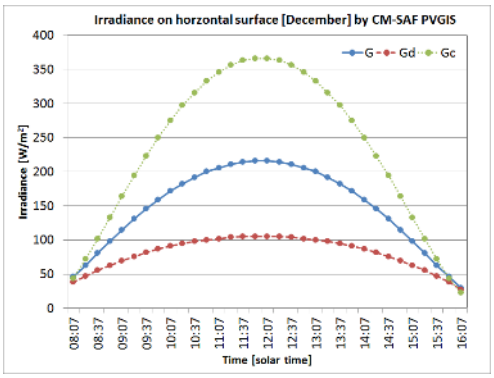

(c)

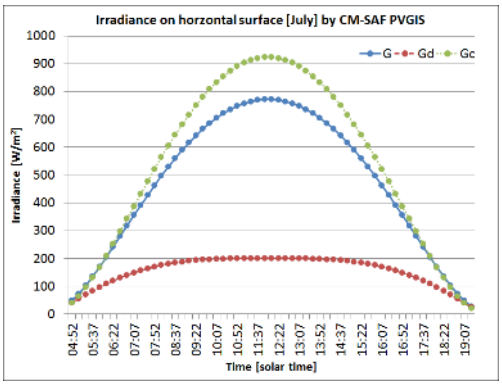

(d)

Fig.7.1.11. Daily irradiance (global and diffuse) at Padova estimated by PVGIS CM-SAF database in the month of: c) December; d) July. (G: Global; Gd: diffused; Gc: Clear sky)

Estimated peak and minimum value of the global during real sky, diffuse during real sky and global during clear sky for Padova in the month of December and July are listed in *Table 7.1.4*. It provides important information for the decision of calculation of minimum and maximum solar input to a photo-voltaic module mounted on a horizontal surface.

Tab. 7.1.4: Estimated solar irradiance on a horizontal surface

	Solar irradiance estimated by classic PVGIS (December)				Solar irradiance estimated by classic PVGIS (July)			
	Time	G	Gd	Gc	Time	G	Gd	Gc
	08:07	43	38	45	04:52	52	47	39
Peak	11:52-12:07	175	107	367	11:52-12:07	645	237	921
Minimum	16:07	28	28	16	19:22	29	29	18
	Solar irradiance estimated by CM-SAF PVGIS (December)				Solar irradiance estimated by CM-SAF PVGIS (July)			
	08:07	43	34	45	04:52	48	40	39
Peak	11:52-12:07	212	96	367	11:52-12:07	771	198	923
Minimum	16:07	25	25	16	16:07	25	25	18

G: Global irradiance on horizontal plane (W/m^2); Gd: diffused irradiance on horizontal plane (W/m^2); Gc: Global irradiance on horizontal plane during clear sky (W/m^2)

From the *Table 7.1.4* it is clear that there is not much difference in the data estimated by the two measurement system used by JRC. So we can use CM-SAF PVGIS data base for the estimation of possible power out from a photovoltaic module.

7.1.5 Calculation of input and output power of a PV module mounted on a electric mini-car

7.1.5.1 Calculation of solar energy input to a PV module mounted on a mini electric car

For the case study, Electric mini-car, Birò Estrima is considered. Roof area of this car is 750×880 mm^2 (0.66 m^2). Available roof area when multiplied with the estimated solar irradiance for Padova results in total input solar power. Input power varies from 242 W in the month of December, to 609W peak in the month of July for clear sky. Whereas it varies from 140 W to 508W peak with real sky from December to July respectively. Minimum solar power input is equal to 16.5W and 11-12 W for real sky and clear sky respectively for both the extreme months. Therefore we can consider that solar power input to the photo-voltaic module mounted on the roof of the car with the available space is minimum 11W and maximum 609W (=923W/m^2×0.66 m^2).

Output power of the photo-voltaic module is calculated by multiplying the input power with the efficiency of the module specified by the manufacturer. One of the most important constraints with the present application is availability of space to mount the photo-voltaic module on the roof top of the car.

7.1.5.2 Calculation of electrical power output from a PV module mounted on the mini car

Case 1: Crystalline photo-voltaic module from Enecom, Italia

Considering the datasheet of HF-40

Physical dimension of this module is 670×526×1.5 (0.352m^2, horizontal area). Thus the maximum input solar power is 324.896W and minimum solar input power is 5.632W. Therefore possible output power for module with: a) crystalline cell (18% conversion efficiency) will be in between 1.014W to 58.48W; b) poly crystalline cell (16% conversion efficiency) will be in between 0.901W to 51.98W.

Other parameters of the module at STC (Standard test conditions) are

V_{OC}= 21.96V; I_{SC} = 2.4A; I_{mp}=2.16A; V_{mp}= 18.18V; Number of Cells in series = 36; Cell dimension = 62.5×125 mm^2.

As the estimated extreme irradiations are 923W/m^2 and 16W/m^2 so I_{SC} for two cases are (2.4×923/1000) ≈ 2.22A and 0.04A. Since current is negligible affected by the variation in temperature due to smaller thermal coefficient, effect of variation in temperature is neglected.

For crystalline solar cells, thermal coefficients for open circuit voltage and peak power are -125.8mV/°C and -0.45%/°C respectively. Average day time temperature at Padova in the month of July is around 25°C and in the month of December is 5°C. As the in the month of July temperature is equal to standard value, open circuit voltage for July will remain same and is 21.96V. Open circuit voltage in the month of December will be 77.21V.

Peak power in the month of July will also remain approximately same, i.e. 58.48W for mono crystalline and 51.98W for poly crystalline solar module, due to same temperature. But in the month of December, it will be 10.14W and 9.01W for mono crystalline and poly crystalline photo-voltaic module respectively.

Formula used for the calculation of voltage and power at different temperature are given by (7.1.4) and (7.1.5) for voltage and power respectively

$$V_t = V_0(1+\beta\Delta T) \qquad (7.1.4)$$

$$P_t = P_0(1+\gamma\Delta T) \qquad (7.1.5)$$

where V_t and P_t are the voltage and power respectively at any temperature, V_0 and P_0 are voltage and power at STC and β and γ are thermal coefficients for open circuit voltage and peak power as described earlier.

Case 2: Poly crystalline Silfab module with 20 cells

Effective cross sectional area of the PV module is 20×0.156^2 and is equal to $0.48672m^2$. Parameters of this module at STC are:

V_{OC} = 12.48V; I_{SC}= 8.305A; V_{mp}= 10.46V; I_{mp}= 8.305A; P_{max} = 80.17W; η = 16.8%. Temperature coefficients are: -2.23mV/K (voltage); +3.69mA/K (current) and -0.046 %/K (power).

Input and output power to and from the PV module, as per the available irradiance during real and clear skies are tabulated in *Table 7.1.5*.

Tab.7.1.5: Estimated solar irradiance on a horizontal surface and power output of SilFab module

Climatic condition	Extreme months	Estimated global irradiance on horizontal plane (Wm^{-2})		Input power (W)		Output power @ η =16.8% (W)	
		max	min	max	min	max	min
Clear sky	July	923	18	449.24	8.76	75.47	1.47
	December	367	16	178.63	7.79	30.01	1.31
Real sky	July	717	25	375.26	12.17	63.04	4.2
	December	212	25	103.18	12.17	17.33	4.2
I_{SC}	8.305A at STP	923	16			7.67A	133mA

Extreme irradiances available are 16 and 923 W/m^2 and the corresponding output powers are 1.31W and 75.47 W. Short circuit current for the two cases are 133mA and 7.67A (=8.305×923/1000). As the temperature coefficient for the current is very small, variation in current with temperature can be neglected.

For the considered solar cells, thermal coefficients for open circuit voltage and peak power are -2.23mV/°K and -0.046%/°K respectively. Average day time temperature at Padova in the month of July is around 25°C. As the in the month of July temperature is equal to standard value, open circuit voltage for July will remain same. i.e.12.48V. Consider that in the month of December temperature fall down to -10°C (*worst case*), in this case open

circuit voltage will be equal to 13.45V.

Peak power in the month of July will also remain approximately same, i.e. 75.47W and in the month of December, it will be 3.42W.

Other possible modules which can be used on the roof of the car are HF-70 (Peak power at STC 70W, with cross-sectional area 1104×526), HF-80 (Peak power at STC 80W, with cross-section area 1230×526 mm^2) from Enecom, Italia, BP 365 (Peak power at STC 65W, with cross-sectional area 1111×502 mm^2) of BP Solar and 75W, 20 Cell SilFab module with cell cross-sectional area 156×156 mm^2.

7.2 Interfacing of PV module with DC-link through high gain dc-to-dc boost converter

7.2.1 Calculations of output voltage and current from PV module

Specification of the multi crystalline SiLFab PV module to be used for the mini-car are summarised in *Table 7.2.1*

Tab. 7.2.1: Specifications of photovoltaic module		
Number of cells: 20	Unit cell area: (0.156x0.156) m^2	Module efficiency: 16.8%
Voltage	V_{OC} = 12.43V	V_{mp} = 9.479V
Current	I_{SC} = 8.44A	I_{mp} = 7.92A
Temperature coefficients	$I_{SC}(\alpha)$: 0.06%/K; VOC(β): -0.31%/K; Pmax(γ): -0.41%/K	
Operating temperature	-40°C to +85°C	

Input and output power to and from the PV module, as per the available irradiance during real and clear skies are tabulated in *Table 7.2.2*.

Tab. 7.2.2: Estimated solar irradiance on a horizontal surface and power output of sil-fab module							
Climatic condition	Extreme months	Estimated global irradiance on horizontal plane (W/m^2)		Input power (W)		Output power @ η =16.8% (W)	
		max	min	max	min	max	min
Clear sky	July	923	18	449.24	8.76	75.47	1.47
	December	367	16	178.63	7.79	30.01	1.31
Real sky	July	717	25	375.26	12.17	63.04	4.2
	December	212	25	103.18	12.17	17.33	4.2

Extreme irradiances available are 16 and 923 W/m^2 and the corresponding output powers are 1.31W and 75.47 W. Short circuit current for the two cases are 135mA and 7.79A (= 8.305×923/1000). As the temperature coefficient for the current is very small variation in

current with temperature can be neglected. For the considered solar cells, thermal coefficients for open circuit voltage and peak power are -0.31%/°K and -0.41%/°K respectively. Average day time temperature at Padova, Italy in the month of July is around 25°C. As in the month of July temperature is equal to standard value, open circuit voltage for July will remain same. i.e.12.48V. Consider that in the month of December temperature fall down to -10°C (*worst case*), in this case open circuit voltage will be equal to 13.45V. Peak power in the month of July will also remain approximately same, i.e. 75.47W and in the month of December, it will be 1.5W.

7.2.2 Decision of input specifications for the boost converter

Figure 7.2.1 shows the I-V and P-V characteristics of SilFab 20 cell PV module. Maximum short circuit current possible in Padova for 923W/m^2 is 7.79A. *Figure 6.2.1b* shows that the open circuit voltage is widely affected by the variation in temperature. Voltage at maximum power point varies from around 7.5V to 13.5V for insolation of 100W/m^2 at 40°C to 0°C respectively. From the behaviour of PV characteristics at 100Wm^{-2} at 0° it can be predicted that voltage at maximum power point for worse case temperature (-10°C) would be around 14V. So input voltage variation for the boost converter is considered as from 7.5V to 15V. Variation of input current is considered from 0.8A to from 8.44A. Output power of the module varies in between minimum 4.2W to maximum 75.47W under different solar insolation.

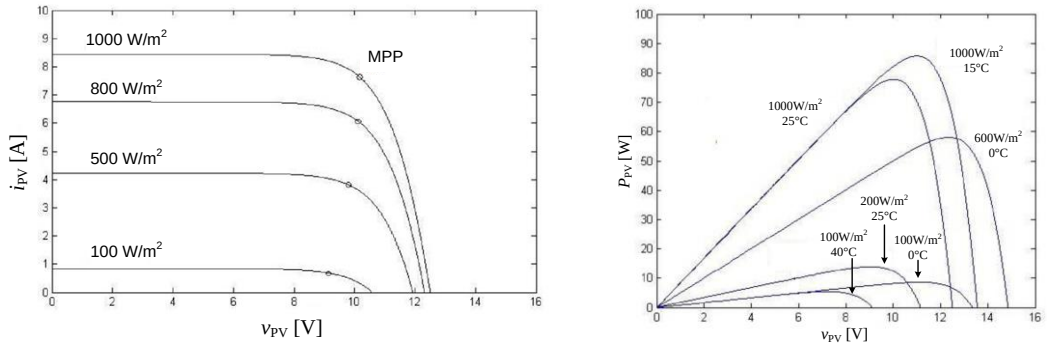

(a) (b)

Fig. 6.2.1 Characteristic curves of SilFab photovoltaic module: a) IV curve; b) PV curve for different insolation and temperature.

Variation in the input power as per insolation

$$P_{i,\min} \le P_i \le P_{i,\max} \Rightarrow 8W \le P_i \le 75.47W$$

Variation in input current as per insolation

$$I_{i,\min} \le I_i \le I_{i,\max} \Rightarrow 0.844A \le I_i \le 8.44A$$

Variation in input voltage as per insolation

$$V_{i,\min} \le V_i \le V_{i,\max} \Rightarrow 7.0V \le v_i \le 16V$$

7.2.3 Design of high gain boost converter

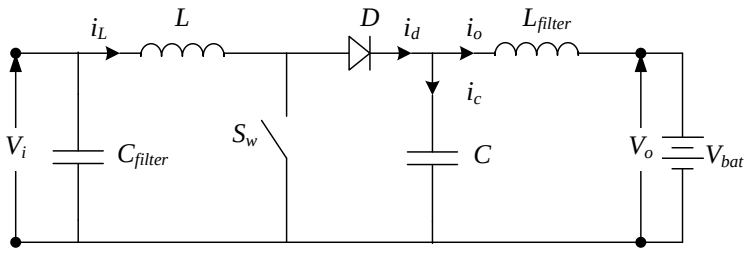

Fig.7.2.2. DC-to-DC boost converter for charging battery through PV module.

Figure 7.2.2 shows the circuital arrangement of a dc-to-dc boost converter used for the integration of SilFab PV module with the dc-bus of the mini-electric car. Boost converter is required to track the maximum power point (MPP) of the PV module and submit charge to batteries connected to the DC-bus. Boost converter is connected with the DC-bus through a filter inductor L_{filter}, so as to reduce the battery current ripples. Filter capacitor C_{filter} at the input side is used to reduce the current ripple in the PV module, which is forced to follow the current ripple of the inductor L in the absence of filter capacitor. Following specifications are considered:

Operating frequency f_s : 20*k*Hz
Nominal input power $P_{i,nom}$: 42W (average of $P_{i,min}$ and $P_{i,max}$)
Nominal input current $I_{i,nom}$: 4.6A (average of $i_{i,min}$ and $i_{i,max}$)
Nominal input voltage $V_{i,nom}$: 9V ($P_{i,nom}/I_{i,nom}$)
Nominal battery voltage $V_{B,nom}$: 48V
Maximum output voltage : 56V;
Battery current ripple: 5% of the C/10 of the nominal charging current
Ripple in PV current: less than 1%

Consider that the boost converter operates in continuous mode of operation [14]. Relationship between input and output variables are given by (7.2.1).

$$\frac{V_o}{V_i} = \frac{I_i}{I_o} = \frac{1}{1-\delta} \qquad (7.2.1)$$

where δ is the duty ratio of the boost converter and is equal to the ratio T_{ON}/T. T_{ON} is the ON duration of the switch and $T = 1/f_s$ is the period of switching operation and f_s is the switching frequency of the switch.

As per the minimum and maximum insolation available insolation output current varies from 0.143A to 1.348A.

$$I_{o,\min} \le I_o \le I_{o,\max} \Rightarrow 0.143A \le I_i \le 1.348A \qquad (7.2.2)$$

Average value of the minimum and maximum output current is equal to 0.746A and is approximately equal to the nominal output current 0.750A as per the considered specification. Maximum and minimum duty ratio required to have 56V output is calculated from

$$\left(1-\frac{V_{i,\max}}{V_o}\right) \le \delta \le \left(1-\frac{V_{i,\min}}{V_o}\right) \Rightarrow 0.732 \le \delta \le 0.875 \qquad (7.2.3)$$

For nominal values of voltage duty ratio is equal to 0.839.

7.2.3.1 Calculation of the values of the input inductor L and filter capacitor C_{filter}

Continuous conduction mode of operation of boost converter is considered. It has been considered that the current at the boundary of continuous and discontinuous mode of operation is equal to the minimum input current $I_{i,min}$, i.e. $I_{L,B}= I_{i,min}$=0.844A.

Figure 7.2.2 shows the current and voltage at the boundary of the continuous and discontinuous modes of operation. Value of inductance to ensure continuous current mode is calculated by

$$L = \frac{v_L \delta T}{2I_{i,\min}} = \frac{9 \times 0.839 \times 50 \times 10^{-6}}{2 \times 0.844} \approx 224 \mu H \qquad (7.2.3)$$

Value of L considered is 323μH.

Considering that, the input current ripple is measured with respect to the nominal current $I_{i,nom}$, then the current ripple for L =323μH is given by

$$\frac{\Delta i_L}{I_{i,nom}} = \frac{v_L \delta T}{L I_{i,nom}} = \frac{9 \times 0.839 \times 50 \times 10^{-6}}{323 \times 10^{-6} \times 4.6} \approx 0.254 (= 25.4\%) \qquad (7.2.4)$$

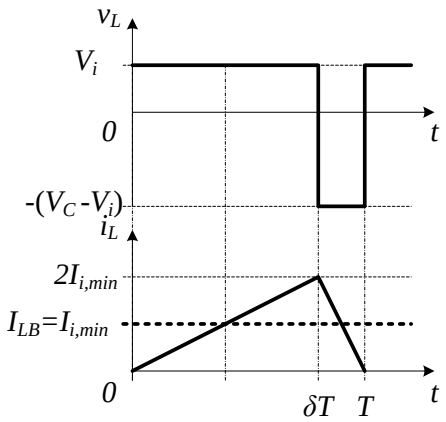

Fig.7.2.2. Inductor current and voltage at the boundary of continuous and discontinuous mode of operation

As the inductor forces current ripples into the PV, higher value of the current ripple deteriorates the performance of the PV module. A filter capacitor is connected at the input of the boost converter to filter the current ripples. *Figure 7.2.3* shows the inductor current i_L, filter capacitor current $i_{C,filter}$ and voltage across the filter capacitor $v_{C,filter}$.

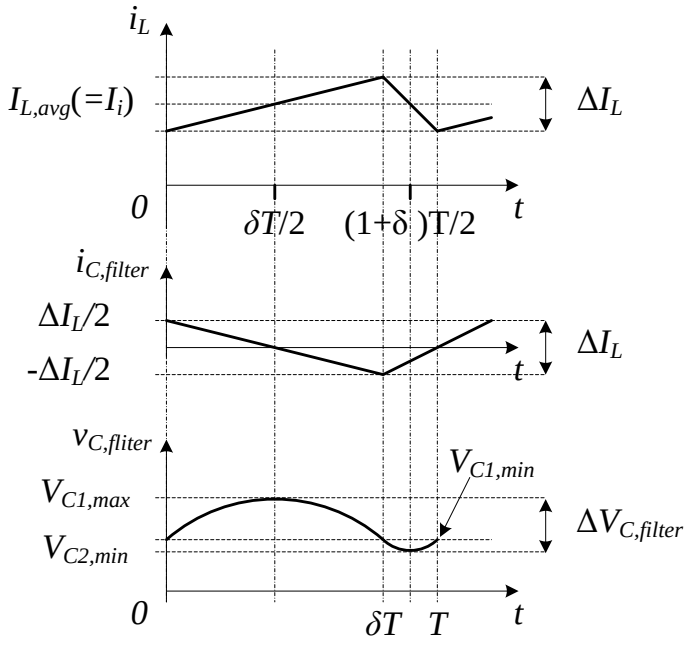

Fig.7.2.3. inductor current and filter capacitor current and voltage

For PV current to remain unaffected from the ripples in the inductor, ripple component should be absorbed by the filter capacitor. Thus $i_{C,filter}$ should follow the behaviour of inductor current ripple with negative sign i.e. $i_{C,filter} = -\Delta i_L = -(i_L - I_{L,avg})$ with average value equal to zero.

Value of the required filter capacitor can be calculated from the information of the relation between voltage ripple across the filter capacitor i.e. $\Delta V_{C,filter}$ and ΔI_L. Such a relationship is obtained as followed:

$$i_{C,\,filter} = \begin{cases} -\dfrac{\Delta I_L}{\delta T}\left(t - \dfrac{\delta T}{2}\right) & 0 \le t \le \delta T \\ \dfrac{\Delta I_L}{(1-\delta)T}\left(t - \dfrac{1+\delta}{2}T\right) & \delta T \le t \le T \end{cases} \qquad (7.2.5)$$

and the voltage across the C_{filter} is given by

$$v_{C,\,filter} = \frac{1}{C_{filter}} \int i_{C,\,filter} dt + const \qquad (7.2.6)$$

Solution of (7.2.6) with boundary conditions, at $t = 0$; $v_{C,filter} = v_{C1,\min}$ and at $t = \delta T$; $v_{C,filter} = v_{C1,min} = v_{C2,max}$ as shown in *Figure 7.2.3*, results in expression of $v_{C,filter}$ during two intervals. Suffix 1 and 2 are used to represent the expressions of the waveform during $0 \le t \le \delta T$ and $\delta T \le t \le T$ respectively.

$$v_{C,\,filter} = \begin{cases} -\dfrac{\Delta I_L}{2\delta T C_{filter}}\left(t - \dfrac{\delta T}{2}\right)^2 + \dfrac{\Delta I_L}{8C_{filter}}\delta T + V_{C1,\min} & 0 \le t \le \delta T \\ \dfrac{\Delta I_L}{2(1-\delta)TC_{filter}}\left(t - \dfrac{1+\delta}{2}T\right)^2 - \dfrac{\Delta I_L}{8C_{filter}}(1-\delta)T + V_{C1,\min} & \delta T \le t \le T \end{cases} \qquad (7.2.7)$$

Expressions in (7.2.7) represents the parabolic variations of $v_{C,filter}$ with maximum value at $t = \delta T/2$ and minimum value at $(1+\delta)T/2$. Maximum and minimum values of $v_{C,filter}$ are

$$V_{C1,\max} = \frac{\Delta I_L}{8C_{filter}}\delta T + V_{C1,\min}$$
$$V_{C2,\min} = -\frac{\Delta I_L}{8C_{filter}}(1-\delta)T + V_{C1,\min} \qquad (7.2.8)$$

Therefore, the ripple in filter capacitor voltage $\Delta V_{C,filter} = V_{C1,max}\text{-}V_{C2,min}$ in terms of inductor current ripple is expressed as

$$\Delta V_{C,\,filter} = \frac{1}{8C_{filter}\,f_s}\Delta I_L \qquad (7.2.9)$$

Value of the filter capacitor is calculated from (7.2.9) and (7.2.4)

$$C_{filter} = \frac{T}{8}\left(\frac{I_{i,nom}}{V_{i,nom}}\right)\left(\frac{\Delta I_L}{I_{i,nom}}\right)\left(\frac{\Delta V_{C,\,filter}}{V_{i,nom}}\right)^{-1} \qquad (7.2.10)$$

where $(\Delta V_{C,filter}/V_{i,nom})$ is the fractional change in filter capacitor voltage with respect to nominal input voltage. Therefore, for 25.4% of inductor current ripple and 1% of voltage ripple, calculated value of filter capacitor is C_{filter} = 81.14μF. Value of capacitance selected is 110 μF. Thus ripple in the filter capacitor voltage reduces to less than 1% and is equal to 0.74%

7.2.3.2 Calculation of the output capacitor *C* and the value of the filter inductor L_{filter}

Figure 7.2.4 shows the variation in the voltage across the output capacitor and filter inductor together with the current through the filter inductor.

For the worst case situation, $I_{o,\max}$ = 1.348A and the maximum duty ratio $\delta_{\max}$ = 0.875. Capacitor voltage ripple ΔV_C is considered as equal to 0.1V. Fraction of capacitor voltage ripple with respect to the nominal battery voltage $V_{B,nom}$ (=48V) i.e. $\Delta V_C/V_{B,nom}$ is equal to 0.2%. Value of the capacitor C is calculated by the expression (7.2.11) [14].

$$C = \left(\frac{I_{o,\max}}{V_{B,nom}}\right)\left(\frac{\delta_{\max}}{f_s}\right)\left(\frac{\Delta V_C}{V_{B,nom}}\right)^{-1} \qquad (7.2.11)$$

Calculated value of C is 614.32μF. Considered value of the capacitor is 660 μF. This reduces the capacitor voltage ripple to 0.186% and ΔV_C to ≈0.09V.

Voltage across the filter inductor is given by (7.2.12)

$$v_{L,\,filter} = L_{filter}\frac{di_o}{dt} = v_c - V_B \qquad (7.2.12)$$

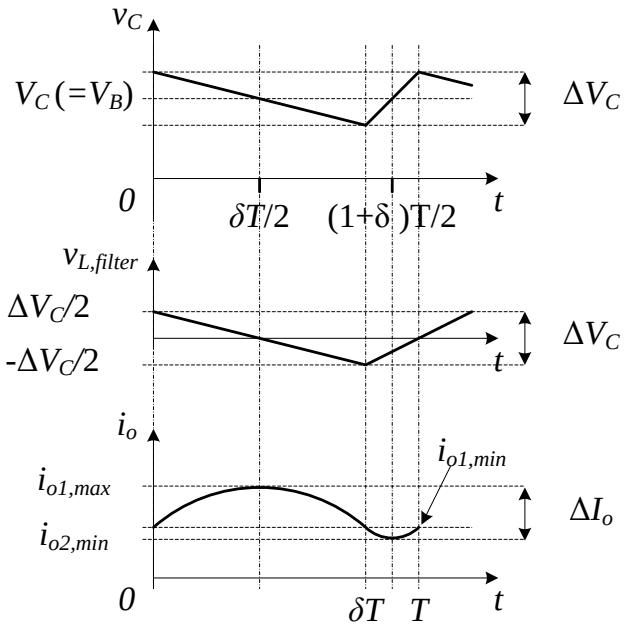

Fig.7.2.4. waveforms of the voltage across the output capacitor and current through the filter inductor

As the average voltage across the filter inductor is equal to zero, therefore average voltage across the capacitor C remains equal to battery voltage V_B. Thus from (7.2.12) voltage ripple across the filter inductor follows the voltage ripple across the output capacitor as shown in figure. In this case also we have the same situation as it was in the case of filter capacitors discussed in previous section. Voltage across the filter inductor $v_{L,filter}$ is expressed as (7.2.13).

$$v_{L,\,filter} = \begin{cases} -\dfrac{\Delta V_C}{\delta T}\left(t - \dfrac{\delta T}{2}\right) & 0 \le t \le \delta T \\ \dfrac{\Delta V_C}{(1-\delta)T}\left(t - \dfrac{1+\delta}{2}T\right) & \delta T \le t \le T \end{cases} \qquad (7.2.13)$$

Current i_o through filter inductor is given by (7.2.14)

$$i_o = \frac{1}{L_{\,filter}} \int v_{L,\,filter}\, dt + const \qquad (7.2.14)$$

With the boundary conditions, $i_o = i_{o1,\min}$ at $t = 0$ and $i_o = i_{o2,\max} = i_{o1,\min}$ at $t = \delta T$, (7.2.14) result in the expressions of i_o as in (7.2.15).

$$i_o = \begin{cases} -\dfrac{\Delta V_C}{2\delta T L_{\,filter}}\left(t - \dfrac{\delta T}{2}\right)^2 + \dfrac{\Delta V_C}{8C_{\,filter}}\delta T + i_{o1,\min} & 0 \le t \le \delta T \\ \dfrac{\Delta V_C}{2(1-\delta)TL_{\,filter}}\left(t - \dfrac{1+\delta}{2}T\right)^2 - \dfrac{\Delta V_C}{8C_{\,filter}}(1-\delta)T + i_{o1,\min} & \delta T \le t \le T \end{cases} \qquad (7.2.15)$$

Output current reaches to its maximum and minimum value at $t = \delta T/2$ and $t = (1+\delta)T/2$ as shown in *Figure 7.2.4*. Maximum and minimum values of i_o are

$$i_{o1,\max} = \frac{\Delta V_C}{8L_{filter}}\delta T + i_{o1,\min}$$
$$i_{o2,\min} = -\frac{\Delta V_C}{8L_{filter}}(1-\delta)T + i_{o1,\min} \qquad (7.2.16)$$

Thus the output current ripple ΔI_o (= $i_{o1,\max}$-$i_{o2,\min}$) and the ripple in output capacitor voltage ΔV_C are related as

$$\Delta I_o = \frac{1}{8L_{filter} f_s}\Delta V_C \qquad (7.2.17)$$

(7.2.17) can be re-arranged as

$$L_{filter} = \frac{1}{8 f_s}\left(\frac{V_{B,nom}}{I_{B,C10}}\right)\left(\frac{\Delta V_C}{V_{B,nom}}\right)\left(\frac{\Delta I_o}{I_{B,C10}}\right)^{-1} \qquad (7.2.18)$$

where $\Delta I_o/I_{B,C10}$ is the fraction of battery current ripple with respect to the nominal battery charging current C10.

It is considered that battery current ripple should be 5% of C/10. As the battery is of 100A.h so 5% of C/10 (=10A) is 0.5A i.e. ΔI_o=0.5A. With the selected value of capacitor C=660μH and ΔV_C =0.09V value of filter inductor is 1.125μH. Considered value of L_{filter} is 10μH. Therefore the current ripple is 0.57% of C10 of the battery nominal charging current.

Selected values of the passive components of the boost converter are tabulated in *Table 7.2.3*.

Tab.7.2.3: Values of the passive components	
Passive component	Values
Input inductor	323 μH
Filter capacitor	100 μF
Output capacitor	660μF
Filter inductor	10 μH

7.3 Experimental arrangement of boost converter with DSP and DSP interface circuitry

For the control of boost converter, DSP interface is made. PV module current, voltage and battery voltage were considered as input for the MPPT and control algorithm. For voltage sensors op-amp as a differential amplifier is considered with reduction of 15/3V and 56/3V for measurement of input and output voltage respectively, 0-15A range LEM current sensor is used with minimum 2.5V for 0A, and 3.125V for 15A. Interface circuit layout with sensor positions are shown in *Figure 7.3.1*. TMS320F28335 experimenter kit is used for the implementation of control algorithms. *Figure 7.3.2* shows the experimental arrangement of boost converter with DSP and interface circuitry.

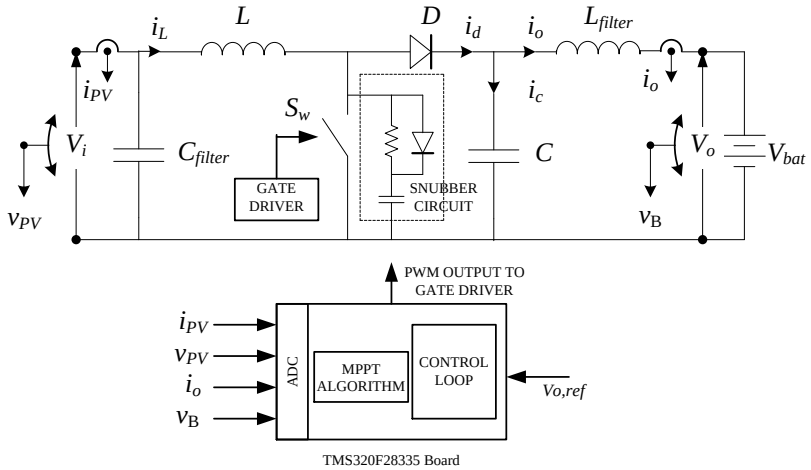

Fig.7.3.1. DSP interface of the boost converter

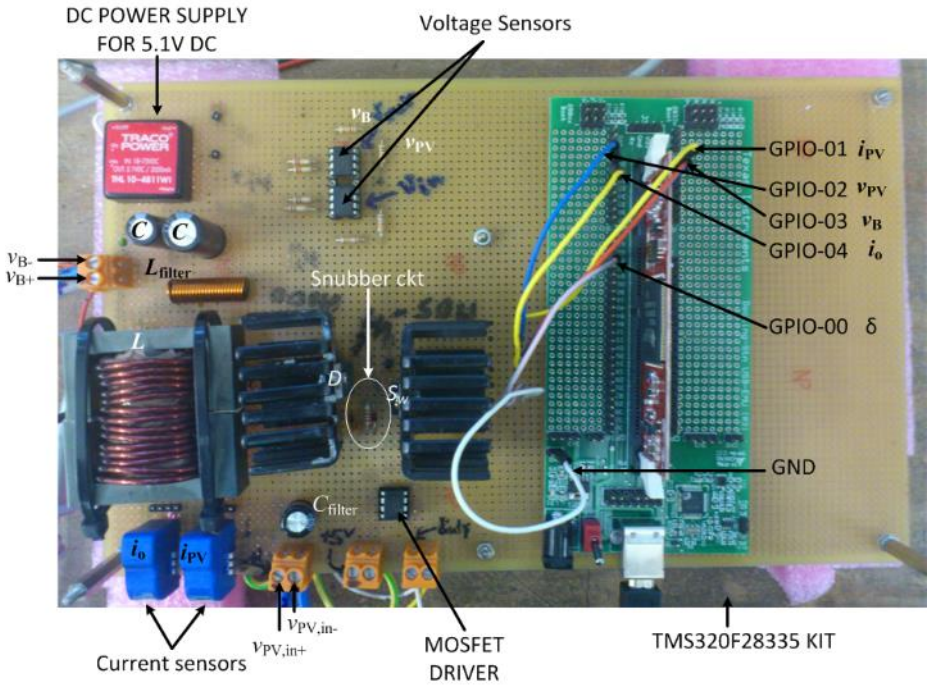

Fig.7.3.2. DC-to-DC boost converter with DSP and interface circuit

7.3.1 Diode and MOSFET

Schottky diode 16CTQ100PBF is used as a diode for the boost converter. I6CTQ100PBF pack is a three pin arrangement as shown in *Figure 7.3.3* and consists of two diodes with individual maximum average current rating 8A and maximum reverse voltage 60V. Two diodes are connected in parallel.

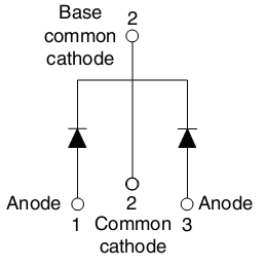

Fig.7.3.3. 16CTQ100PBF

IRFB 3307ZPBF MOSFET is used as a switch with current and voltage ratings 84A and 75V respectively.

7.3.2 MOSFET driver

TC1411N MOSFET driver is used to drive the MOSFET of the converter. Maximum output current of the driver is 1A with the possibility of 5, 10 or 15V supply. This driver is used with +5V biasing supply. Duty ratio output from the DSP at GPIO-00 is provided to the driver as an input. Output of this driver is connected to the Gate terminal of the MOSFET. Functional block diagram and PIN out of the driver are shown in *Figure 7.3.4*.

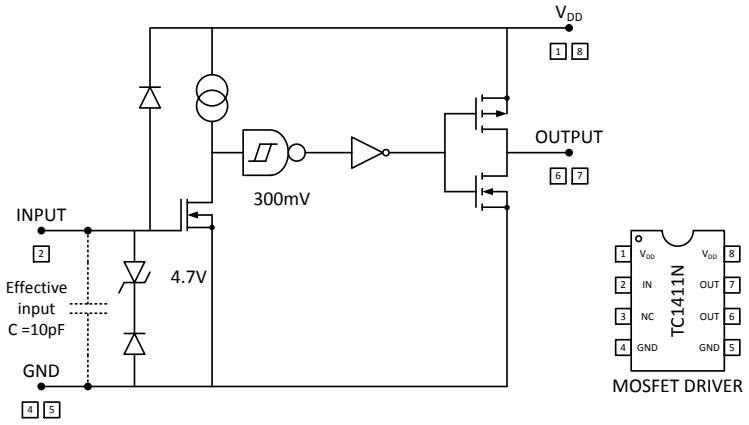

Fig.7.3.4. Functional block diagram and PIN out of TC1411N MOSFET driver [MICROCHIP]

7.3.3 Passive components

Input inductor L of 323μH is made from the 2.0mm dia and 2HG varnish coated copper wire. Rod Core Choke 10μH 5A inductor is selected as filter inductor. 100μF 63V electrolytic capacitor is selected for filter capacitor C_{filter} and two parallel connected 330μF 63V capacitors are selected as output capacitor C.

7.3.4 Voltage sensor circuit

Inverting op-amp as a differential amplifier as shown in *Figure 7.3.5* is considered as voltage sensor.

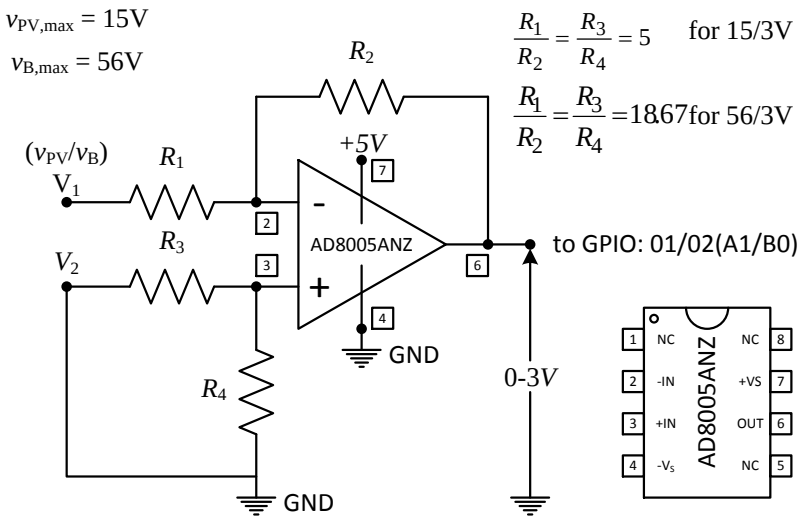

Fig.7.3.5. Voltage sensor circuit and connections

AD8005ANZ op-amp is used for the voltage sensors. Ratio R_1/R_2 and R_3/R_4 are kept equal and is equal to 5 for 15V to 3V reduction for the sensor for v_{PV} and is 18.67 for the battery voltage v_B. Relation between input and output of the voltage sensor is given by

$$V_{out} = \left(\frac{R_1 + R_2}{R_3 + R_4}\right)\left(\frac{R_4}{R_1}\right)V_2 - \frac{R_2}{R_1}V1 \qquad (7.3.1)$$

For $R_1/R_2 = R_3/R_4$, (7.3.1) reduces to the expression (7.3.2) which is enables the reduction in v_{PV} and v_B to admissible voltage to DSP.

$$V_{out} = \frac{R_2}{R_1}(V_2 - V_1) \qquad (7.3.2)$$

Values of R_1 and R_2 selected are $100k\Omega$ and $18k\Omega$ respectively for 15/3V and $220k\Omega$ and $10k\Omega$ respectively for 56/3V. Supply voltage biasing voltages for the considered op-amp circuit are +5V and 0.

7.3.5 Current sensor

LTSR 15-NP current transducer is considered as current sensors. An output voltage vs primary current characteristic of the selected current sensor is shown in *Figure 7.3.6*. LTSR 15-NP is suitable for the electronic measurement of DC, AC, pulsed and mixed current with a galvanic isolation between power circuit and control circuit. Primary nominal current I_{PN} is equal to 15A. It requires biasing voltage equal to +5V. Maximum input current for the input side of converter is 9A and for the output side is approx. 2A. Therefore, the current transducer works in the region on 0 to IPN with output voltage varying linearly from 2.5V to 3.125V.

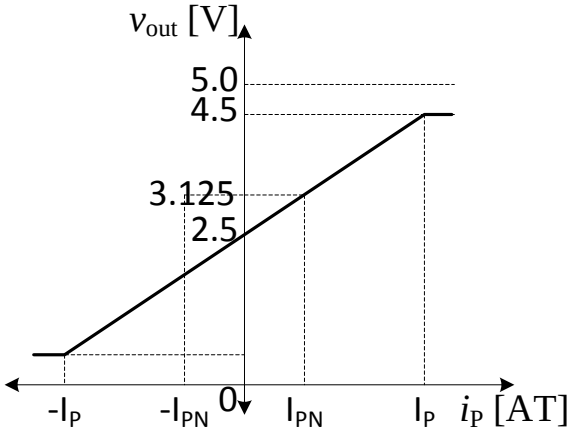

Fig.7.3.6. input output characteristic of LTSR 15-NP current transducer

Relationship between input current and output voltage is given by the expression (7.3.3).

$$v_o = 2.5 + \frac{0.625}{I_{PN}} i_P \qquad (7.3.3)$$

where i_P is the input current to the transducer. Maximum output voltage corresponding to the PV current is 2.875V and the maximum voltage corresponding to the output current of the boost converter is 2.583V.

7.3.6 Power supply for the MOSFET driver and sensors

To provide the biasing voltage of 5V, for current and voltage sensors and MOSFET driver, a 10W TRACO Power dc-to-dc converter THL 10-4811WI is considered. THL10-4811WI provides an output of 5.1V dc for input voltage from 18V to 75V and the maximum output current is 2000mA. DC power supply gets power from the dc-bus and is 84% efficient.

7.3.7 DSP

TMS320F28335 DSC is used for the implementation of control algorithm for the control of boost converter to follow maximum power point of PV module as per the insolation. i_{PV}, v_{PV}, i_o and v_B are the input variables to the DSP as obtained from the current and voltage sensors. Duty-ratio δ is the output variable after the control action and is fed to the input of MOSFET driver. Connection of the DSP with boost converter through interface circuitry is shown in *Figure 7.2.6*. Assignments of input/output variables to GPIO (General Purpose Input Output) pins are listed in *Table 7.2.4*.

Tab.7.2.4: input/output variables and GPIO connections

Variables	GPIO	Input/output
i_{PV}	01	Input
v_{PV}	02	Input
i_o	03	Input
v_B	04	Input
δ	00	Output

DSP uses 12bit ADC module with sample and hold to convert the analog input value into

corresponding digital values ranging from 0 to 4096. Conversion is carried out by the expression (7.3.4).

$$x_{ADC} = \begin{cases} 0 & x_{analog} < 0V \\ 4096 \times \dfrac{x_{analog} - ADCLO}{3} & 0V < x_{analog} < 3V \\ 4095 & x_{analog} > 3V \end{cases} \quad (7.3.4)$$

Analog input value is measured with respect to ADCLO pin which is connected to analog ground.

7.4 Current control of the boost converter

7.4.1 Transfer function for the current control scheme

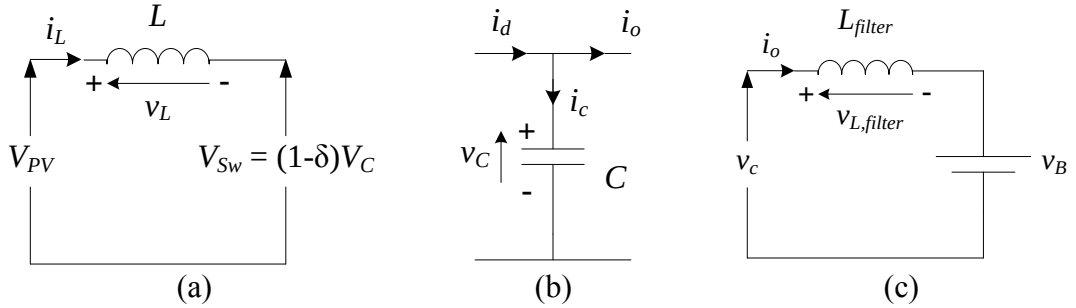

(a) (b) (c)

Fig. 7.4.1. Voltage and current distribution: a) input inductor; b) output capacitor; c) filter inductor

Figures 7.4.1a, 7.4.1b and *7.4.1c* show the distribution of voltage across and current through the passive components input inductor L, output capacitor C and filter inductor L_{filter}. Consider that the current through and voltage across L are i_L, and v_L respectively; voltage across the switch S_W is v_{Sw} and its average value is $V_{Sw} = (1\text{-}\delta)V_C$; V_C is the average value of the voltage v_C across the output capacitor; i_d, i_C and i_o are respectively diode current, output capacitor current and output current of the boost converter; $v_{L,filter}$ and v_B are the voltage across L_{filter} and battery; and V_{PV} is the output voltage of the PV terminal.

From the Kirchhoff's equations for *Figures 7.4.1a* and *7.4.1b* we have

$$L\frac{di_L}{dt} = \delta V_C - (V_C - V_{PV}) \quad (7.4.1)$$

$$i_C = i_d - i_o \Rightarrow C\frac{dV_C}{dt} = (1-\delta)i_L - i_o \quad (7.4.2)$$

Block diagram representation of the boost converter for current control is shown in *Figure 7.4.2*. The average voltage across L_{filter} is zero so the average value of the capacitor voltage equates to battery voltage i.e. $V_C = V_B$. Thus V_C can be considered as constant. Further, on considering (V_C-V_{PV}) as a disturbance, transfer function of the current loop is given by (6.4.3)

$$\frac{I_L(s)}{I_{ref}(s)} = \frac{s\dfrac{K_{p,c}V_C}{L} + \dfrac{K_{i,c}V_C}{L}}{s^2 + s\dfrac{K_{p,c}V_C}{L} + \dfrac{K_{i,c}V_C}{L}} = \frac{2\varsigma\omega_{n,c}s + \omega_{n,c}^2}{s^2 + 2\varsigma\omega_{n,c}s + \omega_{n,c}^2} \quad (7.4.3)$$

where $\omega_{n,c}^2 = \frac{K_{i,c}V_C}{L}$ and $2\zeta\omega_{n,c} = \frac{K_{p,c}V_C}{L}$ $\omega_{n,c}^2 = \frac{K_{i,c}V_C}{L}$. $K_{p,c}$ and $K_{i,c}$ are proportional and integral gain of the PI controller. Subscript 'c' is used to represent current loop. ζ is the damping factor and $\omega_{n,c}$ is the bandwidth of the current loop.

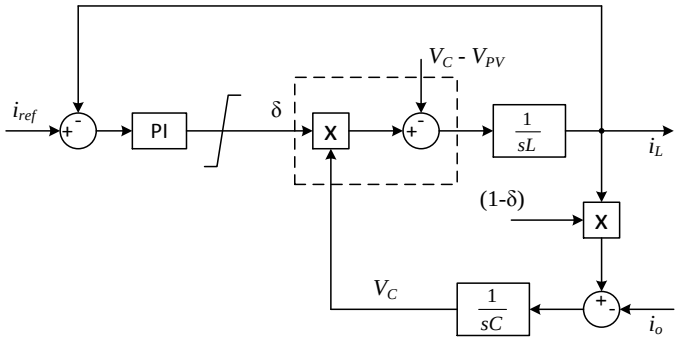

Fig. 7.4.2. Current control scheme for the boost converter

For the bandwidth of 1*k*Hz and ζ = 0.8 calculated values of $K_{p,c}$ and $K_{i,c}$ are equal to 0.058 and 227.7 respectively.

At the output side of the converter i.e. for the loop in *Figure 6.4.*1c, Kirchhoff's equation is written as

$$\left.\begin{aligned} v_c &= v_B + L_{filter}\frac{di_o}{dt} \\ v_C &= \frac{1}{C}\int i_C dt; \quad i_c = i_d - i_o \end{aligned}\right\} \qquad (7.4.4)$$

On differentiating the expression (7.4.4) with respect to time, we get a second order differential expression (7.4.5) for i_o.

$$\frac{d^2 i_o}{dt^2} + \omega_{o,\,filter}^2 i_o = \omega_{o,\,filter}^2 i_d - \frac{1}{L_{filter}}\frac{dv_B}{dt}; \quad \omega_{o,\,filter} = \frac{1}{\sqrt{L_{filter}C}} \qquad (7.4.5)$$

Consider that v_B remains constant over a period. Then the derivative term of v_B in (7.4.5) vanishes. Thus the transfer function $I_o(s)/I_d(s)$ is expressed as

$$\frac{I_o(s)}{I_d(s)} = \frac{\omega_{o,\,filter}^2}{s^2 + \omega_{o,\,filter}^2} \qquad (7.4.6)$$

7.4.2 Control scheme with Maximum Power Point Tracking Algorithm

Control scheme with Maximum Power Point Tracking (MPPT) algorithm is shown in *Figure 7.4.3*. Subroutine is called in an interval of 20ms. Symmetrical PWM modulation is used. Current and voltages are sampled at the middle of the PWM interval to read the average values of the current and voltage. Reference voltage is compared with the battery voltage. In case of difference, current reference generated by the voltage loop is compared with the current reference from the MPPT algorithm. In this case if current reference from MPPT is less than current reference from the voltage loop, reference current for current loop is set to that generated by the voltage loop; otherwise it is set to the reference from the MPPT algorithm. In case of no error in voltage loop current reference i_{ref} is set to zero.

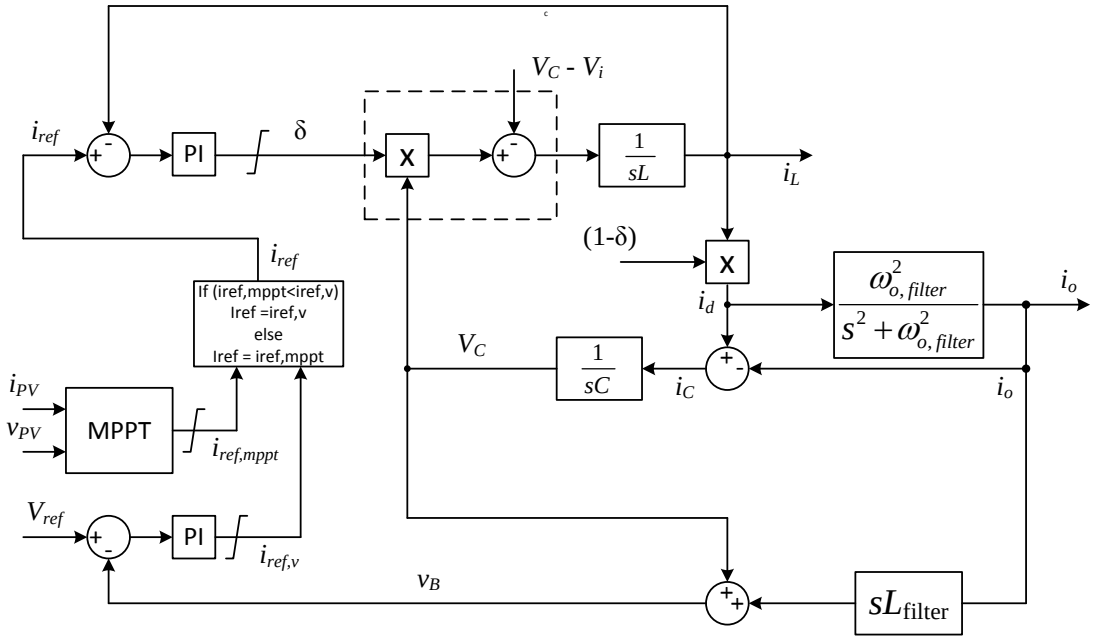

Fig. 7.4.3. Control scheme of the boost converter with MPPT algorithm

7.4.3 MPPT algorithm

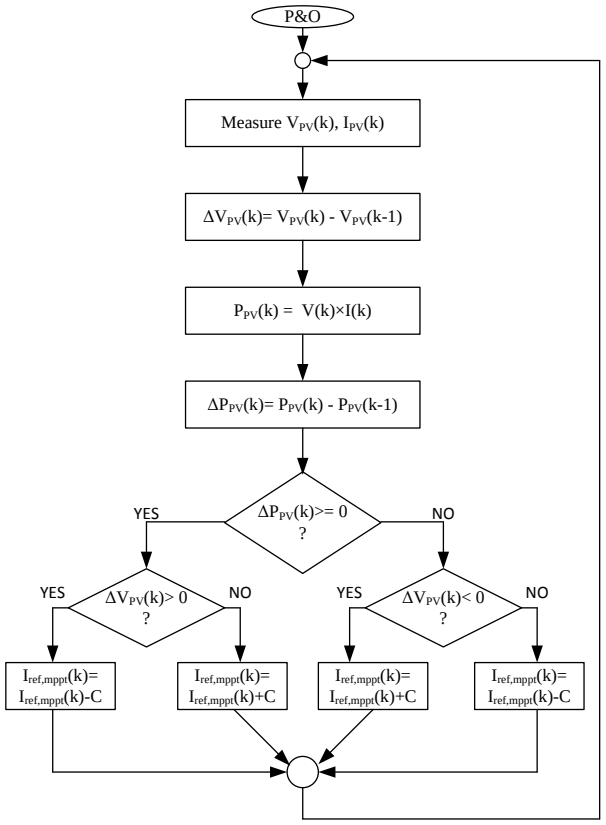

Fig. 7.4.4. P&O, current control MPPT algorithm

Perturb and observe (P&O) MPPT algorithm for current control [15] has been used to

track the Maximum Power Point (MPP) of the P-V characteristic of the PV module. P&O subroutine is called at the interval of 20ms. Algorithm is explained with the help of flow chart as shown in *Figure 7.4.4*. At first current and voltage samples $I_{PV}(k)$ and $V_{PV}(k)$ respectively of the PV module are acquired and then, the corresponding power $P_{PV}(k)$ is computed. Change in the voltage $\Delta V_{PV}(k)$ and power $\Delta P_{PV}(k)$ with respect to previous sampled value are computed. In case of $\Delta P_{PV}(k) > 0$, sign of $\Delta V_{PV}(k)$ is checked. If $\Delta V_{PV}(k)$ is positive current reference $I_{ref,MPPT}$ is decreased otherwise it is increased by a fixed value (perturbation) C. In case of $\Delta P_{PV}(k) < 0$, for negative $\Delta V_{PV}(k)$ $I_{ref,MPPT}$ is perturbed with positive C and for positive $\Delta V_{PV}(k)$ $I_{ref,MPPT}$ is perturbed by negative C. After this current reference i_{ref} is updated and the subroutine becomes idle until the next call.

7.4.4 Verification of MPPT algorithm through DC power supply

In practice, a photovoltaic panel is a non-linear source network, and cannot be considered as Thevenin's or Norton equivalent source network as is done for the case of linear active and bilateral source network. But for the purpose of the verification of the tracking of boost converter with battery load to the MPP, a simple experimental arrangement is proposed. It is considered that, a PV panel is equivalent to a DC power supply $V_{dc,supply}$ in series with a resistance R_s as is shown in *Figure 7.4.5a*. $V_{dc,supply}$ and R_s corresponds to $I_G R_{SH}$ and (R_S+R_{SH}) respectively of the simplified equivalent circuit model of a PV panel shown in *Figure 7.1.5*. Presence of the non-linear component diode D is neglected for the sake of equivalence with a linear network. Therefore a combination of dc power supply in series with an external resistor R_s can be considered as a Thevenin equivalent circuit of a dc source network with V_{th} equal to the set $V_{dc,supply}$ and I_{th} equal to V_{th}/R_s.

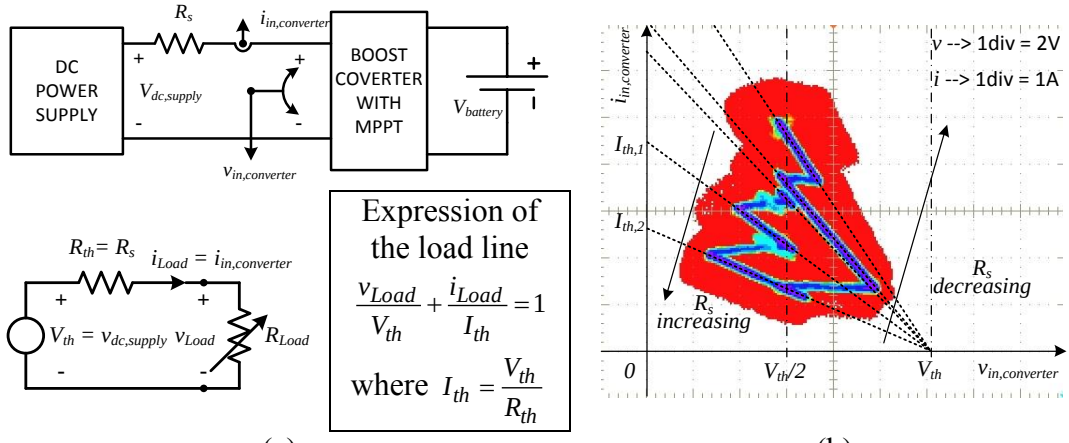

(a) (b)

Fig. 7.4.5 a) experimental circuital arrangement for the verification of MPPT and Thevenin equivalent circuit; b) I-V curve of the source network confirming tracking of maximum power point, with the variation in series resistance R_s.

R_{Load} is the equivalent resistance of the boost converter together with battery as seen from the input side of converter. Load lines for such a supply for different values of R_s are shown in *Figure 7.4.5b* by dotted lines. With each variation in series resistance R_s, boost converter together with MPPT algorithm adjusts its equivalent resistance R_{Load} to be equal to the sum of the series resistance and the internal resistance of the dc supply, so as to enable maximum power absorption by the load from the dc supply network. At maximum power point, voltage across the load becomes equal to the half of the Thevenin's voltage, as are

observed in experimental results along $v_{in,converter} = V_{th}/2$. Any perturbation in source current caused by changing the series resistance, leads to the point of maximum power fulfilling the criteria of maximum power transfer theorem. Observations are in line with the theory, thus tracking along MPP line verifies functionality of the MPPT algorithm.

7.5 Experimental results and discussion

7.5.1 Open loop waveforms

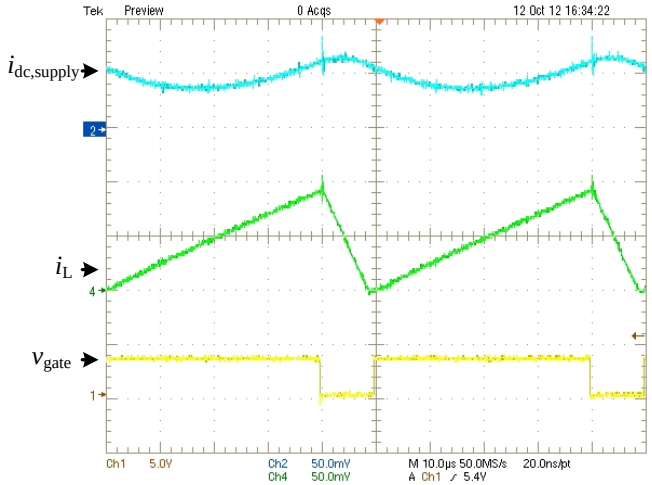

Fig.7.5.1. waveforms of dc supply current (*pink*), inductor current (*green*) and gate pulses to the MOSFET (*yellow*) in case of open loop control

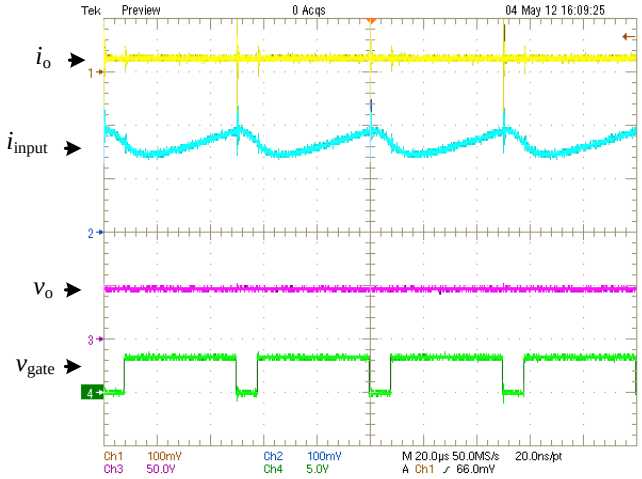

Fig.7.5.2. waveforms of output current (*yellow*), input current (*green*) output voltage (blue) and gate pulses to the MOSFET (*green*) in case of open loop control

For the open loop test, boost converter is fed by a dc supply with input voltage 8.5V and average input current 0.46A. *Figure 7.5.1* shows the waveforms of the input current (*pink*), inductor current (*green*) and gate pulses to the MOSFET (*yellow*). Converter is operated with duty-ratio 0.8 at 20*k*Hz switching frequency. Converter operates at the boundary of the continuous and discontinuous mode of conduction. 7.17% of current ripple with

respect to $I_{PV,nom}$ is observed in the supply current. *Figure 7.5.2* shows the waveforms of input current, output current, output voltage and gate pulses. Duty-ratio for this case is 0.8, input current is 1.8A (average) output current is 0.3A

7.5.2 Waveforms with P&O current control MPPT algorithm

Figures 7.5.3 and *7.5.4* shows the variations in current and voltage at the input and output of the boost converter fed by the PV module. In the first case input current is 6.4A and output current is approx. 0.8A and the input voltage is 6V. Output current ripple observed is 1% with respect to the C/10 charging current of the battery.

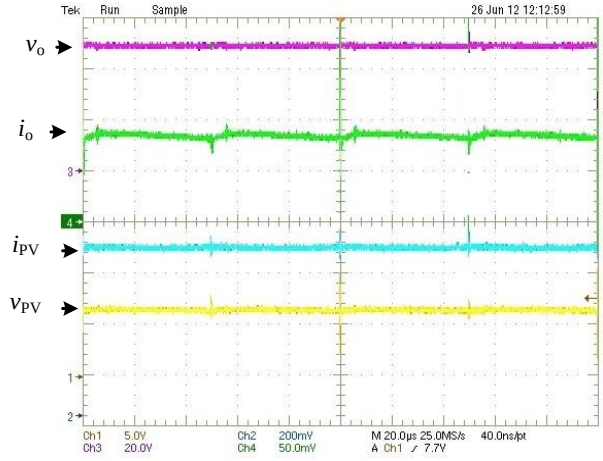

Fig.7.5.3. waveforms of the output voltage (blue), output current (*green*), input current (*pink*), PV module voltage (*yellow*)

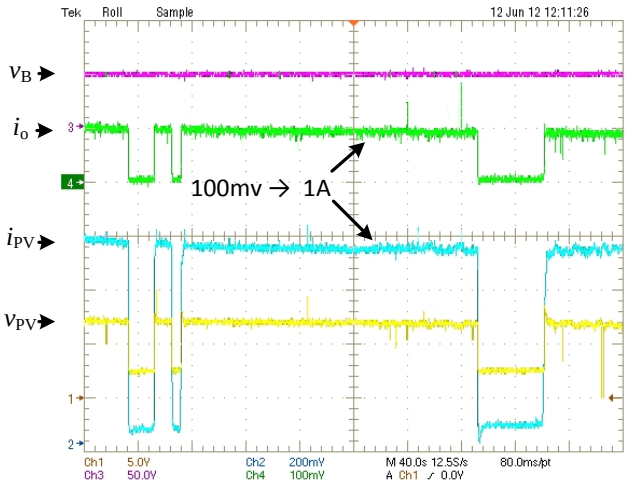

Fig.7.5.4. waveforms of the output voltage (blue), output current (*green*), input current (*pink*), PV module voltage (*yellow*)

Figure 7.5.4 is the trace of the input and output circuit variables captured in the span of 400 seconds. Regions of the drops in input voltage and current and output current of the converter is caused by creating 100% shading from direct insolation on the PV module. When module is exposed to sun it works around MPP, with the PV current varying from 7.2A to 7.6A and v_{PV} at around 7V. During the full shading conditions MPPT is not active.

To validate the proper functionality of the control with MPPT, call of MPPT algorithm is set to active state when the PV current is more than 3.5A. As it is observed in the *Figure 7.5.5* that, the time span during which PV current is less than 3.5A, output current is zero. As the PV current becomes greater than 3.5A, MPPT algorithm becomes active and tries to bring the operating point to Maximum power point. Thus increase in input current, input voltage and output current are observed and settles to the set MPP reference.

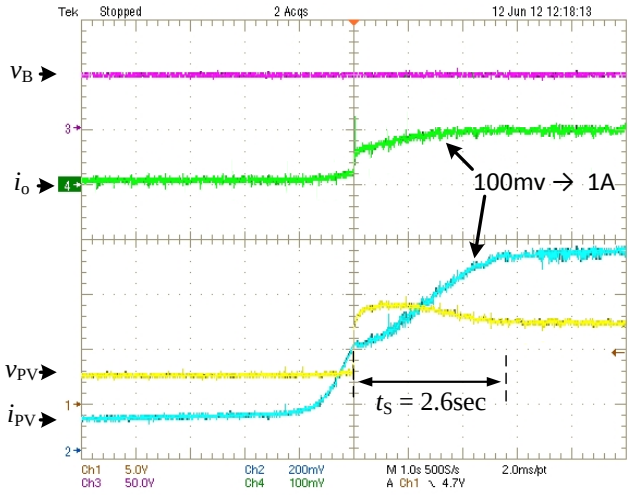

Fig.7.5.5. waveforms of the output voltage (blue), output current (*green*), input current (*pink*), PV module voltage (*yellow*)

Trace in the *Figure 7.5.5* is the capture of 10 seconds. From the waveform of PV current from the instant of activation of MPPT it takes 2.6sec to achieve MPP point. *Figure 7.5.6* shows the tracking of MPP.

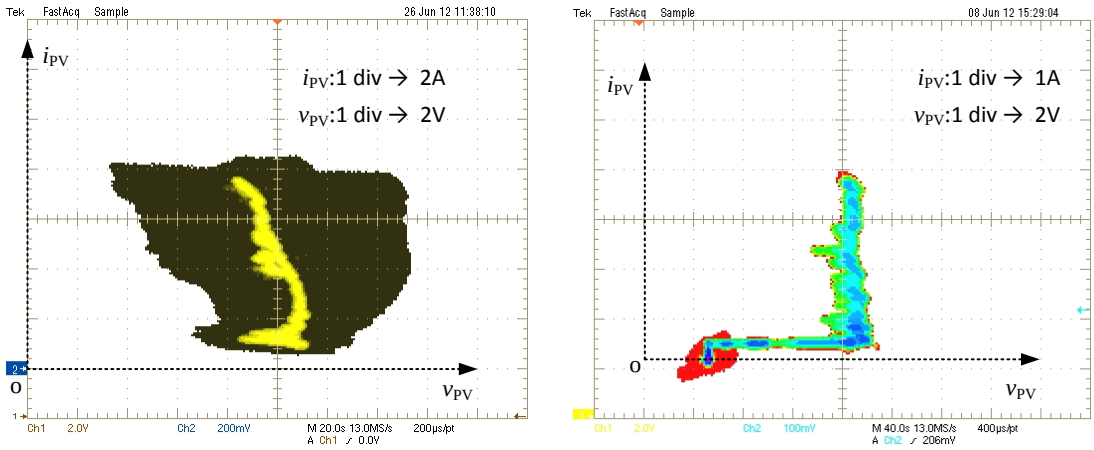

Fig.7.5.6. tracking of maximum power point I-V characteristics curve under different solar insolation

7.6 Experimental and analytical measurement of efficiency

Efficiency of the dc-to-dc boost converter is defined by the ratio of output power to input power.

$$\eta_{converter} = \frac{P_{out}}{P_{in}} = 1 - \frac{P_{loss}}{P_{in}} \qquad (7.6.1)$$

where output power $P_{out} = v_{B} i_{o}$ and input power $P_{in} = v_{PV} i_{PV}$. Power loss in the converter P_{loss} is equal to $P_{out} - P_{in}$. Power loss components are, switching and conduction losses in switch and forward diode, and conduction and core losses in input and filter inductor [16]. Efficiency of the converter can be determined by experimental, and or analytical approach.

7.6.1 Efficiency measurement through experimentation

For the measurement of the efficiency YOGOKAWA power analyser is used. Expected time of the experimentation for the measurement of efficiency has been decided, from the information of estimated hourly irradiance of PVGIS CM-SAF database for June.

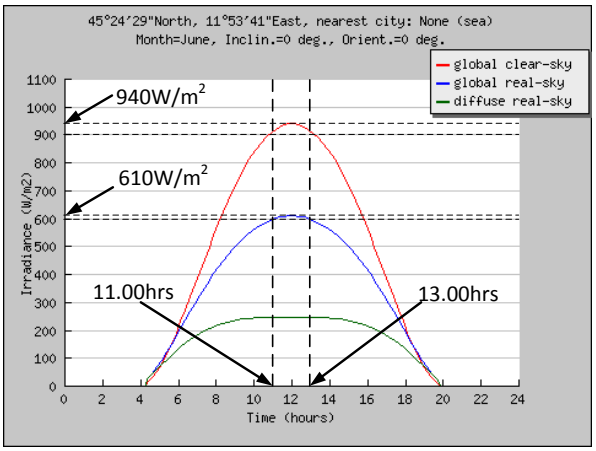

Fig.7.6.1. estimated hourly irradiance (W/m^2) from PVGIS data base, in June at the location of laboratory.

As shown in *Figure 7.6.1*, during 11:00AM to 1:00PM variation in global irradiance for real sky (blue line) varies from 601W/m^2 to 610W/m^2. Expected peak output power from the panel is 50W (approx.). *Figure 7.6.2* shows the variations in input power to the boost converter, its efficiency and gain.

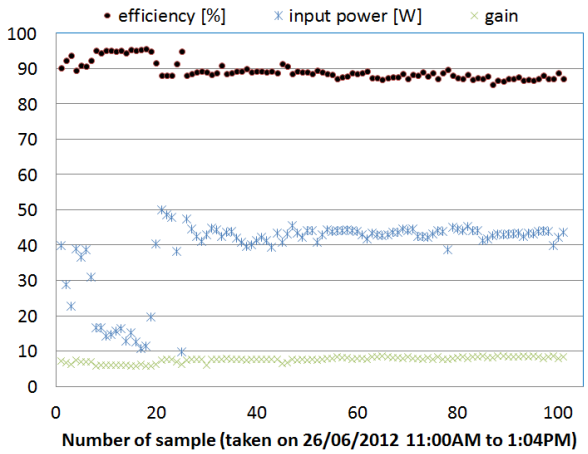

Fig.7.6.2. variations in input power to the boost converter, efficiency and gain of the converter on 26th June 2012, during peak of the global irradiance.

Peak power of 50W (approx.) is observed during the measurement. Against the estimation, observed lower values of the input power during peak hour of irradiance are because of partial shading of PV panel due clouds. For the lower irradiance, during input power variation from 10 to 30W highest efficiency around 95% has been observed. For input power near to the nominal value (43W), efficiency varies from 87 to 90% as shown in *Figure 7.6.3a*. For the nominal input power efficiency stays at around 89%. Variation of efficiency with gain is shown in *Figure 7.6.3b*. Gain of the converter varies from 5.5 to 8.8, efficiency of the converter drops with the increase in gain.

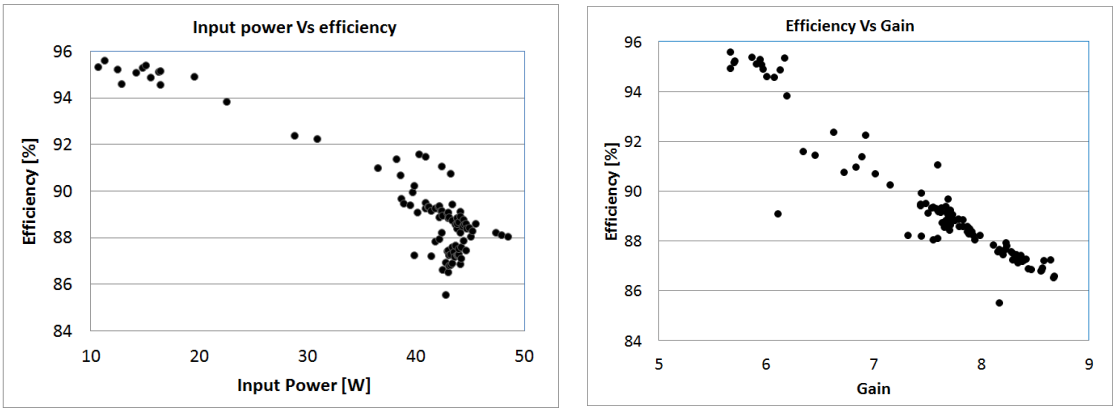

Fig.7.6.3. efficiency vs input power plot of the boost converter under varying solar insolation

With the increase in isolation, increase associated conduction, switching and core losses take place and causes drop in the efficiency. Major loss component responsible for the drop in efficiency is conduction loss in the inductor. Effect of the various loss components on the efficiency and gain of the converter have been explained analytically in the next subsection.

7.6.2 Analytical verification of drop in efficiency

Loss components of the boost converter can be summarized as, switching, conduction and core losses [16]-[20]. Switching loss P_{sw} can further be classified into ON state loss $P_{sw,ON}$ due to ON state voltage drop $V_{sw,ON}$ and commutation loss $P_{\mathrm{sw,com}}$ during commutation from ON state to OFF state. Similarly diode has losses $P_{D,ON}$ during ON state and reverse recovery loss $P_{D,rr}$ during reverse recovery period of the diode. Conduction losses $P_{ind,cond}$ is due to resistances of input and filter inductor, r_L and $r_{L,filter}$ respectively, and $P_{Sw,cond}$ is due ON state resistances of switch and diode r_{Sw} and r_{d} respectively. Core losses P_{core} are eddy current loss $P_{core,e}$ and hysteresis losses $P_{core,h}$ in ferrite core of the inductors. Ferrite cores are characterised with negligible eddy current loss. Therefore expression of the total loss P_{loss} in the converter is expressed as (7.6.2)

$$P_{loss} = P_{ind,cond} + P_{Sw,cond} + P_{sw} + P_D + P_{core} \qquad (7.6.2)$$

Analytical models for the estimation losses in MOSFET (*Sw*) and diode (*D*), and core loss in input inductor (*L*) are discussed in [18]-[20]. However here simplified loss component model of the considered dc-to-dc boost converter as shown in *Figure 7.6.4* has been considered.

As our objective is to provide an analytical support to the drop in efficiency with the increase in solar irradiance, and to look for the factor responsible, at first $P_{sw,com}$, $P_{D,rr}$ and

P_{core} are neglected. Analytical efficiency determined with this consideration is then compared with the experimental value. Information of the differences between analytical and experimental result is used to determine residual resistance r_{res} equivalent to neglected loss components P_{res} by curve fitting. r_{res} is expressed as a function of duty ratio. r_{res} is considered as in series with the input inductor. This approach gives satisfactory result. Values of the associated parameters for the computation of efficiency are enlisted in *Table 7.6.1*.

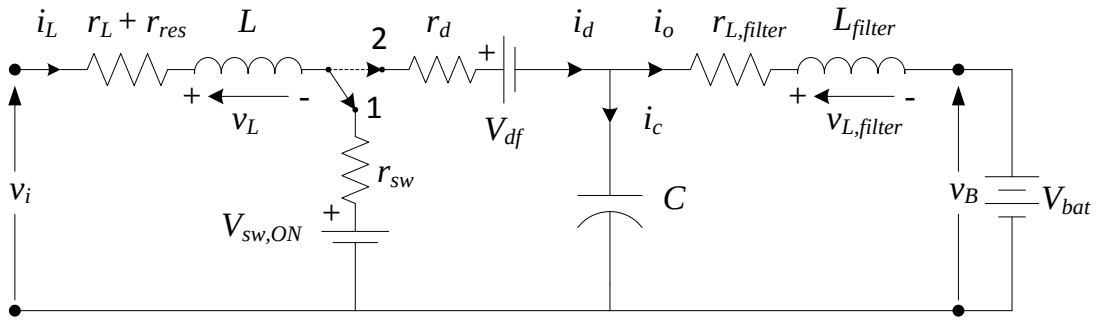

Fig.7.6.4. Circuital layout of dc-to-dc boost converter with loss components

Tab.7.6.1: Parameters of the dc-to-dc boost converter for analytical calculation of efficiency		
Input inductor resistance	r_L	72.4mΩ
Filter inductor resistance	$r_{L,filter}$	13mΩ
Dynamic resistance of forward diode	r_d	11.1mΩ
Drain to source resistance of MOSFET	r_{sw}	4.6mΩ
ON-state voltage of switch	$V_{sw,ON}$	0.1V
Forward voltage drop across diode	$V_{D,ON}$	0.72V

It is considered that the average values of the circuit variables, i_L, i_C, i_o, v_L and v_C corresponds to the average of the corresponding maximum and minimum values and are represented by I_L, I_C, I_o, V_L and V_C respectively.

Average values of the capacitor current i_C, filter inductor voltage $v_{L,filter}$, and input inductor v_L are given by the expressions (7.6.3), (7.6.4) and (7.6.5) respectively.

$$I_C = -I_o d + (I_L - I_o)(1-d) \qquad (7.6.3)$$

$$V_{L,\,filter} = V_C - V_B - I_o r_{L,\,filter} \qquad (7.6.4)$$

$$V_L = \left(V_i - I_L(r_L - r_{res}) - I_L r_{Sw,ON} - V_{Sw,ON}\right)d + \left(V_i - I_L(r_L - r_{res}) - I_L r_{D,ON} - V_{D,ON} - V_C\right)(1-d) \qquad (7.6.5)$$

For average values of i_C, v_L and $v_{L,filter}$ to be zero, (7.6.3) to (7.6.5) result in

$$\frac{I_L}{I_o} = \frac{1}{1-d} \qquad (7.6.6)$$

$$V_C = V_B + I_o r_{L,\,filter} = V_B\left(1 + \frac{I_o r_{L,\,filter}}{V_B}\right) \qquad (7.6.7)$$

$$V_C = \frac{V_i}{1-d}\left[1 - \frac{V_{Sw,ON}}{V_i}d - \frac{V_{D,ON}}{V_i}(1-d)\right] - \frac{I_L}{1-d}\left[(r_L + r_{res}) + r_{Sw,ON}d + r_{D,ON}(1-d)\right] \qquad (7.6.8)$$

With the help of (7.6.6), (7.6.7), and (7.6.8), overall gain $G = V_B/V_i$, of the boost converter is given by (7.6.9)

$$G = \frac{V_B}{V_i} = \frac{\frac{1}{1-d}\left[1 - \frac{V_{Sw,ON}}{V_i}d - \frac{V_{D,ON}}{V_i}(1-d)\right]\left(1 + \frac{I_o r_{L,\,filter}}{V_B}\right)^{-1}}{1 + \frac{1}{1-d}\left[(r_L + r_{res}) + r_{Sw,ON}d + r_{D,ON}(1-d)\right]\left(\frac{I_L}{V_B}\right)\left(1 + \frac{I_o r_{L,\,filter}}{V_B}\right)^{-1}} \qquad (7.6.9)$$

Since the resistive drop $I_o r_{L,filter}$ is negligible as compared to V_B, so the fraction $I_o r_{L,filter}/V_B$ can be neglected without affecting the results. Thus (7.6.9) reduces to (7.6.10).

$$G = \frac{V_B}{V_i} = \frac{\frac{1}{1-d}\left[1 - \frac{V_{Sw,ON}}{V_i}d - \frac{V_{D,ON}}{V_i}(1-d)\right]}{1 + \frac{1}{1-d}\left[(r_L + r_{res}) + r_{Sw,ON}d + r_{D,ON}(1-d)\right]\left(\frac{I_L}{V_B}\right)} \qquad (7.6.10)$$

From, (7.6.1), (7.6.6) and (7.6.10), efficiency of the converter is expressed as

$$\eta_{converter} = \frac{\left[1 - \frac{V_{Sw,ON}}{V_i}d - \frac{V_{D,ON}}{V_i}(1-d)\right]}{1 + \frac{1}{1-d}\left[(r_L + r_{res}) + r_{Sw,ON}d + r_{D,ON}(1-d)\right]\left(\frac{I_L}{V_B}\right)} \qquad (7.6.11)$$

In the expressions of gain and efficiency, V_i and I_L are considered as equal to V_{PV} and I_{PV} respectively. Thus efficiency and gain of the converter turn out to be a function of duty ratio d, input current I_{PV} (hence solar irradiance), input voltage V_{PV} and various components as discussed at the beginning of this subsection.

Figure 7.6.5 shows the analytical plots of efficiency with varying input power as per solar irradiance and duty ratio, as obtained from the experimental measurement. Suffixes "CL", "SwCL" and "RL" are used to represent "conduction losses", "switch conduction loss", and "residual losses" respectively. 'i' and "ni" are used to represent "included" and "not included" respectively. To study the effect of various losses on the efficiency, analytical model is brought to the more practical one, in steps. Topmost plot in *Figure 7.6.5* is the efficiency when P_{cond} and P_{res} losses are not considered, i.e. only ON state switching and diode losses are considered. This variation is far from the measured one. Inclusion of $P_{ind,cond}$, brought the analytical curve very close to the measured one, as shown by SwCL_ni_RL_ni, third plot from the top. Inclusion of $P_{sw,cond}$ and $P_{D,cond}$ shifts the analytical efficiency curve more closer to the measured one as shown by SwCL_i_RL_ni.

Remaining difference between the measured and analytical plot is due to P_{res}. To avoid the complex process to determine it, as discussed earlier, r_{res} is considered in series with the

inductor and is expressed as

$$r_{res} = \frac{P_{res}}{I_{PV}^2} = \frac{\left(\eta_{anlytical} - \eta_{measured}\right)}{100 I_{PV}^2} P_{input} \qquad (7.6.12)$$

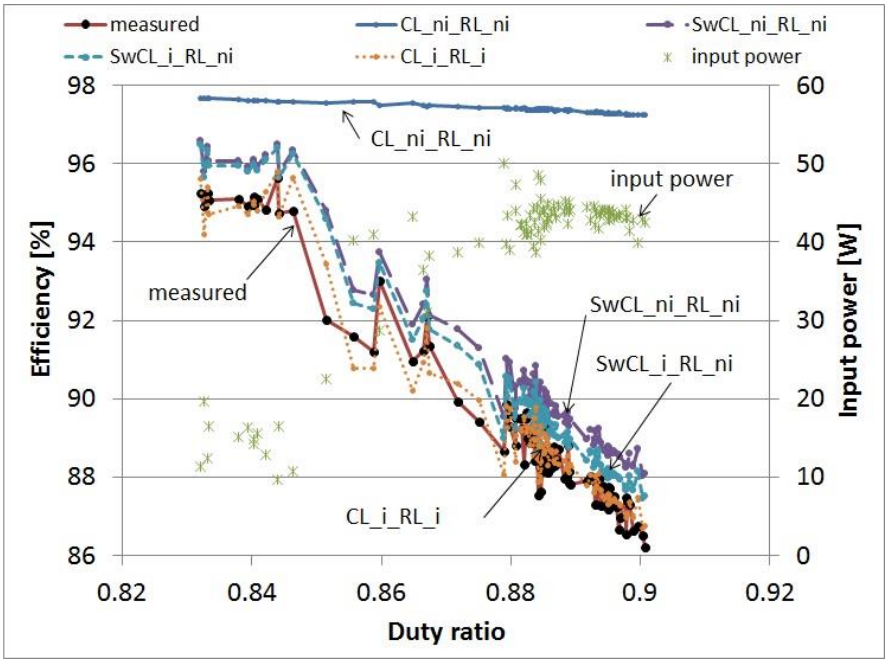

Fig.7.6.5. Variation in efficiency of the dc-to-dc boost converter with varying solar irradiance and duty ratio.

Value of the residual resistance widely varies with duty-ratio from lower solar irradiance to higher irradiance; satisfactory curve fit of its variation with duty ratio d is given by

$$r_{res} = 13.84d^2 - 24.76d + 11.82 \text{ Ohms} \qquad (7.6.13)$$

Although the above approximation is not an accurate approach, it gives much closeness of analytical value with the measured value, as shown in *Figure 7.6.5* by CL_i_RL_i, it can be used to analyse the effect of major loss components on the efficiency under the varying condition of input power and duty ratio.

Variation in associated losses and gain of the converter with input power and duty ratio are shown in *Figures 7.6.6* and *7.6.7* respectively. From the analytical plots for the losses, it is clear that all the loss components are smaller during the lower irradiance, comparably lower duty-ratio and gain. So it justify the higher efficiency of 95%. With the increase in input power because of increasing irradiance, increase in duty ratio takes place, increasing duty ratio, increases P_{res} (= $P_{ind,core}$ + $P_{sw,com}$+ $P_{D,rr}$) and ON state switch and diode losses ($P_{sw,ON}$+$P_{D,ON}$). Major drop in efficiency is caused by the conduction loss in input inductor, as is observed in both experimental and analytical measurement. Wide variation in $P_{ind,cond}$ takes place with the increase in irradiance i.e. with the increase in PV current i_{PV} as shown in *Figure 7.6.5* by the curve CL (inductor). Likewise, as shown by the curve CL_ni_RL_ni in *Figure 7.6.7*, gain is mostly affected by the resistive drop across the inductor. Thus for the present application as $P_{ind,cond}$ plays an important role in dropping down the efficiency of the converter due to increase conduction loss proper selection of cu-wire with lower

resistance for the inductor is important to improve the efficiency.

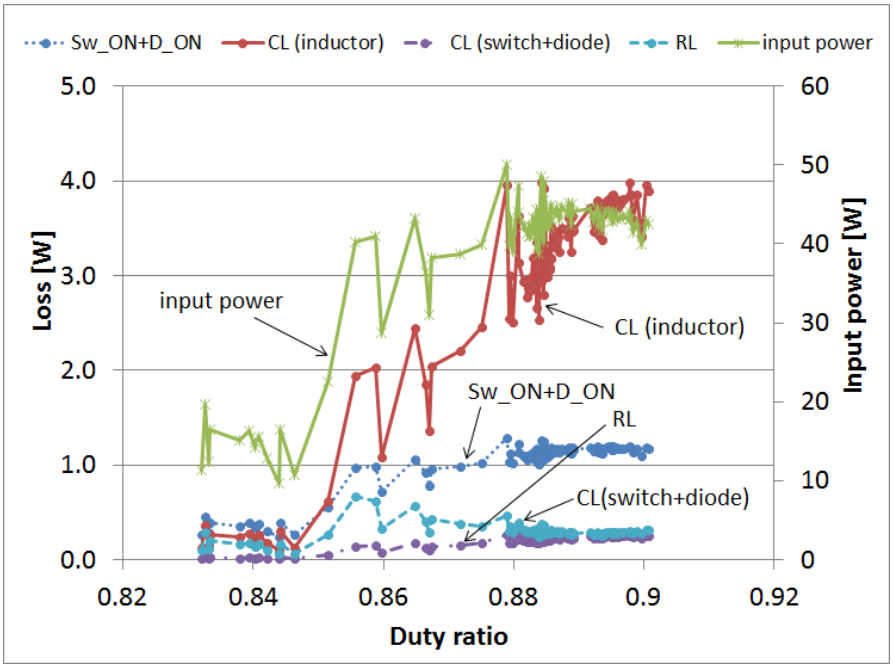

Fig.7.6.6. Variation in switching loss ($P_{sw,ON}$+$P_{D,ON}$); switch conduction loss ($P_{sw,cond}$+$P_{D,cond}$); inductor conduction loss $P_{ind,cond}$ and residual loss P_{res} ($P_{ind,core}$ + $P_{sw,com}$+ $P_{D,rr}$).

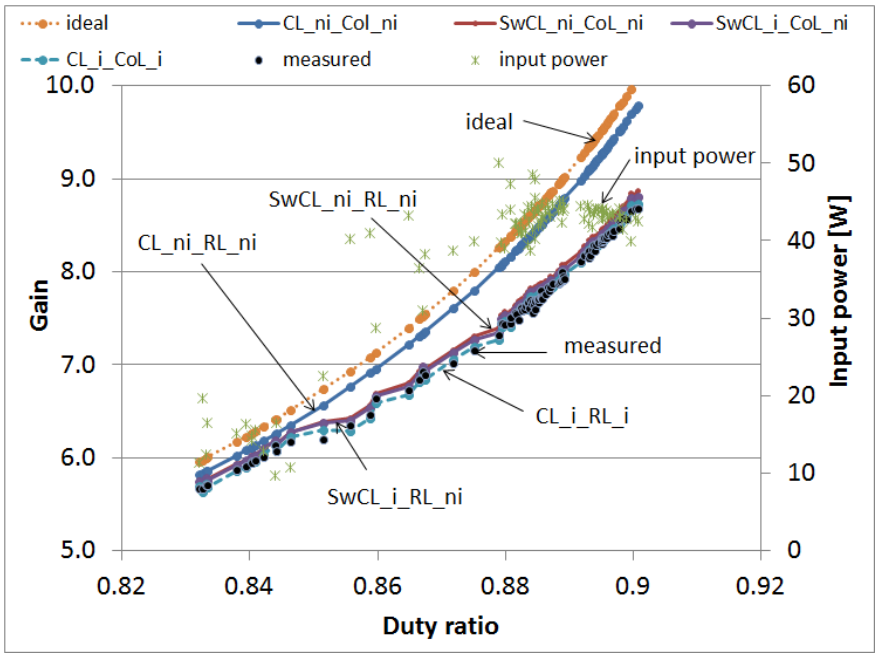

Fig.7.6.7. Measured and analytical variation in gain with input power and duty ratio.

Analytical variation in the efficiency and gain of the converter with duty ratio for nominal power of 43W is shown in *Figure 7.6.8*. From *Figure 7.6.7*, it can be confirmed that, at around nominal input power, converter operates with duty ratio 0.885 and gain 8.4. With

this value, plot of efficiency and gain vs duty-ratio confirms efficiency of 89% as measured from the experimental observation.

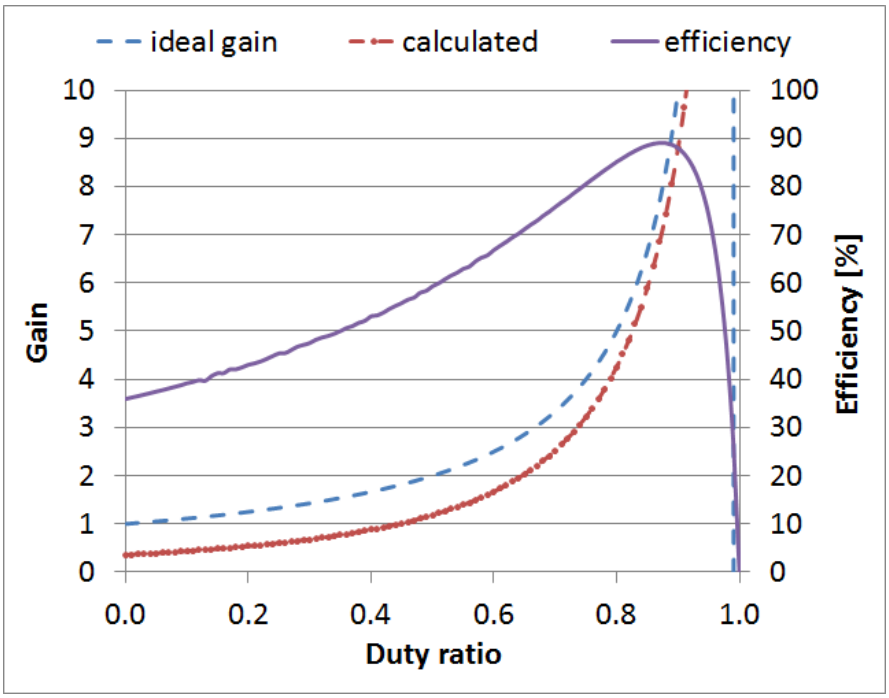

Fig.7.6.8. Variation in of the gain and efficiency of the converter with duty ratio.

7.6.3 Extension in autonomy of the mini-electric car

Annual average insolation available on horizontal surface in Padova is 3.46kWh/m^2/day, so with the considered panel it is possible to get 283Wh (=$3.46\times10^3\times0.156^2\times20\times0.168$) of energy per day. Thus the annual average energy per day, which could be submitted to the DC-bus from the PV panel, during day time is ≈252Wh (=283×0.89) and is equivalent to a 5Ah energy source connected to the DC-bus. Thus, if the mini-electric car consumes 50A of current while running at speed of 50km/hour continuously, possible extension in autonomy is at least 5km. This could be a good assistance to on board batteries with limited roof top space less than a half square meter (0.487m^2).

7.8 Conclusion

Variation in solar insolation and irradiance in Padua, Italy on a horizontal surface were estimated to determine the possible output from the considered multi crystalline SilFab PV panel. Nominal values of power, voltage and current have been considered to design a high gain and high efficiency dc-to-dc boost converter. Perturb and Observe current control MPPT algorithm has been used to track the maximum power point of the PV panel. An experimental strategy is suggested to validate the capability of designed boost converter to track maximum power point. Efficiency of the designed high gain boost converter under nominal condition is measured as 89% and validated with analytical facts with the help analytical efficiency model. Expected extension in the autonomy of the mini-electric car is at least 5km. Mini-electric car with implanted 20 cell SilFab PV panel is shown in *Figure 7.7.1*

Fig.7.7.1 mini-electric car Birò Estrimà with implanted 20 Cell SilFab PV panel

7.9 References

[1] T. Markvart, "Solar Electricity", second edition, John Willey & Sons Ltd., 2001.

[2] M. Pagliaro, R. Ciriminna and G. Palmisano, "Flexible Solar Cells", *ChemSusChem 2008*, vol. 1, pp. 880-891, 2008.

[3] Underwriters Laboratories UL, www.ul.com/dge/photovoltaics

[4] A. J. Anderson, "Final Report for Task 2.0", NREL subcontract No. TAD-4-14166-01, Oak Leaf Place (1995)

[5] G. Blaesser, PV Array Data Translation Procedure, Proc. 13th EC PVSEC (1995)

[6] International Electrotechnical Commission, IEC 891, Procedures for temperature and irradiance corrections to measured I-V characteristics of crystalline silicon photovoltaic devices, 1987.

[7] B. G. Streetman and S. Banerjee, "Solid State Electronic Devices", 5th Edition

[8] S. Coors and M. Bohm, "Application of the Two-Exponential Model to Correction Procedures for Silicon Solar Cells", *Proc. Of 1st EuroSun*, pp. 614-619.

[9] E. I. Ortiz-Rivera and F. Z. Peng, "Analytical Model for a Photovoltaic Module using the Electrical Characteristics provided by the Manufacturer Data Sheet", *Proc. of Power Elect. Spec. Conf.*, pp. 2087-2091, 2005.

[10] W. Herrmann and W.Wiesner, "Current-Voltage Translation Procedure for PV Generators in the German 1000 Roofs-Program", TÜV Rheinland, Sicherheit und Umweltschutz GmbH, D-51101 Cologne.

[11] Photovoltaic Geographical Information System - Interactive Maps, JRC, European Commission.

[12] Data sheet of photo-voltaic module, HF-40, HF-70 and HF-80, Enecom, Italia.

[13] Data sheet of photo-voltaic module, BP365, BP Solar, Italia.

[14] N. Mohan, T. M. Undeland, and W.P. Robbins, "Power Electronics: Converters, Applications, and Design", 2nd edition, John Wiley & Sons, New York, 1995, chapter 7.

[15] T. Esram and P.L. Chapman, "Comparison of Photovoltaic Array Maximum Power Point Tracking Techniques", *IEEE Trans. on Energy Conv.*, vol. 22 no. 2, pp. 439-449, June 2007.
[16] Q. Lei, F.Z. Peng, L. He and S. Yang, "Semiconductor Losses in Voltage Source and Current Source IGBT Converters Based on Analytical Derivation", Proceeding 35th Annual IEEE Power Electro. Spec. Conf., .2004, pp. 2836-2842, Auchen, Germany.
[17] A. Stabile, C. Boccaletti, and A.J.M Cardoso "A Power Loss Measurement Method Applied to Static Power Converters", *IEEE Trans. Instrumentation and Measurment*, pp. 1-6 Early access.
[18] Y. Ren, M. Xu, J. Zhou, and F.C. Lee, "Analytical Loss Model of Power MOSFET", *IEEE Trans. on Power Electr.*, vol 21, issue 2, pp. 310-319, March 2006.
[19] Q. Zhao, and F.C. Lee, "High-Efficiency, High Step-Up DC–DC Converters", *IEEE Trans. on Power Electr.*, vol. 18, issue 1, pp. 65-73, January 2003.
[20] J. Liu, T.G. Wilson, R.C. Wong, R. Wunderlich, and F.C. Lee, "A Method for Inductor Core Loss Estimation in Power Factor Correction Applications", Proceeding of 17th Annual IEEE Applied Power Electronics Conference and Exposition, 2002. APEC 2002, vol.1, pp. 439-445.

List of publications

Peer reviewed International journals (IJ)

IJ1. R. Keshri, M. Bertoluzzo, and G. Buja, "Integration of a Photovoltaic Panel with an Electric City Car," 2014 [accepted for publication in Jour. of Electric Power Components and Systems, Taylor & Francis]

IJ2. G. Buja, R. Menis, and R. Keshri, "Vector analysis of the current commutation in PM BLDC drives," 2014 [accepted for publication in Bulletin of Polish Academy of Science: Technical Science].

Peer reviewed International conferences (IC)

IC1. M. Bertoluzzo, G. Buja, **R.K. Keshri,** and R. Manis, "Stationary Plane-based Investigation of the Behaviour of PM BLDC Drives". Proceedings of IECON 2013, pp. 6630-6635, November 10-13, Vienna, Austria.

IC2. M. Bertoluzzo, G. Buja, **R.K. Keshri** and R. Manis, "Analytical Study of Torque vs. Speed Characteristics of PM Brushless DC Drives", Proceedings of IECON 2012, pp. 1684-1689, October 25-28, 2012, Montreal Canada.

IC3. G. Buja, **R. Keshri**, and R. Menis, "Comparison of DBI and ZSI Supply for PM Brushless DC Drives Powered by Fuel Cell", Proceedings of IEEE International Symposium of Industrial Electronics, pp. 165-170, June 27-30, 2011, Gdansk, Poland,

IC4. **R. Keshri**, M. Bertoluzzo, A. Kumar, P. Thakura and G. Buja, "Generation of Possible Switching Patterns for VSI Using Micro-controller for the Control of PM BLDC Motor", Proceedings of the Indian International Conference on Power Electronics, 2010, January 28-30, 2011, New Delhi, India.